Experimental Investigation of the In-Plane Behaviour of Concrete Masonry Infills Bounded by Masonry Frames

by

Saber Agaei Foroushani

Submitted in partial fulfilment of the requirements
for the degree of Master of Applied Science

at

Dalhousie University
Halifax, Nova Scotia
November 2019

TABLE OF CONTENT

LIST OF TABLES v
LIST OF FIGURES vii
ABSTRACT xi
LIST OF ABBREVIATIONS AND SYMBOLS USED xii
ACKNOWLEDGEMENTS xvi
CHAPTER 1 INTRODUCTION 1
1.1 BACKGROUND OF MASONRY INFILLED FRAMES 1
1.2 PROPOSED ALL-MASONRY INFILLED SYSTEM 3
1.3 RESEARCH OBJECTIVES 4
1.4 DOCUMENT OUTLINE 5
CHAPTER 2 LITERATURE REVIEW 7
2.1 INTRODUCTION 7
2.2 IN-PLANE BEHAVIOUR OF MASONRY INFILLED FRAMES 7
2.2.1 General Behaviour 7
2.2.2 Stiffness Consideration 8
2.2.3 Failure Modes of Infilled Frames 14
2.2.4 Strength Analysis of Infilled Frames 17
2.3 NORTH AMERICAN CODE PRACTICES 22
2.3.1 CSA S304-14 22
2.3.2 TMS 402/602 23
2.4 BOUNDARY ELEMENTS (BE) 24
2.5 SUMMARY 27
CHAPTER 3 EXPERIMENTAL PROGRAM 29
3.1 GENERAL 29
3.2 INFILLED FRAME SPECIMENS 29
3.3 CONSTRUCTION OF SPECIMENS 34
3.3.1 Base Beam Construction 34
3.3.2. Construction of Masonry Frame and Infill 39

3.4 TEST SET-UP 48
3.4.1 Lateral Loading Setup 48
3.4.2 Vertical Loading Setup 52
3.4.3 Displacement Transducers Arrangement 54
3.5 TESTING PROCEDURE 55
3.6 AUXILIARY TESTS 56
3.6.1 CMUs 56
3.6.2 Mortar 57
3.6.3 Grout 59
3.6.4 Masonry Prism 61
3.6.5 Concrete Cylinders 62
3.6.6 Reinforcement 63
3.6.6.1 Reinforcement for the boundary frame 63
3.6.6.2 Bed Joint Reinforcement 64
CHAPTER 4 EXPERIMENTAL RESULTS 66
4.1 INTRODUCTION 66
4.2 INFILLED FRAME SPECIMEN RESULTS 66
4.2.1 General Behaviour of Specimens Subjected to In-Plane Loading 66
4.2.2 Behaviour and Failure Mode 68
4.2.3 Masonry Bare Frame (BF) 69
4.2.4 Specimen IF-RS 72
4.2.5 Specimen IF-RW 74
4.2.6 Specimen IF-RS-A 77
4.2.7 Specimen IF-BB 80
4.2.8 Specimen IF-BJ 82
4.3 EFFECT OF PARAMETERS ON THE IN-PLANE BEHAVIOUR 84
4.3.1 Effect of Infill Strength 85
4.3.2 Effect of Vertical Load 87
4.3.3 Effect of Infill Reinforcement 90
4.4 STORY DRIFT 94
4.5 DUCTILITY 96

4.6 RESULT OF AUXILIARY TESTS 98
4.6.1 CMUs 98
4.6.2 Mortar 103
4.6.3 Grout 105
4.6.4 Masonry Prism 106
4.6.5 Concrete Cylinder 108
4.6.6 Summary of Auxiliary Test Results 111
CHAPTER 5 COMPARATIVE STUDY OF EXPERIMENTAL RESULTS AND EVALUATION OF ANALYTICAL METHODS 112
5.1 INTRODUCTION 112
5.2 COMPARISON WITH THE PREVIOUS STUDIES BY THE RESEARCH GROUP 112
5.2.1 Comparison with Experimental Results of Hu (2015) 112
5.2.2 Comparison with Experimental Results of Manesh (2013) 116
5.3 COMPARISON WITH CSA S304.14 AND TMS 402/602-16 118
5.3.1 CSA S304.14 Stiffness Evaluation 119
5.3.2 TMS 402/602 Stiffness Evaluation 122
5.3.3 CSA S304.14 Strength Evaluation 123
5.3.4 TMS 402/602 Strength Evaluation 128
5.3.5 Summary 132
CHAPTER 6 SUMMARY AND CONCLUSIONS 133
6.1 SUMMARY 133
6.2 CONCLUSIONS 134
6.3 RECOMMENDATIONS FOR FUTURE RESEARCH 137
REFERENCES 138
APPENDIX A SAMPLE FOR DESIGN STRENGTH AND STIFFNESS CALCULATION 142

LIST OF TABLES

Table 2.1. Summary of Analytical Models of the Equivalent Diagonal Strut Width 10

Table 2.2. Summary of Strength Evaluation Equations for Masonry Infilled Frames 19

Table 3.1. Summary of Test Specimens 30

Table 3.2. Batch Numbers Used for Each Specimen 58

Table 3.3. Grout Batch Numbers for Each Specimen 60

Table 4.1. Summary of the Failure Mode 69

Table 4.2. Summary of Test Results of the Specimens 85

Table 4.3. Test Results Comparison of IF-RW and IF-RS 86

Table 4.4. Test Result Comparison of IF-RS-A and IF-RS 88

Table 4.5. Test Results Comparison of IF-RS, IF-BB and IF-BJ 91

Table 4.6. Summary of the Loads Sustained at Three Allowable Storey Drifts 94

Table 4.7. Summary of Ductility Factor of Specimens 97

Table 4.8. Standard Stretcher CMUs Properties 99

Table 4.9. Half Blocks Properties 99

Table 4.10. Boundary CMUs Properties 100

Table 4.11. Weak Stretcher CMUs (for IF-RW) Properties 100

Table 4.12. Mechanical Properties of CMUs 101

Table 4.13. Mortar Sample Strength 104

Table 4.14. Average Grout Compressive Strength for Specimens 105

Table 4.15. Compressive Strength of Masonry Prisms 108

Table 4.16. Concrete Cylinder Compression Test Results 109

Table 4.17. Summary of Auxiliary Test Results 111

Table 5.1. Summary of Experiment Results of Current and Hu (2015)'s Study 113

Table 5.2. Experiment Results of Current and Manesh (2013)'s Study 116

Table 5.3. Material and Geometrical Properties of Specimens from This Study 119

Table 5.4. Summary of Comparison of CSA S304.14 and Experimental Crack Stiffness 121

Table 5.5. Summary of Comparison of TMS 402/602 and Experimental Crack Stiffness 123

Table 5.6. Comparison of Experimental Results and CSA S304.14 Predicted Ultimate Strengths 127

Table 5.7. Comparison of Experiment Results and TMS 402/602 Predicted Ultimate Strengths 131

LIST OF FIGURES

Figure 1.1. Masonry Infilled Frames: (a) Steel Frame (World House Encyclopedia), (b) RC Frame (Memari AM, Aliaari M 2012) 3

Figure 2.1. Geometrical Features of the Equivalent Strut 8

Figure 2.2. Masonry Infill Geometric Variables Definition 9

Figure 2.3. Three-Strut Infilled Frame Model 13

Figure 2.4. Corner Crushing Mode 15

Figure 2.5. Diagonal Compression Mode 15

Figure 2.6. Sliding Shear Mode 16

Figure 2.7. Diagonal Cracking Mode 16

Figure 2.8. Frame Failure Mode 17

Figure 2.9. Illustration of Geometric Properties of the Equivalent Diagonal Strut 23

Figure 2.10. Buildings Configuration and Walls' Cross Sections 26

Figure 3.1. Geometric Properties of Infilled Frame Specimens (unit:*mm*) 31

Figure 3.2. Geometry and Dimensions of CMUs (unit:*mm*) 32

Figure 3.3. Reinforcement Detail (unit: *mm*) 33

Figure 3.4. Base Beam Concrete Formwork 34

Figure 3.5. Base Beam Rebar Cage Fabrication 35

Figure 3.6. Base Beam Cage Placed in the Formwork 35

Figure 3.7. Base Beams with Column Rebar 36

Figure 3.8. In-Situ Slump Test 37

Figure 3.9. Pouring Cylinders 37

Figure 3.10. Curing with Moist Burlaps 38

Figure 3.11. Air Curing 39

Figure 3.12. General Construction Sequence 41

Figure 3.13. Levelness and Plumbness Checking 41
Figure 3.14. Bare Frame Specimen Construction 42
Figure 3.15. Bed-Joint Reinforcement Detail 43
Figure 3.16. Bed-joint Reinforcement Extension into the Column 44
Figure 3.17. Bond Beam Detail 46
Figure 3.18. Bond Beam Construction 47
Figure 3.19. Overall Test Setup 48
Figure 3.20. Schematic of Lateral Loading Test Setup 49
Figure 3.21. Actuator to Top Beam Connection Detail 50
Figure 3.22. Top and Side View of Beam to Floor Clamping Connection 51
Figure 3.23. Hydraulic Actuator to Brace the Base Beam 51
Figure 3.24. Combined Vertical and Lateral Loading Setup 52
Figure 3.25. Schematic of Vertical and Lateral Loading Test Setup 53
Figure 3.26. Vertical Load Arrangement Detail 53
Figure 3.27. LVDTs Arrangement Detail 55
Figure 3.28. Compression Test Setup for CMUs. (a) Boundary Block, (b) Infills Block 57
Figure 3.29. Sampling Mortar Batches in 2 in. Cubic Molds 58
Figure 3.30. Mortar Samples under Compression Test 59
Figure 3.31. Grout Sampling 60
Figure 3.32. Grout Samples for Compression Test 61
Figure 3.33. Capped Prism Samples in the Instron Machine 62
Figure 3.34. Compression Test Setup for Concrete Cylinder 63
Figure 3.35. Steel Coupon Detailing (Hu 2015 64
Figure 3.36. Tension Test Set-up for Steel Coupons (Hu 2015) 64
Figure 3.37. Bed Joint Reinforcement Coupon Detail 65

Figure 4.1. Lateral Load vs. Displacement Curve of Specimen IF-RS 68

Figure 4.2. Final Crack Pattern of the Masonry Bare Frame..... 70

Figure 4.3. Masonry Bare Frame Failure Pattern 71

Figure 4.4. Lateral Load vs. In-Plane Displacement Curve of the Bare Frame..... 72

Figure 4.5. Final Failure Pattern of IF-RS 73

Figure 4.6. Fracture Crack on the Top Beam of IF-RS 73

Figure 4.7. Lateral Load vs. In-Plane Displacement Curve of IF-RS..... 74

Figure 4.8. Failure Mode for Specimen IF-RW: (a) Final Crack Pattern, (b) Faceshell Spalling at Failure 76

Figure 4.9. Lateral Load vs. In-Plane Displacement Curve of IF-RW 76

Figure 4.10. Crack Pattern at Failure of IF-RS-A..... 78

Figure 4.11. Close-Up View of Failure of IF-RS-A: (a) Vertical Hairline Cracks in the Top Course, (b) Horizontal Mortar Joint Cracks on the Left Boundary Column, (c) Compression and Shear Cracking on the Right Boundary Column..... 79

Figure 4.12. Lateral Load vs. In-Plane Displacement Curve of IF-RS-A 80

Figure 4.13. Final Failure Pattern of IF-BB..... 81

Figure 4.14. Lateral Load vs. In-Plane Displacement of IF-BB..... 82

Figure 4.15. Final Failure Pattern of IF-BJ..... 83

Figure 4.16. Lateral Load vs. In-Plane Displacement Curve of IF-BJ 84

Figure 4.17. Load vs. Displacement Curves for Infill Strength Study 86

Figure 4.18. Comparison of Final Crack Pattern: (a) IF-RS, (b) IF-RW..... 87

Figure 4.19. Load vs. Displacement Curves for Vertical Load Study..... 88

Figure 4.20. Crack Pattern Comparison: (a) IF-RS, (b) IF-RS-A..... 90

Figure 4.21. Lateral Load vs. Displacement Curves for Infill Reinforcement Study..... 91

Figure 4.22. Failure Crack Pattern Comparison: (a) IF-RS, (b) IF-BJ, (c) IF-BB..... 93

Figure 4.23. Comparison of Load vs. Displacement Curves for Drift Study 95

Figure 4.24. Δ_d and Δ_y Definition in Ductility Calculation 97

Figure 4.25. Typical Failure Mode of CMUs 102

Figure 4.26. Typical Failure Mode for Mortar Samples 103

Figure 4.27. Grout Sample Failure mode 106

Figure 4.28. Failure Mode of Masonry Prisms 107

Figure 4.29. Concrete Cylinders Failure Pattern 110

Figure 4.30 Initial Stress vs. Strain Curve of Concrete Cylinders under Compression.. 110

Figure 5.1. Comparison of Load-Displacement Curves for RC Bare Frame and Masonry Bare Frame Specimens 114

Figure 5.2. Comparison of Load-Displacement Curves for Infilled RC Frame and Masonry Frame Specimens 115

Figure 5.3. Comparison of Failure Mode between (a) IF-RS and (b) IF-NG 115

Figure 5.4. Load-Displacement Curves for Axial Load Effect Comparison Study 117

Figure 5.5. Comparison of Failure Mode between (a) IF-RS-A and (b) CF-2 117

ABSTRACT

This study was carried out to investigate the in-plane behaviour of all-masonry infilled frames, i.e., concrete masonry infills bounded by reinforced masonry frames. To this end, six specimens including one masonry bare frame and five all-masonry infilled frame specimens were subjected to lateral loading applied at the frame top beam level to failure. The parameters studied included masonry infill strength, infill reinforcement, and presence of vertical loading. Masonry infill strength study considered a regular and a weaker strength of infills; infill reinforcement study considered two scenarios of horizontal reinforcement in the infill where one was the bed joint reinforcement implemented every other course in the infill and the other was the two bond beams implemented in the infill; and vertical load study involved one specimen under combined vertical and lateral loading where the vertical load was applied to the top beam and held constant while the lateral loading was increased to the specimen failure. Load vs. displacement response, cracking pattern and load, and failure mode and ultimate load for each specimen were obtained and discussed in detail. The experimental results were used to evaluate the validity of stiffness and strength provisions contained in the Canadian (CSA S304.14) and American (TMS 402/602.16) masonry design standards. The performance of specimens was also compared with the infills of the same geometry but bounded by RC frames.

For all infilled frame specimens, the final failure mode seems to be controlled by severe diagonal cracking extending into the boundary columns or a combination of diagonal cracking and shear sliding as in the case of horizontally reinforced infills. No evident corner crushing was observed. An increase in infill strength increased the ultimate load of the infilled frame but showed no evident correlation with the infill-frame system stiffness. Implementing infill reinforcement did not have a significant effect on the ultimate strength but resulted in an increase in both the initial and cracking stiffnesses as well as ductility of the specimen. Presence of vertical load resulted in a marked increase in ultimate load of the infilled specimen but at the expense of a reduced ductility. In general, CSA S304-14 overestimated whereas TMS 402/602 underestimated the stiffness with a similar range of disparity to the test results. In the case of strength prediction, CSA S304 performed better than TMS 402/602 with predicted values closer to the test results. The comparison with infilled RC frames showed that behaviour, strength, and ductility of all-masonry infilled frames are similar to, and in some cases, slightly better than infilled RC frames.

LIST OF ABBREVIATIONS AND SYMBOLS USED

SYMBOLS

A	Compressive area of infill diagonal strut
A_c	Cross-sectional area of the RC column
A_{nv}	Net shear area
A_o	Area of infill opening
A_p	Surface area of infill
b_w	Thickness of the web of the infill
c	Empirical constant that varies with in-plane displacement
C	Multiplication factor accounting for infill aspect ratio
d	Diagonal length of infill
e	Eccentricity of the load
E_f	Modulus of elasticity of frame
E_m, E_I	Modulus of elasticity of masonry
f'_m	Compressive strength of masonry
f'_{m-0}	Masonry strength parallel to bed joints
f'_{m-90}	Masonry strength perpendicular to bed joints
f_{bs}	Shear bond strength between the masonry and mortar
f_t	Tensile strength of masonry infill
h, h'	Height of infill, frame
F_v	Total applied vertical load to the frame
H_{CC}	Corner crushing strength of infill xiv
H_{DC}	Diagonal cracking strength of infill

H_{SS}	Sliding shear strength of infill
I_b	Moment of inertia of area of beam
I_c	Moment of inertia of area of column
K_{ini}	Initial stiffness
K_{cr}	Cracking stiffness
K_{ult}	Ultimate stiffness
l, l’	Length of infill, frame
M_f	Factored moment at section
M_p	Plastic moment capacity of either the frame beam or column
M_{pb}	Plastic moment capacity of beam
M_{pc}	Plastic moment capacity of column
M_{pj}	Plastic moment capacity of the joint
N_u	Factored compressive force
P_r	Factored axial load resistance
P_{d1}, P_{d2}, P_{d3}	Load at the lateral drift of 1%, 2% and 2.5% of the infilled frame
P_{cra}	Crack strength
P_{ult}	Ultimate strength
R	Ductility
t	Thickness of infill
t_e	Effective thickness of infill
μ	Coefficient of friction between the interface of the infill and frame
ν	Poisson’s ratio
ν_m	Shear strength of masonry

V_f	Factored shear at section
V_n	Nominal shear strength
V_r	Ultimate load of different failure modes
w	Width of the diagonal strut
w_{eff}	Effective width of the diagonal strut
W_R	Received weight
W_I	Immersed weight
W_S	Saturated weight
W_D	Dry weight
α_b, α_l	Contact length between the beam and the infill
α_c, α_h	Contact length between the column and the infill
θ	Angle whose tangent is the infill height to length aspect ratio, in radians.
λ	Dimensionless infill relative stiffness parameter
λ_p	Relative stiffness correlated to the beam
λ_T	Relative stiffness correlated to the adjacent column
γ_g	Factor to account for partially grouted and ungrouted walls constructed of units
ϕ_m	Masonry resistance factor
Δ_u	Ultimate displacement
Δ_y	Yield displacement
Δ_d	Displacement at 80% of ultimate strength after ultimate point
χ	Factor to account for direction of compressive stress in masonry member relative to the direction used for determination of f'_m

ABBREVIATIONS

ASTM	American Society for Testing and Materials
BF	Bare frame
CC	Corner crushing
CMU	Concrete masonry unit
CSA	Canadian Standards Association
CV	Coefficient of variation
DC	Diagonal cracking
DC	Diagonal Cracking
DSC	Diagonal Strut Compression
FF	Frame Failure
LVDT	Linear variable differential transformer
MSJC	Masonry Society Joint Committee
NBCC	National Building Code of Canada
RC	Reinforced concrete
SS	Sliding shear
TMS	The Masonry Society

ACKNOWLEDGEMENTS

I would like to express my deepest gratitude to my supervisor Dr. Yi Liu for her irreplaceable guidance, monitoring, and generous support. I feel really fortunate that I have her as my supervisor. Without her direction and patience, this dissertation would not have been possible.

I would also like to thank my committee members, Dr. Hany El-Nagger and Dr. Navid Bahrani, for taking the time to review this dissertation and provide valuable feedback.

I would like to thank my fellow colleagues, Reza Rahimi, Soraya Roosta and Ali Hosseini for their assistance during testing.

I would like to thank Mr. Jordan Maerz, Mr. Jesse Keane, and Mr. Brian Kennedy for their kind assistance during specimen construction and the test set up. I would also like to thank Mr. Andrew Smith for providing me with the materials and professional mason for the construction of specimens.

My thanks also go to the Canadian Concrete Masonry Products Association for providing me with financial assistance.

Lastly, I would like to thank my parents and oldest brother for their vital support, inspiration, and unconditional love.

CHAPTER 1 INTRODUCTION

1.1 BACKGROUND OF MASONRY INFILLED FRAMES

The use of masonry materials in construction dates back ten thousand years ago (Drysdale and Hamid 2005). The earliest form of masonry materials consists of mostly sun-dried clay or natural stones. They have evolved to include calcium silicate, oven-dried clay (brick masonry), and recently, concrete masonry units (CMUs) in the early 20th century. Masonry materials commonly find their application in compression members such as columns and walls in building construction. The use of masonry walls to infill either steel or reinforced concrete (RC) frames is a common practice in building construction. Referred to as masonry infills, these walls provide either partitions for interior space or cladding for the exterior envelope for buildings. In North America, the CMUs and clay bricks are two masonry products often employed as the infill materials. Figure 1.1 shows examples of either infilled steel or RC frames. Previous research has shown that if constructed in tight contact with its bounding frame, the infill will participate in the load sharing and thus significantly affects the stiffness, strength and ductility of the infilled frame system (Mehrabi et al. 1996; Al-Chaar 2002; El-Dakhakhni 2002; Liu and Soon 2012). Hence, the design of the "participating infills" needs to accurately quantify the interaction between the infill and its bounding frame and, ultimately, its contribution to the frame behaviour.

To that end, a considerable amount of research on the general subject of masonry infilled frames has been conducted in the past five decades. Some analytical models have been proposed to evaluate the infill effect on the system behaviour and strength. A detailed literature review is provided in Chapter 2. For design, the current Canadian masonry design

standard (CSA S304-14) and American standard (TMS 406/602-16) both provide design equations for calculation of the frame system stiffness and strength considering the infill effect. Despite a large amount of physical evidence of the benefit of infills to the system behaviour and availability of code provisions, the industry practice has been to treat the masonry infills as non-structural elements and design the frame for both gravity and lateral load. There might be multiple reasons for this disconnect between the experimental results and industry practice. But one is believed to be related to how the current masonry infilled frames are constructed. Either bounded by RC or steel frames, the infilled frames require two trades, i.e., concrete or steel and masonry. Masonry infills are often designed by architects while the frame structure is designed by structural engineers. The coordination of two trades and design teams often presents a challenge from a practical standpoint to make the design and construction consistent. Hence, this study is to develop a novel, all-masonry infilled frame system where the bounding frame is also made of masonry.

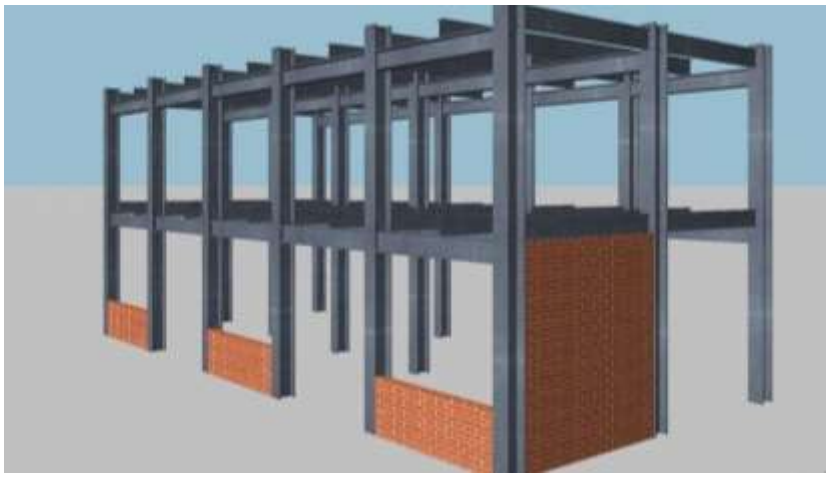

(a)

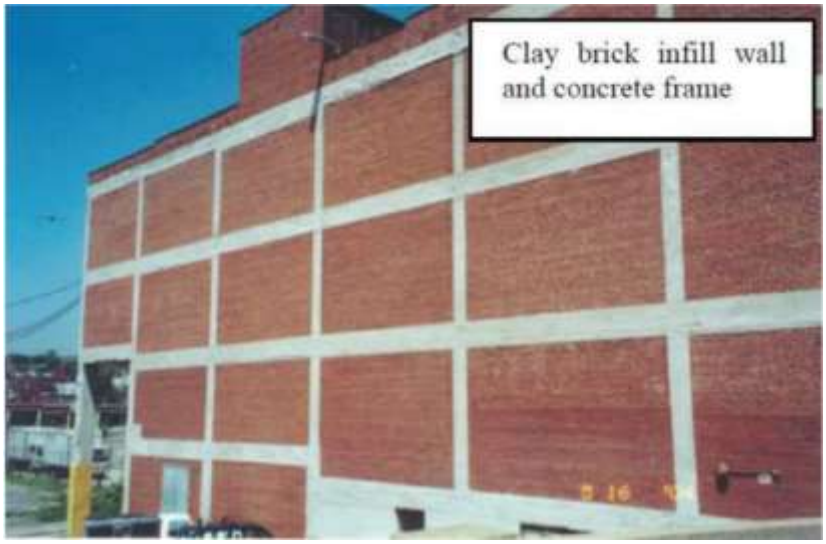

(b)

Figure 1.1. Masonry Infilled Frames: (a) Steel Frame (World House Encyclopedia), (b) RC Frame (Memari AM, Aliaari M 2012)

1.2 PROPOSED ALL-MASONRY INFILLED SYSTEM

Conceptually, an all-masonry infilled frame is similar to a masonry infilled RC frame and the difference is that the bounding frame for the former is also made of masonry. In the former case, masonry reinforced columns and tied beams form the masonry frame while the masonry infill may be constructed in the same manner as in the conventional infilled

RC frames. From both construction and design perspectives, all-masonry infilled frames are advantageous as design for the frame and the infill can be carried out in the same consulting firm and constructed at the same time with one material and thus eliminating the need to coordinate with concrete or steel trades as in the case of steel or RC frames. In addition, simultaneous construction of the frame and the infill makes it easier to include vertical reinforcement in the infill as well as provide alternative forms of interfacial connection where mechanical anchorage between the frame and infill may be implemented as opposed to simple mortar bedding.

This study is part of an ongoing experimental and numerical research program at Dalhousie University on the behaviour of masonry infill walls. Under this framework, studies have been conducted in the same research group on masonry infilled steel and RC frames subjected to both in-plane and out-of-plane loading (Soon 2011; Manesh 2013; Hu 2015; Steeves 2017). The results of the previous studies will be used for comparison in the evaluation of the performance of all-masonry infilled frames.

It is recognized that while sharing some similarities with masonry infilled RC frames, different configuration and associated construction details make the all-masonry infilled frame system essentially a unique system with different behavioural characteristics. Experimental results on its performance and how it is compared with respect to the conventional infilled RC frames are needed.

1.3 RESEARCH OBJECTIVES

The main objective of this study is to experimentally investigate the strength and behaviour of the all-masonry infilled frame systems subjected to in-plane loading focusing on the

effect of several material, geometric and loading parameters. These parameters included masonry infill strength, infill horizontal reinforcement, and presence of vertical loading. These parameters were selected due to their practical relevance to the construction of this type of infilled frames.

A detailed description of the research objectives is summarized as follows:

1. To provide experimental results on the strength and behaviour of all-masonry infilled frames subjected to in-plane loading.

2. To analyze the effect of the above-mentioned key parameters on the performance of all-masonry infilled frame systems.

3. To evaluate the performance of this system against infilled RC frames.

4. To assess the validity of existing analytical models developed for infilled RC/steel frames when used to evaluate the strength of all-masonry infilled frames.

1.4 DOCUMENT OUTLINE

The thesis consists of six chapters. Chapter 1 includes an introduction along with objectives and scope of this thesis. Chapter 2 presents a literature review of previous studies on masonry infilled frames in general, existing analytical methods for the stiffness and strength calculations of such systems, and the guidelines contained in the current North American masonry design standards on the design of infilled frames. Chapter 3 provides a detailed description of the experimental program. Chapter 4 contains a description and discussion of the results from the specimens and auxiliary tests. Chapter 5 presents an evaluation of the design codes by comparing the experimental results with the analytical

values and previous experimental results on RC frames. Chapter 6 presents a summary of the research and the conclusions draw from this study.

CHAPTER 2 LITERATURE REVIEW

2.1 INTRODUCTION

While there is considerable research available in the literature on the in-plane behaviour and strength of masonry infilled RC or steel frames, the research conducted specifically on masonry infills with masonry bounding frames is none. Hence, this chapter provides a review of general behaviour, failure modes and state-of-the-art research on masonry infills bounded by RC and steel frames. It is believed that the fundamental behavioural characteristics for masonry infills are similar. The masonry bounding frame, in this context, shares similarities with masonry boundary elements (BE). The chapter thus also provides a review of literature on the behaviour of masonry shear walls incorporating BEs under in-plane lateral loading.

2.2 IN-PLANE BEHAVIOUR OF MASONRY INFILLED FRAMES

2.2.1 General Behaviour

The behaviour of masonry infilled frames lies in the interaction between the infill and its bounding frame. It has been shown that at relatively low level of lateral force, the infill and frame act together and provide shear resistance to deformation. As load increases, the infill begins to form diagonal cracks connecting loaded corners, and as cracking develops and the frame further deforms, two contact regions, in the diagonal direction, are created, as shown in Figure 2.1. The frame system with the masonry infill is equivalent to a frame with a diagonal strut for resisting the lateral load. The “diagonal strut method” for calculating frame system strength was first proposed by Polyakov (1960), where a diagonal strut with appropriate mechanical properties can be used to replace the entire infill in a frame analysis. Since its inception, it has become the main method of analysis for masonry

infill walls and has been adopted in various forms in most masonry design standards across the world.

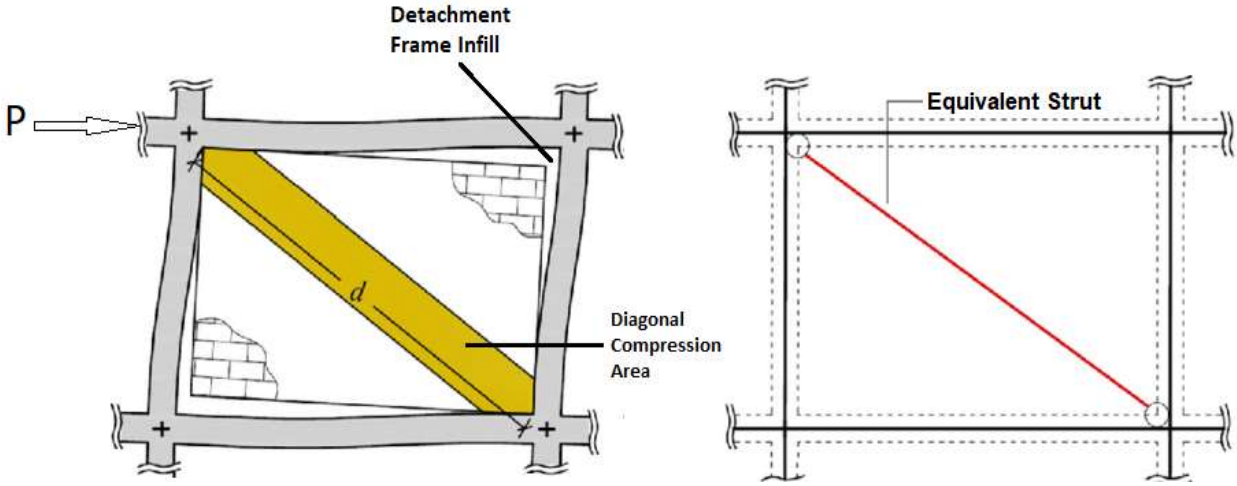

Figure 2.1. Geometrical Features of the Equivalent Strut

(Adapted from Fabio Di Trapani et al. 2015)

2.2.2 Stiffness Consideration

Based on the concept of the diagonal strut method, the key parameter is to determine the width of the strut. Once the strut width is known, the system stiffness can be calculated by performing a simple frame analysis assuming the thickness and material property of the strut to be the same as the masonry infill. The infill strength can also be related to strut width. In the past five decades, many studies have been conducted to develop a rational approach for the diagonal strut width calculation to accurately reflect the stiffness of an infilled frame as a braced frame. To that end, a few analytical models have been proposed and a summary of them is provided in Table 2.1 with the key geometric symbols defined in Figure 2.2. Equations proposed before the 1990s were mainly based on calibrating an analytical model using experimental results on one or another specific type of masonry/frame situation. Equations proposed after the year 2000 had more reliance on

results obtained through finite element models encoded on computer software. While the simplest form of the diagonal strut width was expressed as a fraction of infill diagonal strut length, d, most models considered the strut width as a function of the relative stiffness between the infill and the bounding frame, defined through a stiffness parameter, λ_h. Most equations are explained in the table, those which needs more information are elaborated in the following.

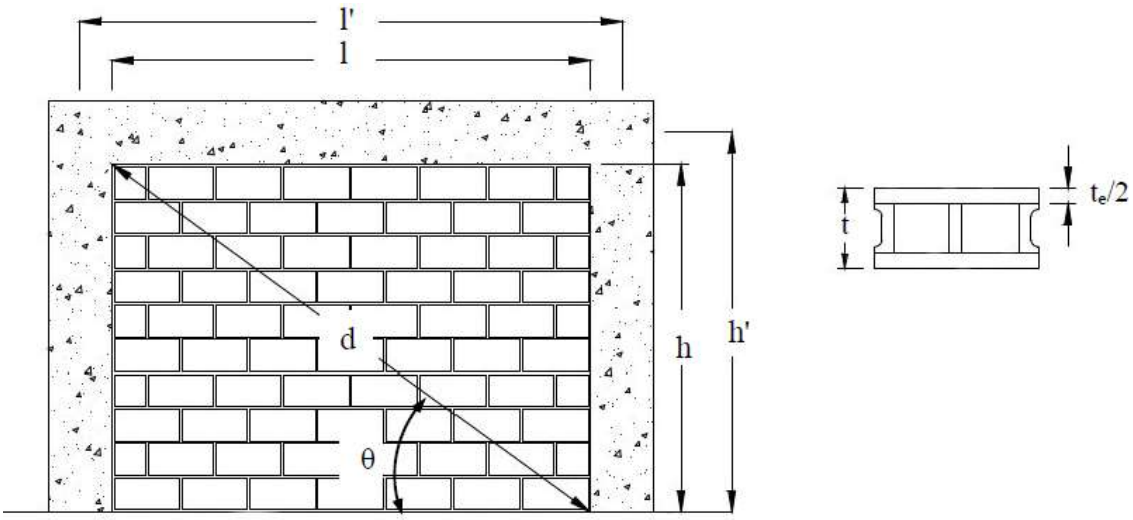

Figure 2.2. Masonry Infill Geometric Variables Definition

Table 2.1. Summary of Analytical Models of the Equivalent Diagonal Strut Width

Author	Equation		Type of Infill and Frame	Note
Holmes (1961)	$w = d/3$	[2-1]	Experimental study Brick masonry infilled Steel frame	d: Infill diagonal length
Smith and Carter (1969)	$w = 0.58(\frac{1}{h})^{-0.445}(\lambda_h h')^{0.335d(\frac{1}{h})^{0.064}}$ $\lambda_h = \sqrt[4]{\frac{E_I t sin(2\theta)}{4E_c Ih}}$	[2-2]	Experimental study Concrete masonry infilled RC frame	α_c: Contact length between the infill and frame at loaded corner λ_h: Relative stiffness of the masonry infill and the frame θ: Slope of the infill diagonal to the horizontal. E_I *and* E_C: Young's moduli of the infill and frame column
Mainstone (1971)	$w/d = 0.175(\lambda_h h')^{-0.4}(4 \le \lambda_h h' \le 5)$ $w/d = 0.16(\lambda_h h')^{-0.3} \quad (\lambda_h h' \ge 5)$	[2-3]	Experimental study Concrete masonry infilled steel frame	λ_h: Relative stiffness parameter
Liauw and Kwan (1984)	$w = \frac{0.86hcos\theta}{\sqrt{\lambda_h h}}, or\ 0.45hcos\theta$	[2-4]	Finite element study Masonry infilled frame	θ: Slope of the infill diagonal to the horizontal.

Table 2.1. Summary of Analytical Models of the Equivalent Diagonal Strut Width (cont'd)

Dawe and Seah (1989)	$w = \frac{2\pi}{3}(\frac{cos\theta}{\lambda_P} + \frac{sin\theta}{\lambda_T})$ $\lambda_P = \sqrt[4]{\frac{E_I t sin2\theta}{4E_C I_p h'}}$ $\lambda_T = \sqrt[4]{\frac{E_I t sin2\theta}{4E_C I_T h'}}$	[2-5]	Experimental/Numerical study Concrete masonry infilled steel frame	t: Thickness of panel λ_p: Relative stiffness correlated to the beam λ_T: Relative stiffness correlated to the adjacent column E_I *and* E_C: Elastic moduli of the infill and the RC frame
Paulay and Priestley (1992)	$w = 0.25d$	[2-6]	Experimental/numerical study Masonry infilled frames	d: Infill diagonal length
Hendry (1998)	$w = 0.5\sqrt[2]{\alpha_h + \alpha_l}$ $\alpha_h = \frac{\pi}{2}\sqrt[4]{(\frac{E_c I_c h}{2E_I t sin2\theta})}$ $\alpha_l = \pi\sqrt[4]{(\frac{E_c I_b L}{2E_I t sin2\theta})}$	[2-7]	Numerical study Frame-infill system	E_C *and* E_I: Young's moduli of frame column and masonry infill I_c and I_b: Moment of inertia of column and beam α_h *and* α_l: Contact length between infills and column and beam
Flanagan and Bennett (1999)	$w = \frac{\pi t}{c\lambda_h cos\theta}$	[2-8]	Experimental study Clay tile infilled steel frame	c: Empirical constant varies with the in-plane drift t: Thickness of infill

Table 2.1. Summary of Analytical Models of the Equivalent Diagonal Strut Width (cont'd)

Al-Chaar (2002)	$w = 0.0835Cd(1 + 2.574/\lambda_h h')$ $for l/h \geq 1.5$ $w = 0.1106d(1 + 6.027/\lambda_h h')\ for\ l/h = 1$ $C = -0.3905(l/h) + 1.7829$	[2-9]	Experimental/numerical study Concrete and brick masonry infilled RC frame	d: Infill diagonal length C: Non-dimensional factor to consider aspect ratio effect
*El-Dakhakhni et al. (2003)	$A = \frac{(1-\alpha_c)\alpha_c h' t}{cos\theta}$	[2-10]	Numerical study Masonry infilled steel frame	$\alpha_c h$: Contact length along height of the infill
*Papia et al. (2003)	$w = dk\frac{c}{z(\lambda)^{\beta}}$ $c = 0.249 - 0.116\nu_d + 0.567{\nu_d}^2$ $\beta = 0.146 - 0.0073\nu_d + 0.126{\nu_d}^2$ $\lambda = \frac{E_I t h}{E_C A_C}(\frac{h^2}{l^2} + \frac{A_C l}{4A_b h})$	[2-11]	FE Analysis Frame-infill system	k: Vertical load effect ν_d: Poisson ratio along diagonal direction A_b *and* A_C: Section area of beam $Z = \begin{cases} 1 & l/h=1 \\ 1.125 & l/h=1.5 \end{cases}$

*Elaborated in the following sections

In the case of Eqn [2-10], a multi-strut concept was proposed by El-Dakhakhni et al. (2003). They argued that one strut is not adequate in capturing the moment effect generated by the infill on the frame members and thus proposed a 3-strut model with the assigned area for each strut as shown in Figure 2.3. The two regions of diagonal compression are defined by the contact lengths along the height and length of the infill, $\alpha_c h$ and $\alpha_b l$, respectively, as follows:

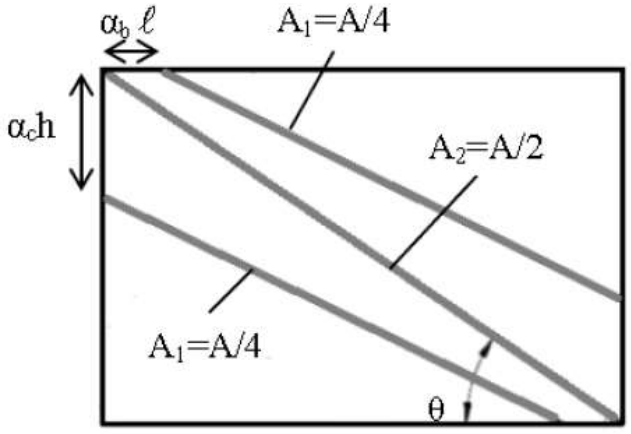

Figure 2.3. Three-Strut Infilled Frame Model
(Adapted from El-Dakhakhni et al. 2003)

$$\alpha_c h = \sqrt{\frac{2(M_{pj}+0.2M_{pc})}{f'_{m0}t}} \leq 0.4h \qquad [2\text{-}12]$$

$$\alpha_b l = \sqrt{\frac{2(M_{pj}+0.2M_{pc})}{f'_{m90}t}} \leq 0.4l \qquad [2\text{-}13]$$

where M_{pc} and M_{pb} are the plastic moment capacity at the column and beam respectively; M_{pj} is the plastic moment capacity of the joint taken as the least capacity of the column, beam, or connection; $f'_{m\text{-}0}$ and $f'_{m\text{-}90}$ are the masonry strength parallel and perpendicular to the bed joint, respectively.

In the case of Eqn [2-11], Papia et al. (2003) studied the effect of vertical load on the diagonal strut approach. They introduced a factor, k, in the calculation of the strut width as follows:

$$w = dk\frac{c}{z(\lambda)^{\beta}} \qquad [2\text{-}14]$$

The factor k depends on the level of the vertical loads acting on the columns which is expressed as:

$$k = 1 + (18\lambda + 200)\varepsilon_v \qquad [2\text{-}15]$$

$$\varepsilon_v = \frac{F_v}{2A_cE_c} \qquad [2\text{-}16]$$

where E_c and A_c are the Young's modulus and cross-sectional area of the RC column, respectively. F_v is the total vertical load applied to the frame. This equation is only applicable for vertical load applied through frame columns and it results in an increase in the diagonal strut width, and thus stiffness of the system as the vertical load is applied.

2.2.3 Failure Modes of Infilled Frames

Along with the stiffness studies, both experimental and numerical studies were also conducted to evaluate failure modes of masonry infilled frames (Liauw and Kwan 1983; Mehrabi and Shing 1996; Shing et al. 2002; El-Dakhakhni 2002; El-Dakhakhni et al. 2003; Drysdale and Hamid 2005; Liu and Soon 2012; Hu 2015; Xi 2016). For masonry infilled frames of various material, geometry and construction techniques, five potential failure modes have been identified and they are:

(a) The corner crushing (CC) mode, which represents crushing of the infill at the loaded corners, as shown in Figure 2.4. This mode is generally associated with weak masonry infill surrounded by a relatively strong frame.

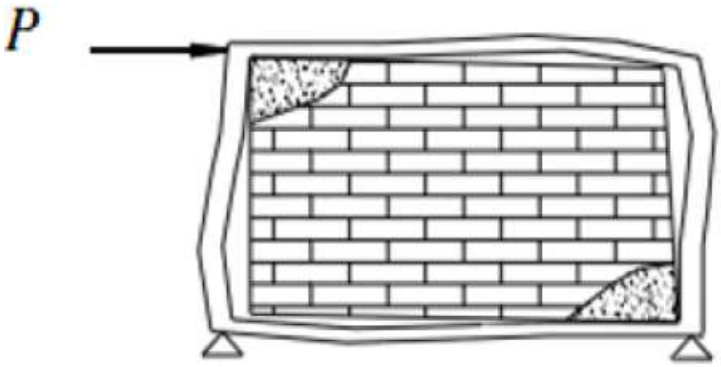

Figure 2.4. Corner Crushing Mode

(Adapted from El-Dakhakhni 2003)

(b) The diagonal strut compression (DSC) mode, which associates with slender infills and results in out-of-plane buckling, where crushing occurs, within the central region of diagonal strut, as shown in Figure 2.5.

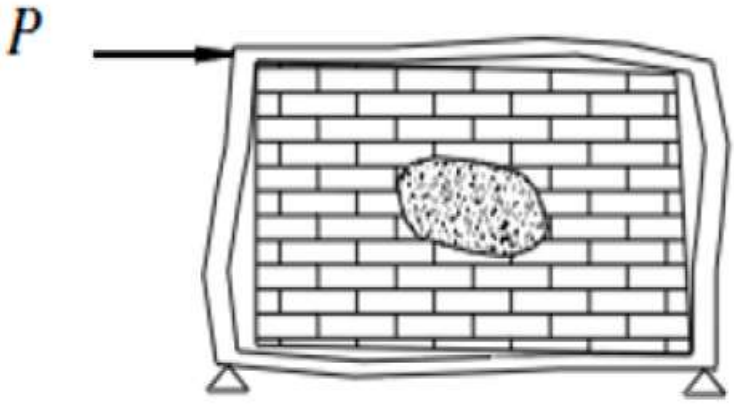

Figure 2.5. Diagonal Compression Mode

(Adapted from El-Dakhakhni 2003)

(c) The sliding shear (SS) mode, representing horizontal sliding through bed joints of a masonry infill, as shown in Figure 2.6. This phenomenon is associated with weak mortar joints and a strong frame.

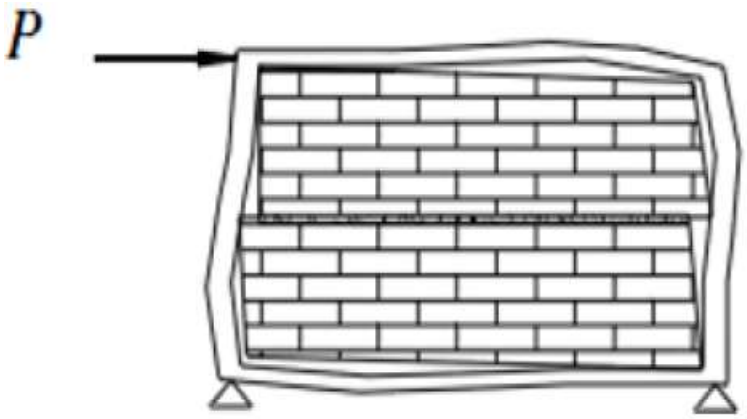

Figure 2.6. Sliding Shear Mode

(Adapted from El-Dakhakhni 2003)

(d) The diagonal tension cracking (DC) mode, which is seen in the form of cracks along the compressed diagonal, as shown in Figure 2.7. This mode of failure occurs when the diagonal tension forces causes cracks in the diagonal strut.

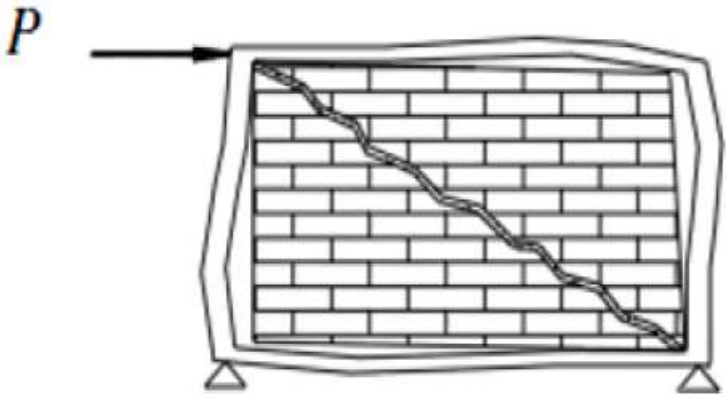

Figure 2.7. Diagonal Cracking Mode

(Adapted from El-Dakhakhni 2003)

(e) The frame failure (FF) mode, is seen in the form of plastic hinges developing at the columns or the beam-column connections, as displayed in Figure 2.8. This mode often occurs in a strong infills-weak frame systems or frames with weak joints.

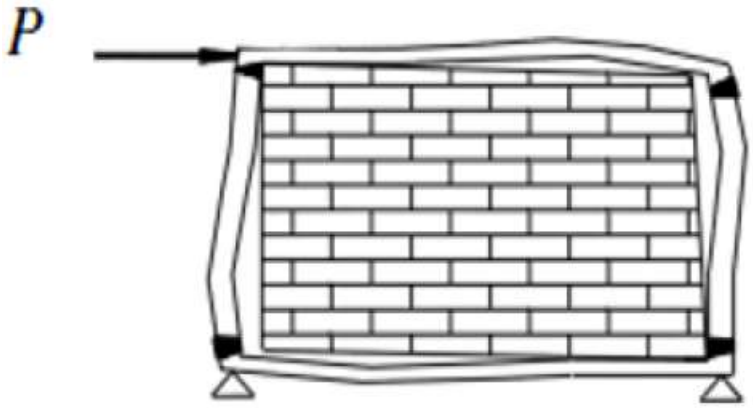

Figure 2.8. Frame Failure Mode

(Adapted from El-Dakhakhni 2003)

For masonry infilled frames of typical material and geometry and constructed in North America, corner crushing was identified as the most common failure mode. The diagonal tension cracking was also observed to often initiate the failure although the final failure was by corner crushing. The sliding shear mode was also reported when the mortar joints were weak in the infill.

2.2.4 Strength Analysis of Infilled Frames

Since 1960, several analytical models have been proposed to calculate the lateral strength of masonry infilled frames. A summary of the existing strength models is provided in Table 2.2. As can be seen, most equations were proposed for corner crushing (CC), sliding shear (SS), and diagonal cracking (DC) as they were the most often observed failure. These models were mainly empirical and all more or less based on the diagonal strut concept, relating the lateral strength of the infill to some forms of strut width. It should be pointed

out that each model, whether developed based on experimental results or numerical studies, was calibrated against a set of experimental results of material and geometric properties of the infilled systems specific to the study. Most often, these experimental results were limited in the number of specimens and range of variation of parameters. Thus, none of these models is found universally applicable to all types of masonry infilled frames (Xi and Liu 2016). Nonetheless, they are listed to provide information on the development of strength equations.

Table 2.2. Summary of Strength Evaluation Equations for Masonry Infilled Frames

Author	Equation		Type of Infill and Frame	Note
Mainstone (1971)	$H_{CC} = 0.56(\lambda_h h)^{-0.875} f'_m h' t cot(\theta) \quad 4 \le \lambda_h h' \le 5$ $H_{CC} = 0.52(\lambda_h h)^{-0.8} f'_m h' t cot(\theta) \quad \lambda_h h' \ge 5$	[2-17] [2-18]	Experimental study Concrete masonry infilled steel frame	λ_h: Relative stiffness parameter (Eqn [2-2]) f'_m= Masonry infill compressive strength
Rosenbluth (1980)	$H_{SS} = \left(0.9 + 0.3\frac{l}{h}\right) f_{bs} h t$ $H_{CC} = \frac{2}{3}\alpha_c t f'_m sec(\theta)$ $\alpha_C = \frac{\pi}{2}\sqrt[4]{\frac{4E_c I_c h}{E_I t sin2\theta}}$	[2-19] [2-20]	Experimental study Masonry infilled RC frame	f_{bs}= Shear bond strength between the masonry and mortar α_c= Contact length of the infill and column
Decanini and Fantin (1986)	$H_{DC} = (0.6\tau_{m_0} + 0.3\sigma_0) t d cos\theta$ $H_{SS} = ((1.2 sin\theta + 0.45 cos\theta)\tau_0 + 0.3\sigma_0) t d cos\theta$ $H_{CC} = \frac{(1.12 sin\theta cos\theta)}{(\lambda_h)^{0.88}} f'_m t d cos\theta$	[2-21] [2-22] [2-23]	Experimental study All material infilled frames	τ_{m0}= Shear strength evaluated through diagonal compression tests ($\tau_{m_0} = 0.285\sqrt{f'_m}$) σ_0= Total vertical stress due to gravity loads τ_0= Slide resistance in the joints (τ_0= 0.7 τ_{m_0})

Table 2.2. Summary of Strength Evaluation Equations for Masonry Infilled Frames (cont'd)

Smith and Coull (1991)	$H_{CC} = f'_m t \frac{\pi}{2} \sqrt[4]{\frac{4E_c I_c h'}{E_I t}}$	[2-24]	Numerical study All material infilled frames	(Terms are defined before)
Paulay and Priestley (1992)	$H_{DT} = \frac{\pi}{2} t d f'_m cos\theta$	[2-25]	Numerical study Masonry infilled RC frames	(Terms are defined before)
Priestley and Calvi (1991)	$H_{SS} = \frac{0.03 f'_m}{1 - 0.3(h/l)} t d cos\theta$	[2-26]	Numerical study All material infilled frames	(Terms are defined before)
Saneinejad and Hobbs (1995)	$H_{SS} = min\begin{cases} \frac{\gamma \tau_0 t d}{1 - 0.45 tan\theta} cos\theta \\ 0.83 \gamma t d cos\theta \end{cases}$	[2-27]	Numerical study All material infilled frames	f_t= Tensile strength of infill γ= Load factor $\alpha_c h$ and σ_c = Contact length and contact stress between the column and infill α_b and τ_b= Contact length and contact stress between the beam and infill
	$H_{DT} = 2\sqrt{2} t d f_t cos^2\theta$	[2-28]		
	$H_{CC} = (1 - \alpha_c)(\alpha_c h) t \sigma_c + (\alpha_b l)(t \tau_b)$	[2-29]		

Table 2.2. Summary of Strength Evaluation Equations for Masonry Infilled Frames (cont'd)

Mehrabi (1996)	$H_{SS} = 0.34A_w + 0.9P_w$	[2-30]	Experimental study Masonry infilled RC frames	A_w= Horizontal cross section of infill P_w= Vertical load
Flanagan and Bennett (1999)	$H_{CC} = k_{cc} t f'_m$	[2-31]	Experimental study Clay tile infilled Steel frame	K_{cc}= Empirical constant for corner crushing with a mean value of 246 mm for clay tile infills

Note: H_{SS}= the sliding shear capacity; H_{CC}= the corner crushing strength; H_{DC}= the diagonal tension strength

2.3 NORTH AMERICAN CODE PRACTICES

2.3.1 CSA S304-14

The Canadian masonry design standard (CSA S304-14) adopts the equivalent diagonal strut concept for masonry infill design. Based on the model proposed by Stafford-Smith and Carter (1969), the strut width, w, is considered a function of contact areas between the infill and the frame beam and column, α_h and α_l, respectively, as shown in Figure 2.9.

$$w = \sqrt{{\alpha_h}^2 + {\alpha_L}^2} \qquad [2\text{-}32]$$

$$\alpha_h = \frac{\pi}{2}\sqrt[4]{\frac{4E_f I_c h}{E_m t_e \sin 2\theta}}\,;\ \alpha_L = \pi\sqrt[4]{\frac{4E_f I_b l}{E_m t_e \sin 2\theta}} \qquad [2\text{-}33]$$

where t_e is the effective thickness of the masonry infill, E_f is the elastic modulus of the frame material, I_b and I_c are the moment of inertia of the beam and column, respectively. The effective diagonal strut width, w_{eff}, along which the stress can be considered uniform, is taken as w/2 and less than quarter of the diagonal strut length.

For stiffness consideration, S304-14 specifies that the effective strut width be further reduced to $0.5w_{eff}$. S304-14 considers three failure modes for determination of the in-plane strength of masonry infills, and they are corner crushing, shear sliding, and diagonal tension cracking. The formulae related to strength evaluation are presented in Chapter 5. In all cases, the strength equations are related to the diagonal strut width and in this case, the w_{eff} is used as the strut width. The difference in strut width for stiffness and strength consideration is based on experimental evidence and numerical results of the work by Soon and Liu (2012).

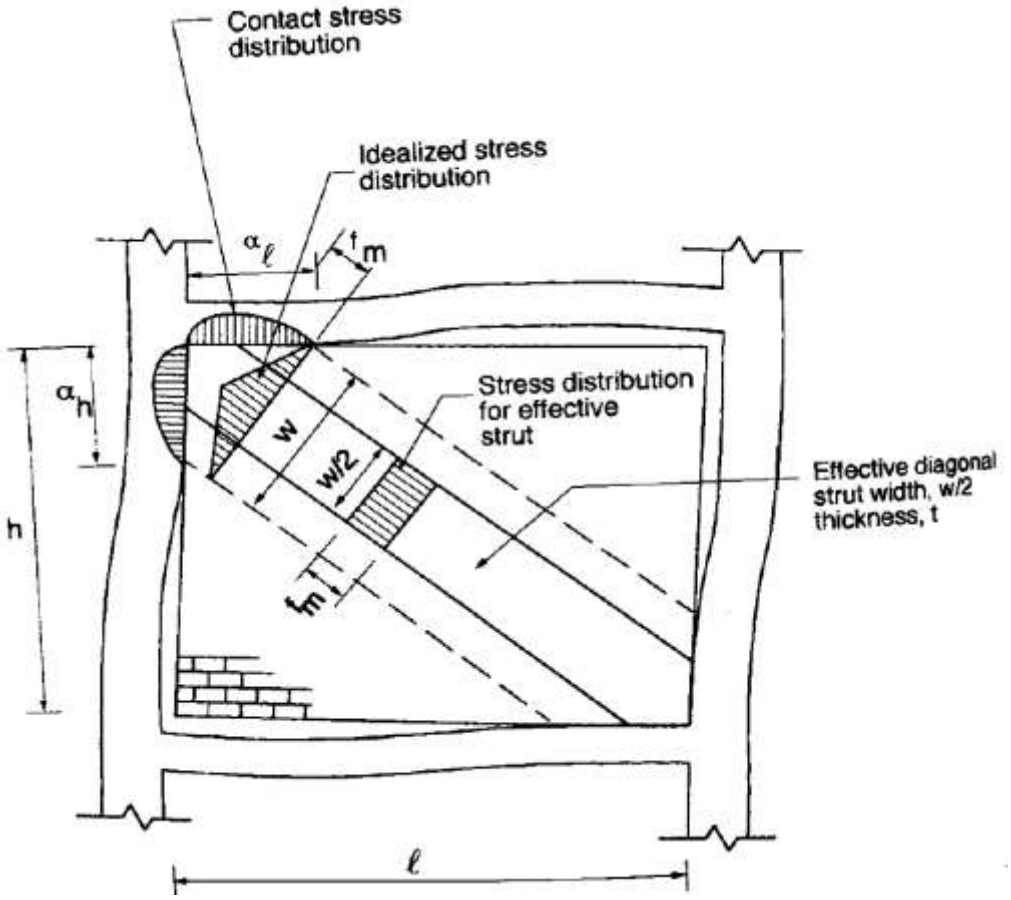

Figure 2.9. Illustration of Geometric Properties of the Equivalent Diagonal Strut (Adapted from Drysdale and Hamid 2005)

2.3.2 TMS 402/602

Similar to CSA S304-14, the American standard TMS 402/602 states that the infill shall be analyzed as an equivalent strut to calculate the stiffness of the infilled system. Based on the work conducted by Flanagan and Bennett (1999), the width of the diagonal strut is expressed as follows:

$$W_{inf} = \frac{0.3}{\lambda_{strut} cos\theta_{strut}} \qquad [2\text{-}34]$$

where λ_{strut} is the stiffness parameter and defined as below, for the design of concrete and clay masonry infills:

$$\lambda_{strut} = \sqrt[4]{\frac{E_m t_e \sin 2\theta}{4 E_{bc} I_{bc} h}} \quad [2\text{-}35]$$

where E_{bc} and I_{bc} are the Young's modulus and moment of inertia of bounding columns, respectively, and t_e is the effective thickness of the infill. The factor of 0.3 is used to account for the potential damage sustained by diagonal mortar joints with no damage to the infill (Flanagan & Bennett 1999). Although similar in concept, the TMS equation is a simplified diagonal strut equation where the bounding beam effect is considered negligible and the width is largely dependent on the bounding column stiffness.

In TMS 402/602, the in-plane strength of infilled frames is also evaluated based on three failure modes, i.e., corner crushing, sliding shear, and 25 *mm* lateral displacement of the frame. The formula for each is described in Chapter 5. It should be pointed out here that for corner crushing, the TMS simply uses a constant term of 6 inches as the diagonal strut width to account for the compressive capacity of the diagonal strut.

Moreover, the proposed method in either S304-14 or TMS 402/602 is only recommended for "simple" infill situations. For infills with openings, horizontal reinforcement, or simultaneous vertical loading, neither standard provides guidelines for the treatment of those cases.

2.4 BOUNDARY ELEMENTS (BE)

The concept of boundary elements stemmed from the design of masonry shear walls as part of the lateral load resisting system of a structure. The geometry of conventional masonry block units makes it difficult to accommodate the same amount of rebars as in a reinforced concrete case due to the size of the cavity within the masonry unit. To achieve the same

shear resistance as a reinforced concrete wall, a thicker masonry wall would be required to just make the equivalent amount of reinforcement fit. The boundary elements essentially are larger block units containing a thin face-shell permitting large open areas for reinforcement and they are located at boundaries of a wall. Use of boundary elements to increase ductility and energy dissipation of masonry shear walls has been studied in recent years (Shedid et al. 2010; Banting and El-Dakhakhni 2012; Cyrier 2012; Kingsley et al. 2014; Ezz et al. 2015).

M. Ezzeldin (2017) conducted reduced-scale tests on a two-story reinforced masonry (RM) shear wall building with confining boundary elements subjected to lateral cyclic loading to compare load-displacement hysteretic behaviour, ductility and energy dissipation with RM shear wall building with conventional rectangular cross-section. Figure 2.10 shows details of walls' cross sections and building configuration.

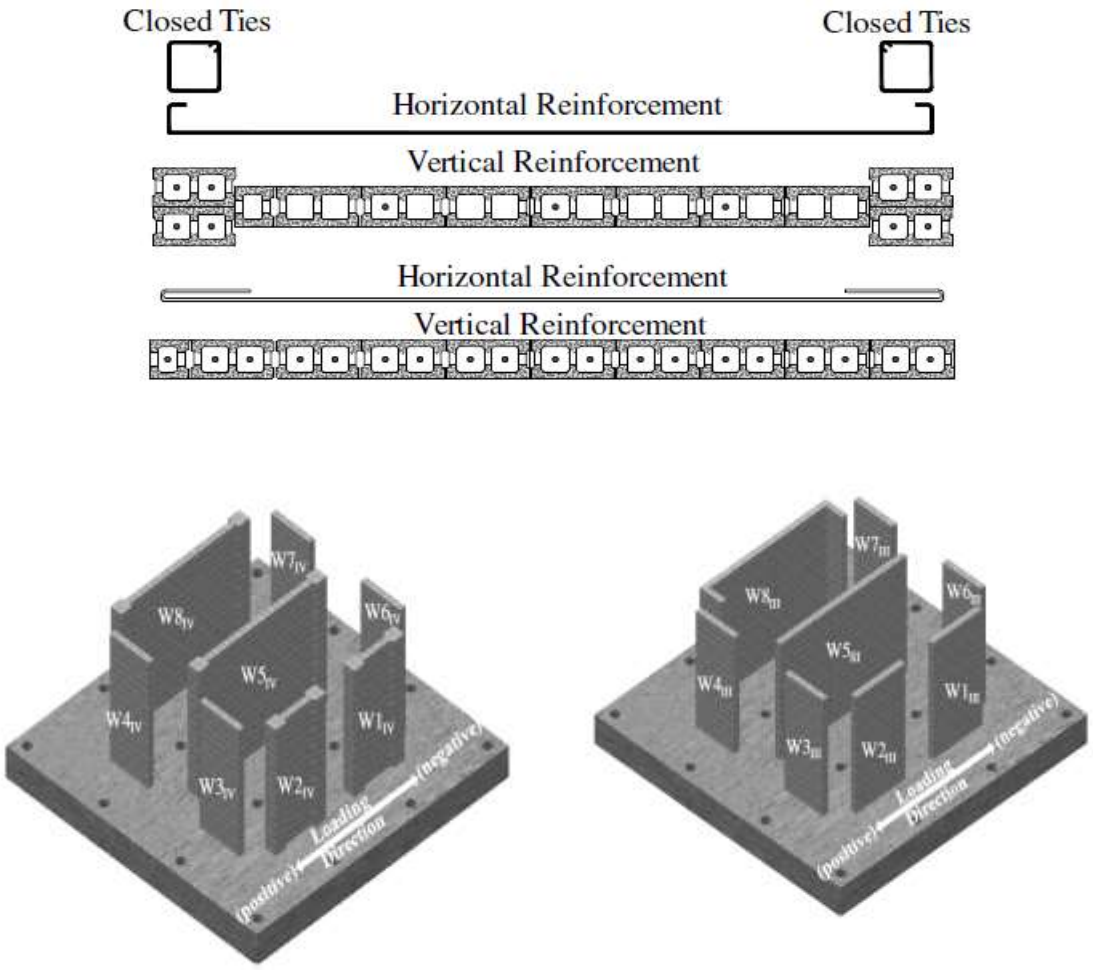

Figure 2.10. Buildings Configuration and Walls' Cross Sections

(Adapted from Ezzeldin 2017)

The results showed that the building with BEs dissipated more energy than the conventional one, 25% higher at a 3.5% drift level. While having the same elastic stiffness and ultimate capacity, the building with BEs was significantly more ductile than the conventional one and about 40% higher ductility was observed at 50% of their ultimate strength.

The increased ductility and energy dissipation characteristics of using BEs was also observed and reported by Shedid et al. (2010), and Banting and El-Dakhakhani (2012,

2014) through experimental testing of single and multi-storey masonry walls. Other benefits of using BEs also included the effective confinement of reinforcement provided by more grouting in BEs. This confinement delayed the vertical reinforcement buckling and thus the crushing of the grout core which was often failure trigger of conventional masonry shear walls. Additionally, spalling of face shell in the compression zone did not affect resistance. The studies also suggested that the ductility enabled by BEs in masonry shear walls justifies a need to provide a new category of RM walls with boundary elements to be used in seismic design. In the case of all-masonry infilled frames, the similarities with the boundary element shear wall construction lie in the boundary columns where masonry columns are formed with prototype boundary element units fully grouted and reinforced, and masonry beams are formed using bond beams and tied into columns. However, different from masonry shear walls, the uniqueness of all-masonry infilled frame systems is that they rely on combined frame-action and frame-to-infill interaction to achieve their lateral resistance, which can improve construction efficiencies by having large portions of masonry (in the infills) with little-to-no reinforcement.

2.5 SUMMARY

A considerable amount of research has been conducted on masonry infilled frames, mostly RC or steel frames, under in-plane loading. Many analytical models for calculating the stiffness and strength of this type of structural systems were proposed, several of which have been adopted in the current North American masonry design standards. This available information provides important technical background for the proposed all-masonry infilled frame systems. Noting the similarities and differences between the existing and proposed infilled frame systems, the study is to evaluate the effect of these similarities and

differences through an experimental study. The results are used to assess the validity of the existing analytical models when applied to the proposed all-masonry infilled system.

CHAPTER 3 EXPERIMENTAL PROGRAM

3.1 GENERAL

The experimental program was conducted to investigate the in-plane behaviour and strength of concrete masonry infill walls bounded by reinforced masonry frames. The results were used to evaluate its structural performance in comparison with conventional infilled RC frames. To that end, an experimental study on concrete masonry infilled RC frames subjected to in-plane lateral loading was conducted by two colleagues in the same research group (Steeves 2017, Hu 2015). The results of those two studies were used in the comparison study. To make the comparison valid, the geometry of the infill and frame, and main material properties of the infilled frame components of this study were kept consistent with the previous ones.

In this study, a total of six specimens were tested to failure under an in-plane lateral monotonic load applied at the frame top beam level. Along with testing of the infilled frames, auxiliary tests were also performed to determine the material properties of specimens' components including concrete masonry units, mortar, grout, concrete and reinforcing steel. In the following sections, detailed descriptions of infilled frame specimens, test set-up and procedure as well as auxiliary tests are presented.

3.2 INFILLED FRAME SPECIMENS

Table 3.1 presents a description of the test specimens. Six specimens included one bare frame (BF), one control specimen (IF-RS) and four specimens with varying parameters including infill material strength, infill reinforcement, and combined vertical and lateral loading. Two specimens were designed for infill reinforcement study (IF-BJ and IF-BB)

where IF-BJ had bed joint reinforcement implemented every other course in the infill and IF-BB had two bond beams implemented in the infill. One specimen was designed for infill material strength study (IF-RW) where the infill was constructed with weaker masonry blocks and mortar. One specimen was designed under combined vertical and lateral loading (IF-RS-A). A vertical load of 80 kN was selected for this study.

Table 3.1. Summary of Test Specimens

Number	Specimen ID	Mortar Type	Parameters
1	BF	Normal	-
2	IF-RS	Normal	Control Specimen
3	IF-RS-A	Normal	Vertical (80kN) + Lateral Loading
4	IF-RW	Weak	Weak Mortar and Blocks
5	IF-BB	Normal	Bond Beam At 3rd and 8th Courses
6	IF-BJ	Normal	Bed-Joint Reinf. at Every Second Course

All the masonry infills were constructed with a tight contact with the boundary frames. The geometry and dimensions for all the specimens are shown in Figure 3.1, yielding an infill height-to-length aspect ratio of 0.73.

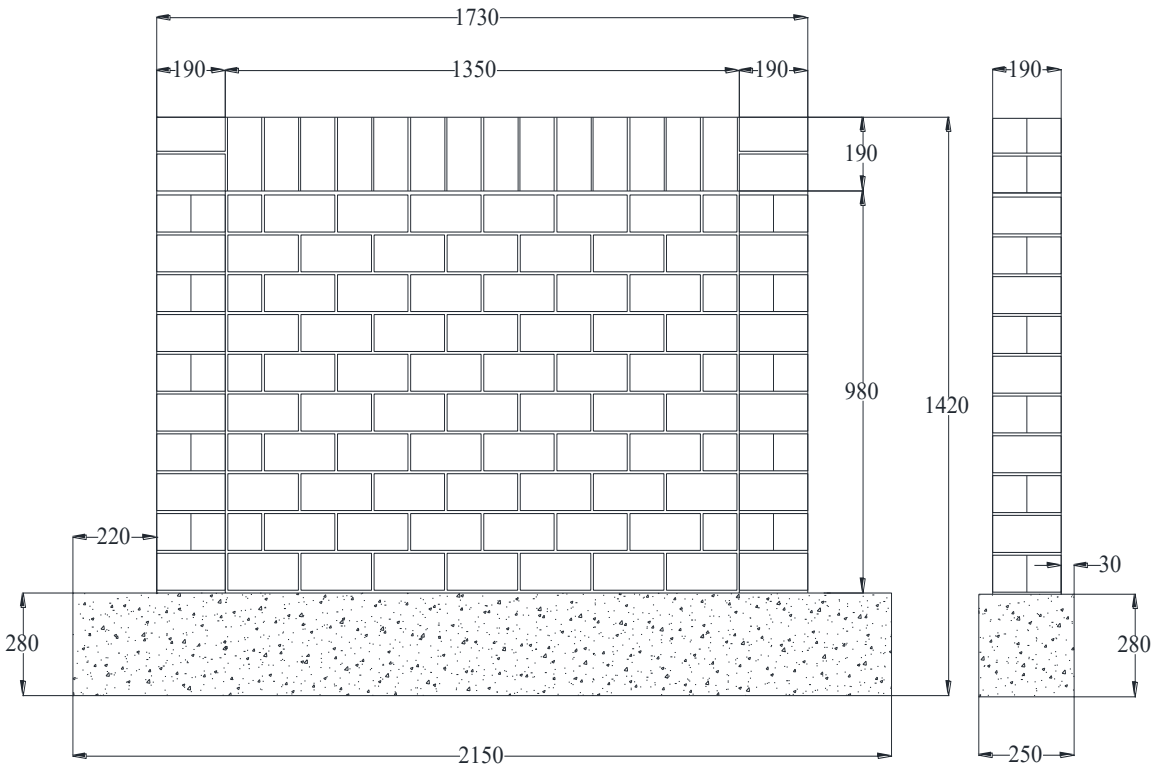

Figure 3.1. Geometric Properties of Infilled Frame Specimens (unit:*mm*)

All the masonry infills were constructed as un-grouted and unreinforced (no vertical reinforcement) using the custom-made, half-scale standard 200 *mm* CMUs. Figure 3.2 shows the nominal dimensions of the CMUs used. For boundary frames, 190x190 mm square sections were used for both columns and beams. The nominal dimension of the custom-made block used for boundary frame members is also shown in the figure. To achieve 190x190 mm sections, the block was cut on site to obtain the required dimension.

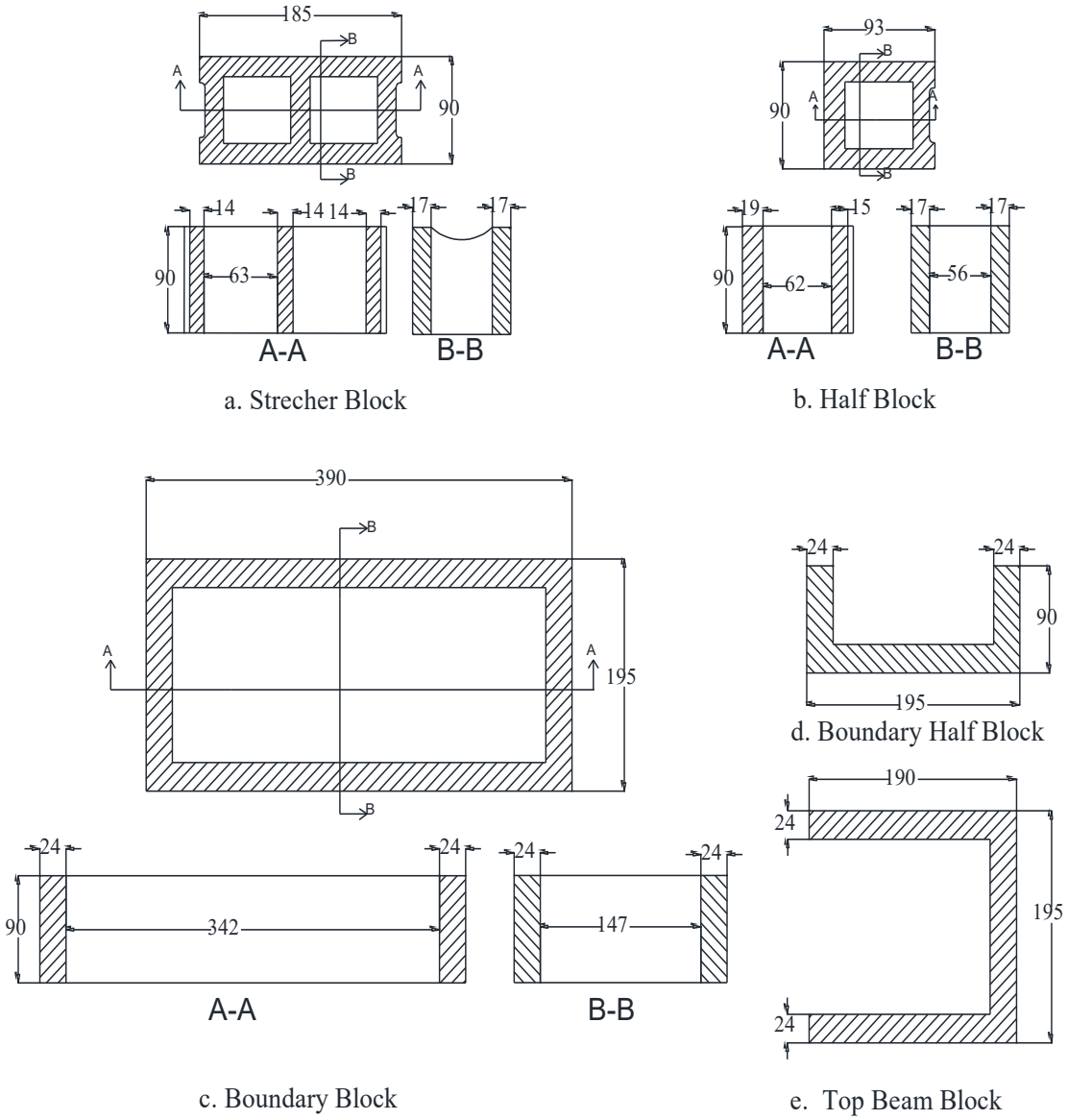

Figure 3.2. Geometry and Dimensions of CMUs (unit:*mm*)

Figure 3.3 shows the details of reinforcement in the boundary frame. The reinforcement scheme was also kept consistent with previous tests on the RC framed infills. In that case, the RC frame was designed in accordance with the Canadian concrete design code CSA A23-3 (2014) and the reinforcement detail including size, spacing, arrangement of longitudinal bars and stirrups complied with requirements to provide ductility and avoid brittle shear failure. As the dimension of the frame member and reinforcement details were

practically the same, it was then considered the masonry frame to be structurally ductile with a similar behaviour to the RC frame. The top beam and columns were reinforced with four 10M longitudinal deformed rebars and 10M square stirrups spaced at 100 *mm* centre-to-centre. The base beam had a 250x280 *mm* cross-section reinforced with four 15M longitudinal rebars confined by 10M stirrups spaced at 130 mm centre-to-centre. To strengthen the regions of beam-column connection, similar to RC frames, two 300 by 300 *mm* L-shaped 10M rebar were added at each top corner.

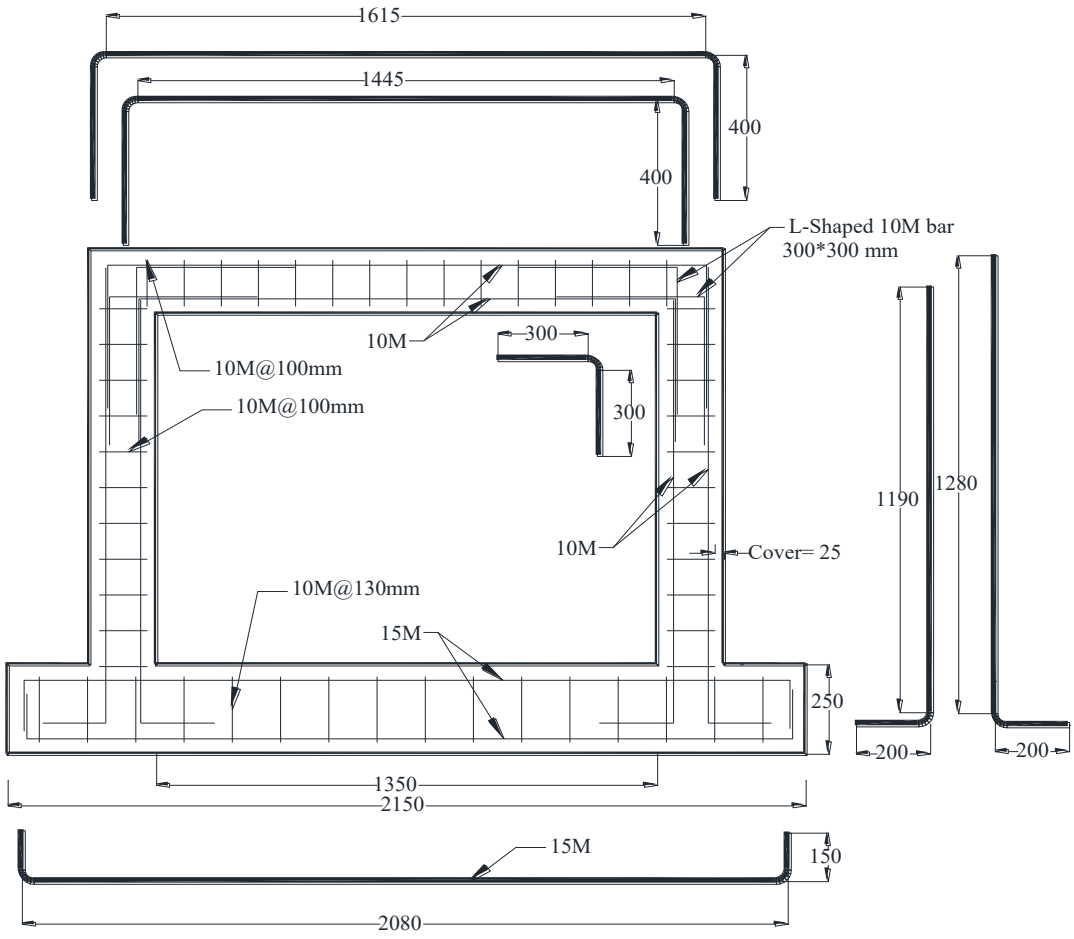

Figure 3.3. Reinforcement Detail (unit: *mm*)

3.3 CONSTRUCTION OF SPECIMENS

The construction of specimens consisted of two main phases, i.e., RC base beam construction, and construction of masonry frame and infill. Due to the uniqueness of masonry infilled masonry frames, the construction sequence is different from a conventional infilled RC frame. In the latter case, an RC frame is first cast and cured for 28 days which is followed by the construction of masonry infills. In this case, the RC base beam was first cast and cured for 28 days which was followed by a simultaneous construction of masonry frame and infill. The following sections provide descriptions of major steps involved in the two-phase construction.

3.3.1 Base Beam Construction

The first step to construct the base beam was to build its formwork. The formwork was constructed using plywood boards cut to specified geometry as shown in Figure 3.4.

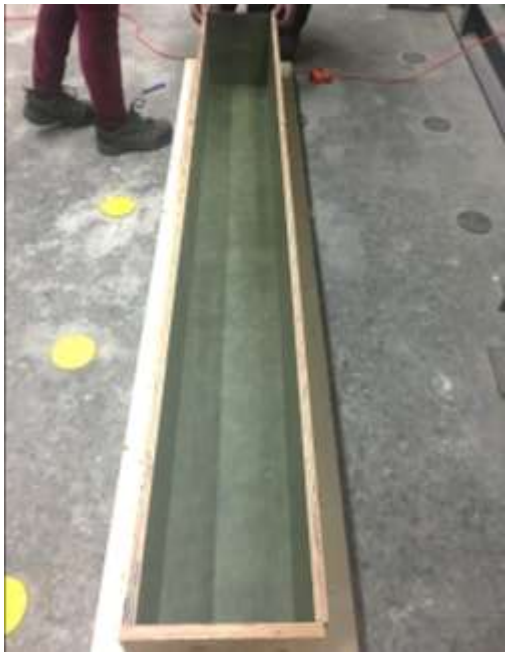

Figure 3.4. Base Beam Concrete Formwork

The base beam reinforcement was then formed into a steel “cage” (Figure 3.5), and the cage was carefully positioned into the formwork (Figure 3.6) while maintaining a 40 mm cover. Lastly, the vertical rebars of columns were tied into the base beam rebar cage before casting concrete (Figure 3.7).

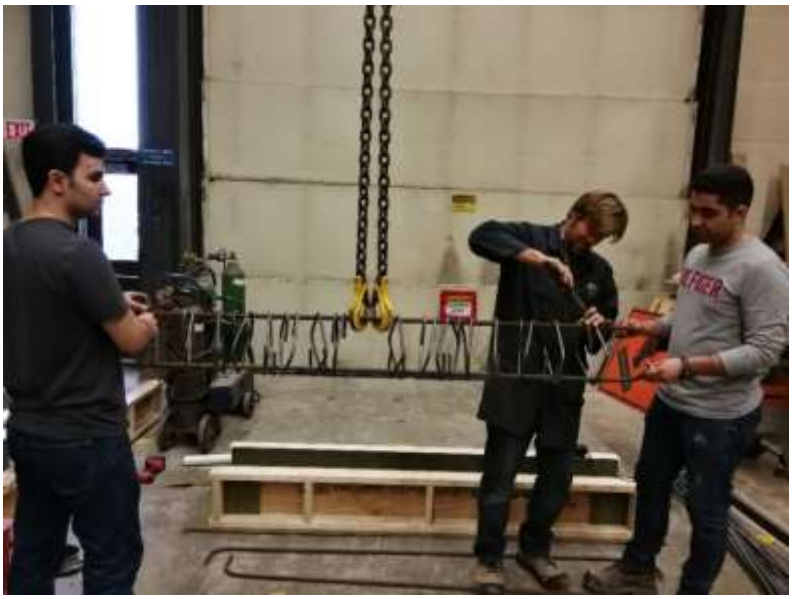

Figure 3.5. Base Beam Rebar Cage Fabrication

Figure 3.6. Base Beam Cage Placed in the Formwork

Figure 3.7. Base Beams with Column Rebar

The concrete used for the base beam was the ready-mix concrete with a specified compressive strength of 25 *MPa* and maximum aggregate size of 12 *mm*. The base beams for all specimens were cast on October 16, 2018. At each pour, concrete was sufficiently vibrated to minimize potential air pockets and voids. Onsite slump tests were performed before each pour in accordance with ASTM C143/143M (2015) Standard Test Method for Slump of Hydraulic-Cement Concrete. The average falling height of 153 *mm* was achieved which satisfied the required 150 *mm* base on the standard (Figure 3.8). Along with casting base beams, four 100 *mm* by 200 *mm* and three 150 *mm* by 300 *mm* cylinders were also cast for the concrete batch as part of the auxiliary test in accordance with ASTM C39/C39M (2016) (Figure 3.9).

Figure 3.8. In-Situ Slump Test

Figure 3.9. Pouring Cylinders

After pouring concrete, the base beams were covered with moist burlaps for 48 hours (Figure 3.10). The formwork was removed after 48 hours and the base beams were continued to be moist cured till the14th day from the day of pouring. After 14 days, the concrete was air-cured until the day of the test (Figure 3.11). The figure also shows that vertical rebars in position to receive masonry blocks for columns.

Figure 3.10. Curing with Moist Burlaps

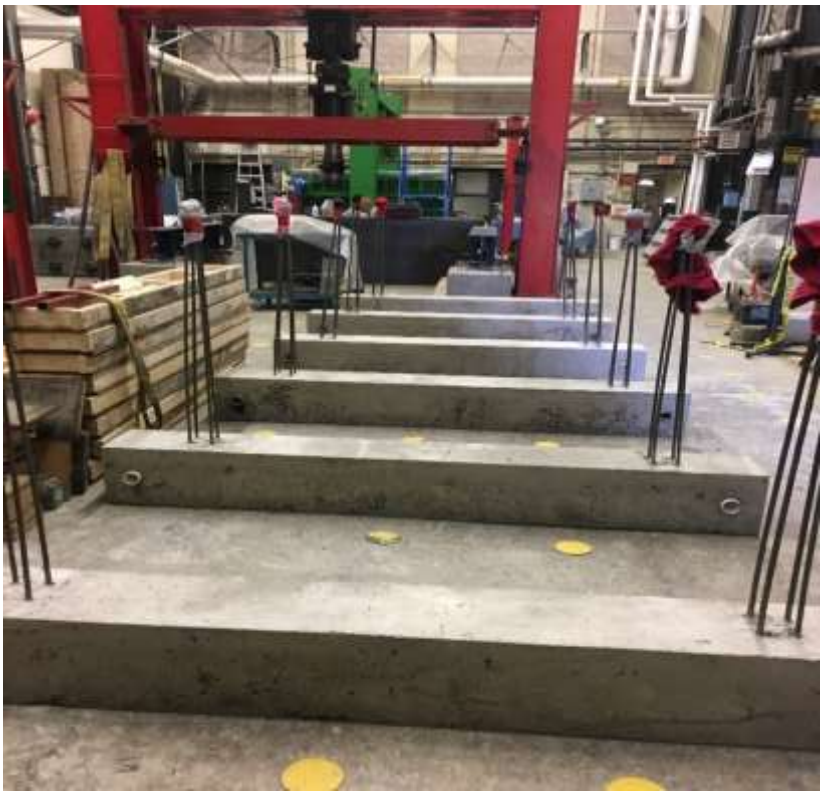

Figure 3.11. Air Curing

3.3.2. Construction of Masonry Frame and Infill

Figure 3.12 shows the general construction sequence for this phase which consists of tying stirrups on the column vertical rebars (a), construction of masonry columns and the infill simultaneously course by course (b), construction of masonry frame beam (c), grouting columns and beam (d), and curing (e). The construction commenced on December 17 and completed on December 21, 2018. The masonry portion was constructed by an experienced mason to the standard practice. The mortar was applied only on the face shell of blocks for both the bed joints and the head joints. At each course, the levelness and plumbness were checked and ensured before continuing to the next course (Figure 3.13). At the frame beam course, the block was turned 90 degrees to form a U-shape and set above the last infill course. A steel "cage" representing the beam reinforcement details built independently was

carefully positioned into the course with vertical rebars into the cavity of columns. The masonry grout was then poured into the cavities of both the beam and columns to form a monolithic frame. The grout was sufficiently vibrated to ensure it flows to the bottom of the columns as well as to remove air pockets. After pouring concrete, the specimen was moist cured within wrapped plastic sheets for 14 days. After that, they were all air-cured until the day of testing.

(a)

(b)

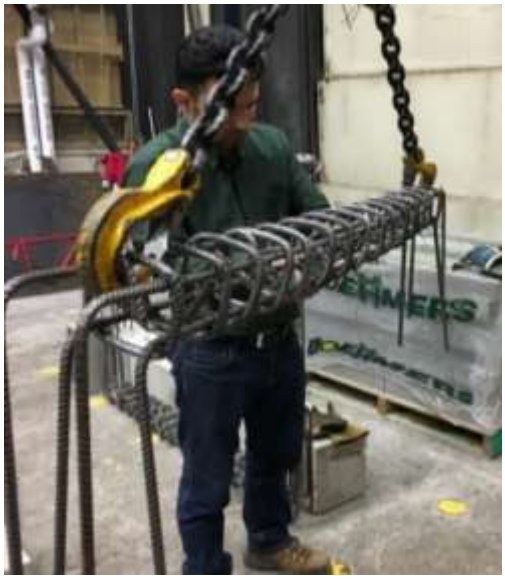

(c)

(d)

(e)

Figure 3.12. General Construction Sequence

Figure 3.13. Levelness and Plumbness Checking

The following sections provide further construction details for specimens which require special consideration during construction.

Construction of Specimen BF

As the bare frame has no infill to support the frame top beam, a shoring system consisting of wooden planks was installed during curing, as illustrated in Figure 3.14.

Figure 3.14. Bare Frame Specimen Construction

Construction of Specimen IF-BJ

The ladder-type joint reinforcement was used as the bed-joint reinforcement for specimen IF-BJ. The mesh was made of 5 *mm* wires and with a width of 70 mm resting in the middle

of the face shell of the course, as shown in Figure 3.15. The reinforcement was placed on every other course starting at the second course and it was extended into the column to form a bond as shown in Figure 3.16.

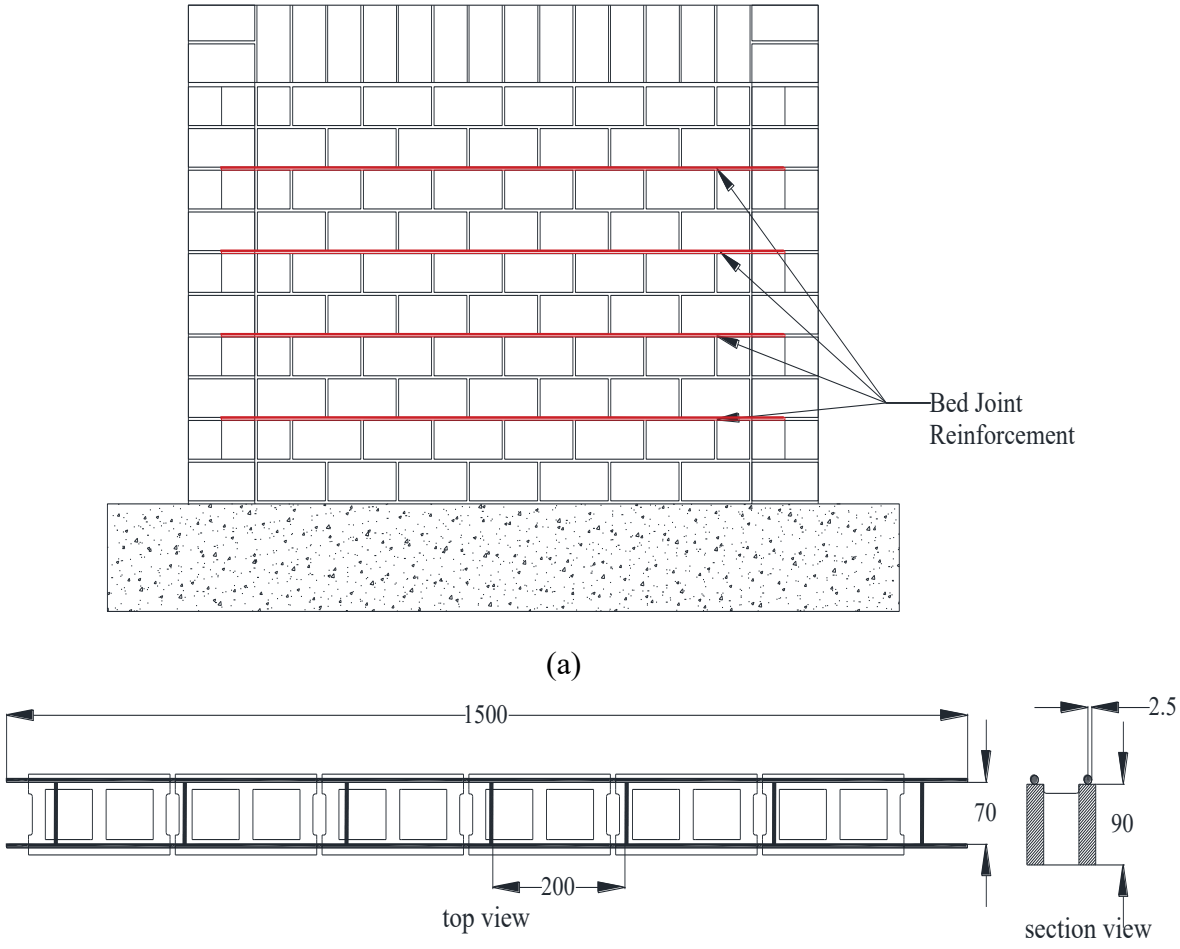

Figure 3.15. Bed-Joint Reinforcement Detail

(a)

(b)

Figure 3.16. Bed-joint Reinforcement Extension into the Column

Construction of Specimen IF-BB

The all-masonry infilled frames make the implementation of bond beams through the infills possible. For this specimen, two singly reinforced bond beams were constructed at the 3rd and 8th courses, as shown in Figure 3.17. The webs of masonry blocks for that course were first cut to desired depth to accommodate the steel rebar through the length of the course. As shown in Figure 3.18, before placing the 3rd or 8th course, the cavities of lower courses were blocked to prevent running the grout into the lower courses (a). The bond beam rebar (10M rebar) was positioned in the course and its end were bent 90 degrees to be extended into the columns (b). Lastly, grout was poured, and surface was smoothed before moving to the next course (c).

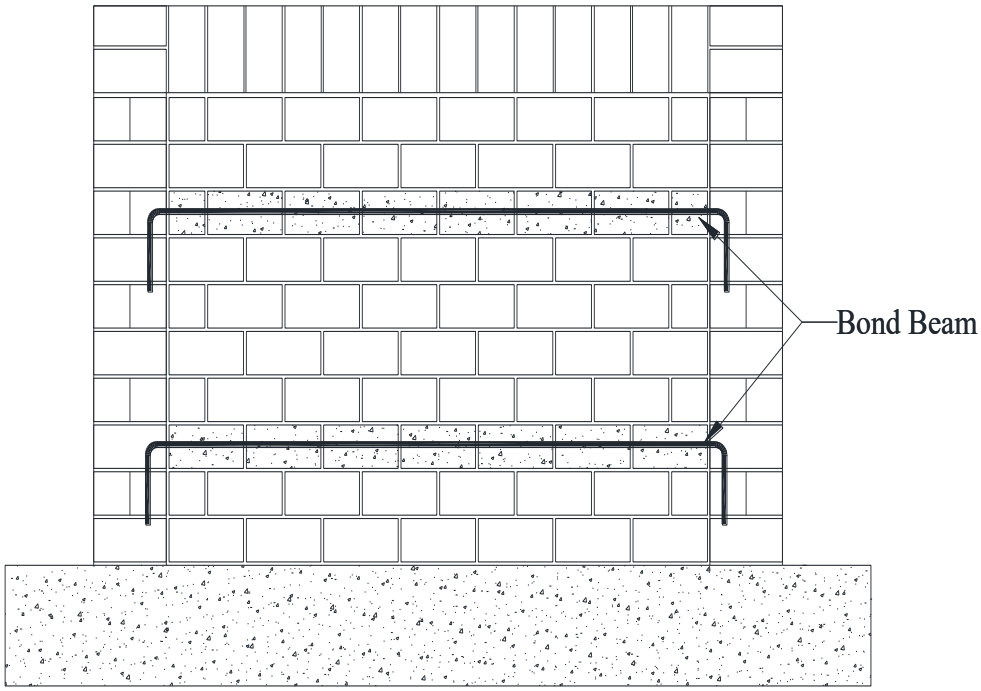

(a)

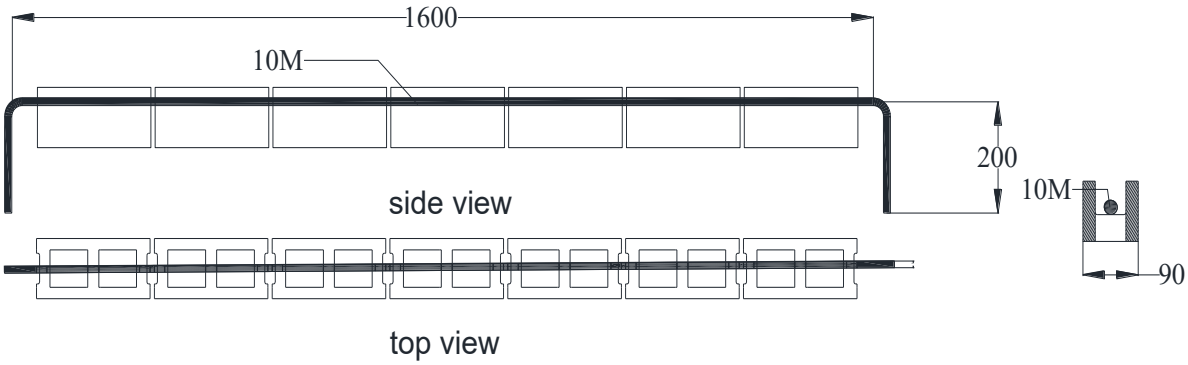

(b)

Figure 3.17. Bond Beam Detail

(a)

(b)

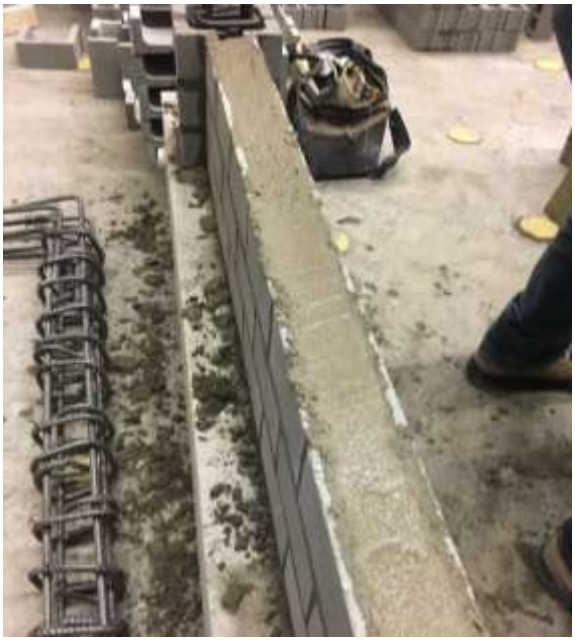

(c)

Figure 3.18. Bond Beam Construction

3.4 TEST SET-UP

3.4.1 Lateral Loading Setup

All specimens were subjected to in-plane lateral loading applied at the frame top beam level. The overall setup and schematic of test setup are shown in Figure 3.19 and 3.20, respectively. This load was applied monotonically using a hydraulic actuator with a capacity of 250 *kN*. The actuator was reacted against the column

Figure 3.19. Overall Test Setup

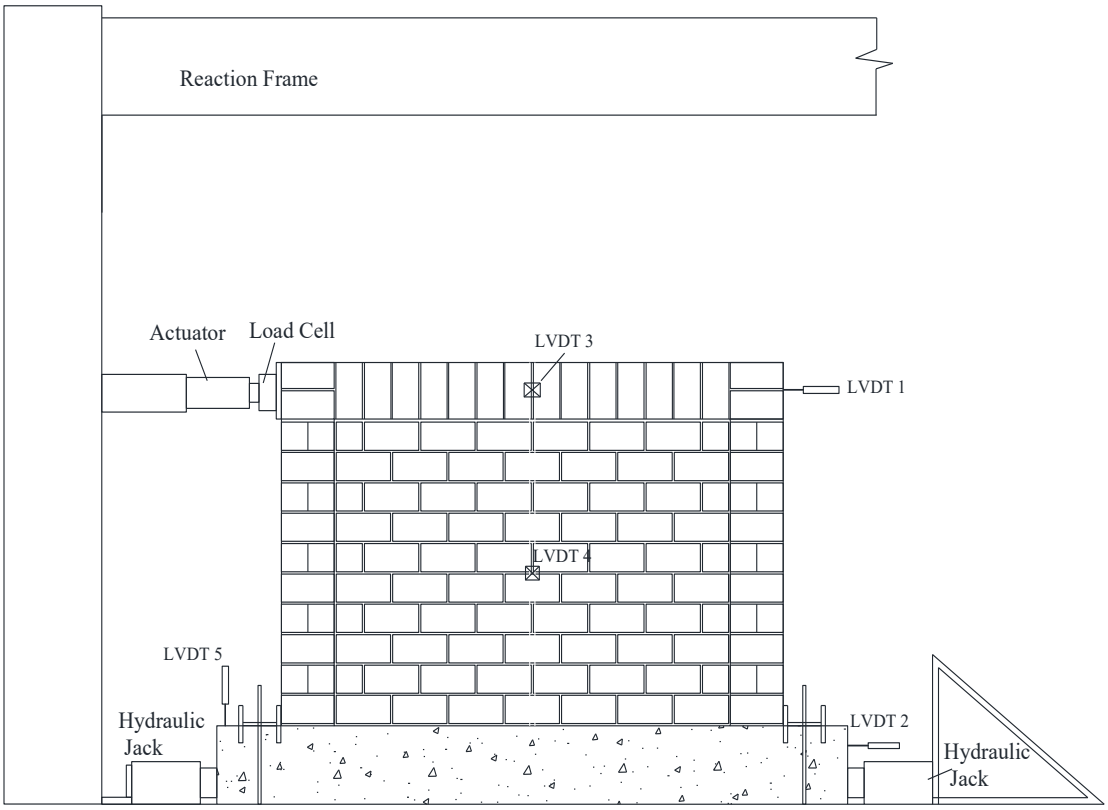

Figure 3.20. Schematic of Lateral Loading Test Setup

of an independent reaction frame (Figure 3.21(a)). A load cell, attached to the head of the actuator, was used to monitor the load throughout the loading history. A steel plate was mounted between the load cell and the frame top beam to distribute load evenly to the loading point, preventing potential masonry local crushing, as shown in Figure 3.21(b). To provide the fixity of the frame base, the base beam of the frame was clamped down to the strong floor with two W steel beams through 40 mm threaded rods (Figure 3.22). The base beam was further braced against any potential sliding using a hydraulic jack on each end against the column of the reaction frame, as shown in Figure 3.23.

(a)

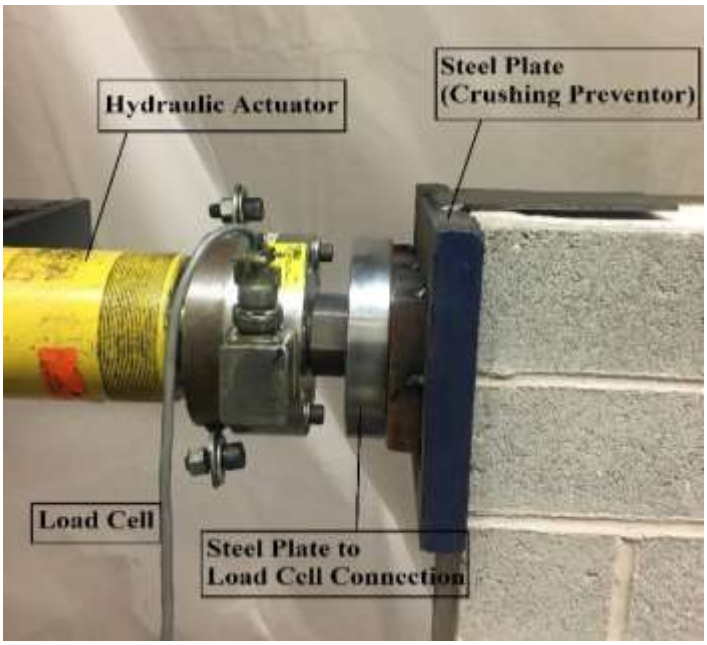

(b)

Figure 3.21. Actuator to Top Beam Connection Detail

(a) (b)

Figure 3.22. Top and Side View of Beam to Floor Clamping Connection

(a) (b)

Figure 3.23. Hydraulic Actuator to Brace the Base Beam

3.4.2 Vertical Loading Setup

Vertical loading setup was only required for specimen IF-RS-A which was subjected to combined vertical and lateral loading. Figure 3.24 and 3.25 show the overall vertical load setup. The vertical load was applied to the masonry infill through the masonry beam at two loading points approximately at the one-third of the infill length. To achieve this loading scheme, a hydraulic jack was used with one end reacted against the cross-head of the independent frame while the other end was reacted against a steel spreader beam. To facilitate the relative movement between the spreader beam and the masonry specimen when the in-plane loading was applied, the spreader beam was rested on an assembly of rollers at two loading locations. A pivot was installed between the actuator and the spreader beam at the loading point to accommodate the potential rotation of the spreader beam in the vertical direction. Figure 3.26 shows a close-up of the vertical loading arrangement.

Figure 3.24. Combined Vertical and Lateral Loading Setup

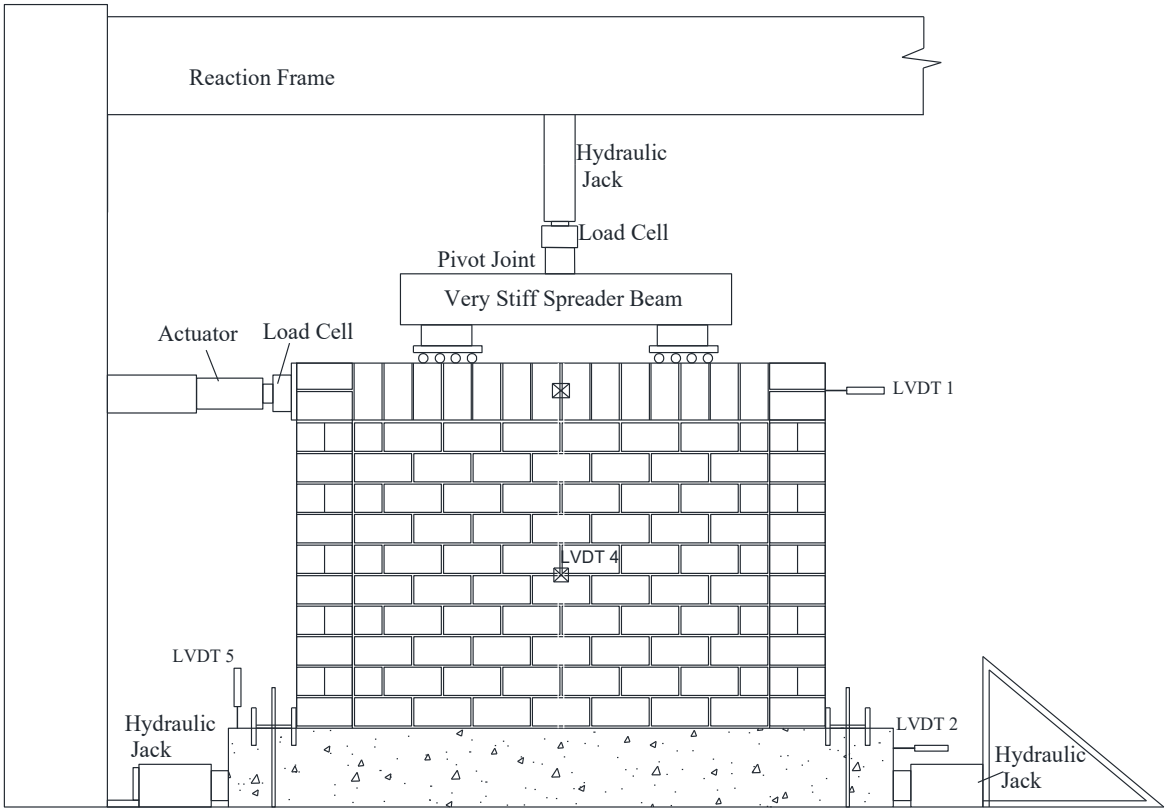

Figure 3.25. Schematic of Vertical and Lateral Loading Test Setup

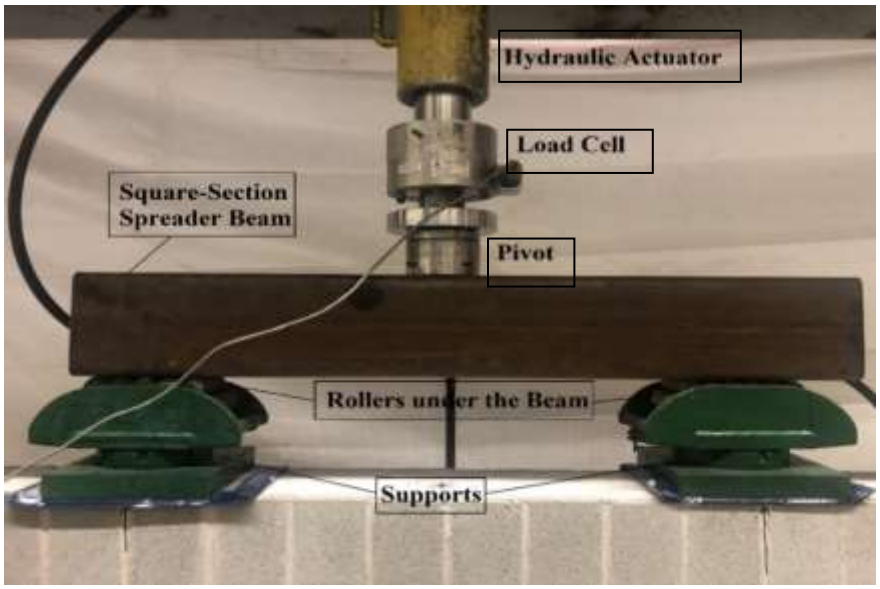

Figure 3.26. Vertical Load Arrangement Detail

3.4.3 Displacement Transducers Arrangement

Five linear variable differential transformers (LVDTs) were used to monitor the specimen displacements. Two LVDTs were used to measure the lateral displacements, where LVDT 1 and 2 were mounted to measure the top frame beam and base beam lateral displacements respectively (Figure 3.27(a)). Two LVDTs were used to monitor potential out-of-plane displacements of the specimen where LVDTs 3 and 4 were mounted at the mid-point of the top frame beam and the center of infill, respectively (Figure 3.27(b)). The LVDT 5 was placed at the bottom beam at the loading side of the specimen to monitor the potential uplift of the specimen (Figure 3.27(c)).

(a)

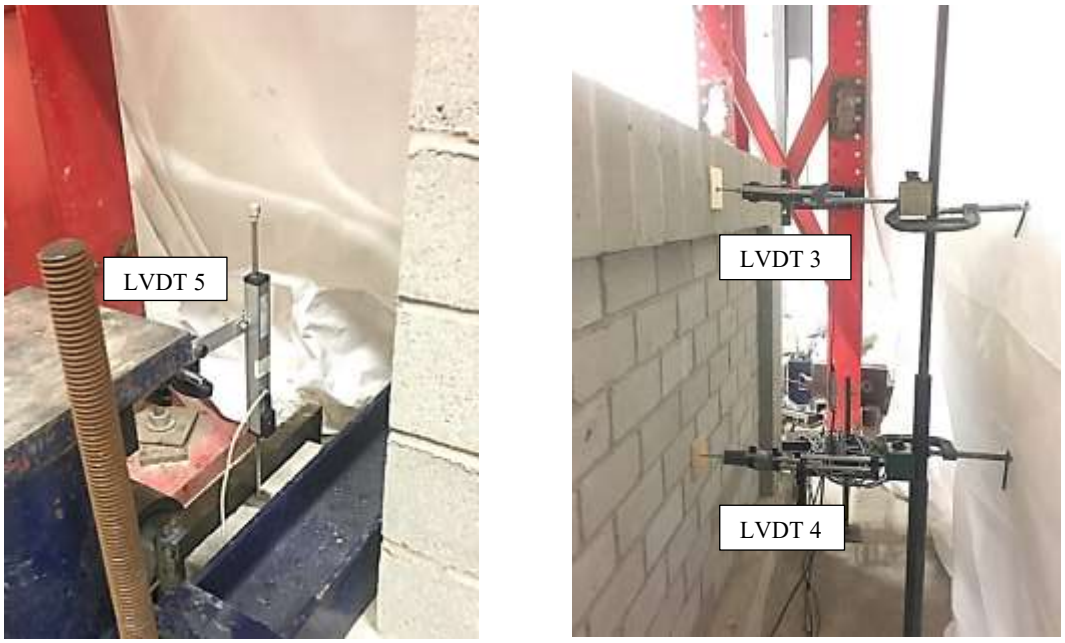

(b) (c)

Figure 3.27. LVDTs Arrangement Detail

3.5 TESTING PROCEDURE

Prior to each test, the specimen was transported to the testing location. Care was taken to ensure that the specimen was positioned at the center of both the lateral and vertical loading setup. The load cell(s) and displacement transducers were mounted and checked to ensure that they worked properly and zeroed for initial recording. All the specimens except IF-RS-A were subjected to in-plane loading until failure. The in-plane loading was gradually increased at a loading rate of approximately 6 *kN* per minute. The load cell and all LVDTs were set to record data at a 0.1 second interval using an electronic data acquisition system. For specimen IF-RS-A under combined vertical and lateral loading, the test began with applying the vertical load gradually using a hand pump to 80 *kN* and held constant. The lateral load was then applied in the same manner as described above. The vertical load level fluctuated as the frame deformed and specimen stiffness changed, but the fluctuation was

kept around 5% by operating the hand pump throughout the loading history. During each test, the cracking load, ultimate load, cracking pattern and failure mode were recorded and marked throughout the loading history.

3.6 AUXILIARY TESTS

Concurrent with the testing of frame specimens, auxiliary tests were carried out to obtain the material properties of CMUs, mortar, grout, masonry prims, and reinforcing steel. The test setup and procedures of those tests are described in the following sections.

3.6.1 CMUs

Both physical properties and compressive strength of masonry infill CMUs were determined in accordance with ASTM C140/C1140M (2018) “Standard Test Methods for Sampling and Testing Concrete Masonry Units and Related Units”. To that end, a minimum three blocks were randomly selected from the CMUs batch used in this study and tested. Physical properties obtained included 24-hour percentage absorption, moisture content, and density. Compressive strength was obtained using the Instron universal testing machine as seen in Figure 3.28 where a block is in position to be loaded in compression.

(a)

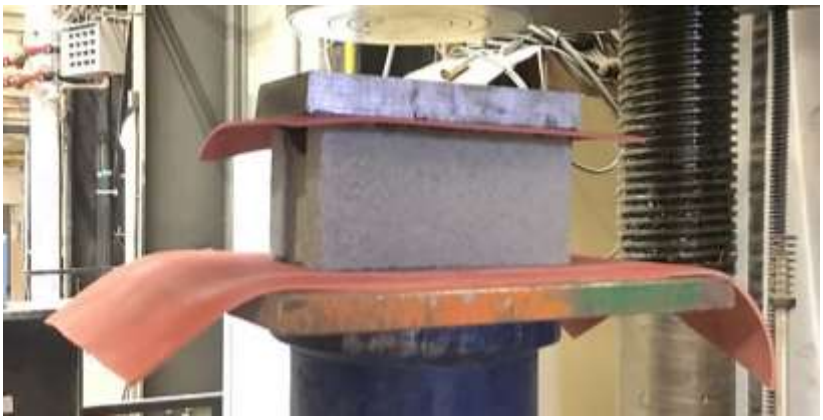

(b)

Figure 3.28. Compression Test Setup for CMUs. (a) Boundary Block, (b) Infills Block

3.6.2 Mortar

Two mortar mixes were used in constructing specimens. For all specimens except IF-RW, Type S mortar was used where Portland cement, Type N masonry cement, and sand were mixed with a respective weight ratio of 1:3:12 in accordance with ASTM C270 (2014) Standard Specification for Mortar for Unit Masonry. For specimen IF-RW, weak CMUs were used, and thus weak mortar was intended to achieve a weaker masonry strength. In this case, a mortar mix with a weight ratio of 0.7:4:20 of Portland cement, Type N masonry cement, and sand was used. A total of 16 batches of mortar was mixed to construct all specimens. For each batch, an average of six mortar cubes were cast, as seen in Figure 3.29. Table 3.2 provides a summary of mortar batch numbers used for each specimen. After being cured in a moisture room for 48 hours, the samples were moist-cured in the same manner as the specimen for another 14 days and then air-cured until the day of test. The samples were tested using the Instron universal testing machine on the day that the corresponding specimen was tested (Figure 3.30)

Table 3.2. Batch Numbers Used for Each Specimen

Specimen ID	Mortar Type	Mortar Batch Numbers
BF	Normal	N 9,13
IF-RS	Normal	N 5,6,7,8
IF-RS-A	Normal	N 10,11,12,13
IF-RW	Weak	W 1,2,3,4
IF-BB	Normal	N 14,15,16
IF-BJ	Normal	N 1,2,3,4

Figure 3.29. Sampling Mortar Batches in 2 in. Cubic Molds

Figure 3.30. Mortar Samples under Compression Test

3.6.3 Grout

A total of 11 grout batches was mixed according to ASTM C476 (2018) Standard Specification for Grout for Masonry with a weight ratio of 1:3 for Portland cement and sand, respectively. Table 3.3 presents a summary of grout batch numbers used for each specimen boundary frame. The grout batches used for bond beams is also mentioned in the table. Three samples were cast from each batch in accordance with ASTM C1019 (2018) Standard Test Method for Sampling and Testing Grout, as shown in Figure 3.31. All samples were kept moist under a plastic cover for seven days before removed from the molds. They were then cured in the same condition as the specimen before the testing.

Figure 3.32 shows a grout sample in the Instron universal testing machine to be tested for compressive strength.

Table 3.3. Grout Batch Numbers for Each Specimen

Specimen ID	Grout Batch Number
BF	B 6,7,8
IF-RS	B 2,6
IF-RS-A	B 4,5
IF-RW	B 3,4
IF-BB	B1(3rd Course), B3(8th course), B 9,10
IF-BJ	B 10,11

Figure 3.31. Grout Sampling

Figure 3.32. Grout Samples for Compression Test

3.6.4 Masonry Prism

For each infilled specimen, at least three masonry prisms were constructed resulting in a total of 15 masonry prisms. They were constructed according to ASTM C1314 (2016) Standard Test Method for Masonry Prisms. Constructed alongside the corresponding specimens, all prisms were 3-high and constructed in the same manner as the specimen where the middle course consisted of 2 half blocks, as shown in Figure 3.33. The mortar was applied on the faceshell of the masonry blocks at the bed joint and head joint to be consistent with the specimen. After construction, they were cured in the same condition as the specimen until the day of testing. For the compression test, they were capped with fiberboard on loading surface and loaded in compression in the Instron universal testing machine.

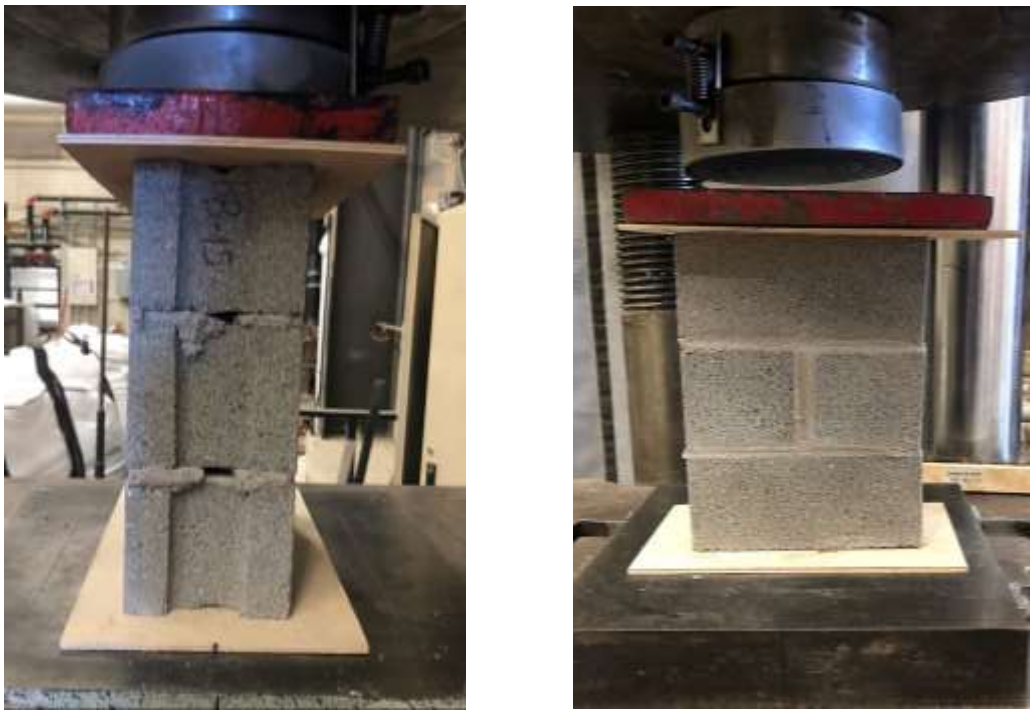

(a) (b)

Figure 3.33. Capped Prism Samples in the Instron Machine

3.6.5 Concrete Cylinders

Four 100 by 200 *mm* and one 150 by 300 *mm* concrete cylinders were cast alongside the base beams of all specimens. The smaller samples were cured in the moisture room for 28 days and then tested to measure the 28-day compressive strength of the concrete. The large cylinder was first cured in the moisture room for 28 days and then were kept in the same condition as the specimens. The three large cylinders were tested to determine the compressive strength and modulus of elasticity of concrete at the day of specimen testing. All the sampling, curing and testing procedure were in accordance with ASTM C39/C39M (2018) Standard Test Method for Compressive Strength of Cylindrical Concrete Specimens. Figure 3.34 shows the setup of the cylinder in the Instron universal testing machine.

Figure 3.34. Compression Test Setup for Concrete Cylinder

3.6.6 Reinforcement

3.6.6.1 Reinforcement for the boundary frame

Since the reinforcement used in this study was from the same batch as used in a previous experimental study (Hu 2015), the reinforcing steel data was collected from that study. To obtain material properties, three steel coupons were cut from randomly selected 10M longitudinal rebars and tested using the Instron universal testing machine. Figure 3.35 presents the details of the reinforcing coupons used. As it is shown in Figure 3.36 an extensometer was mounted on the coupon to measure the strain during the loading. All the sampling and testing procedure were in accordance with ASTM E8 (2016) Standard Test Methods for Tension Testing of Metallic Materials.

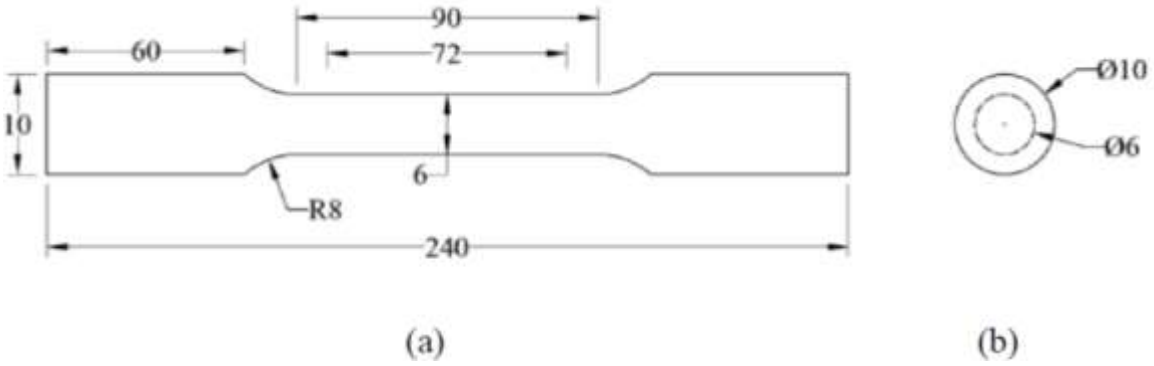

Figure 3.35. Steel Coupon Detailing (Hu 2015)

Figure 3.36. Tension Test Set-up for Steel Coupons (Hu 2015)

3.6.6.2 Bed Joint Reinforcement

The bed joint reinforcement was made of 5 *mm* steel round wire in the ladder type. Figure 3.37 shows the dimension detail of the tensile coupons. Due to the small diameter of the coupon, the existing Instron machine does not have adequate grip fixture to test. The

physical test of the joint reinforcement was not conducted. The mechanical properties provided by the manufacture's specification were used and they satisfy the minimum requirement contained in ASTM A951/A951M (2016) Standard Specification for Steel Wire for Masonry Joint Reinforcement.

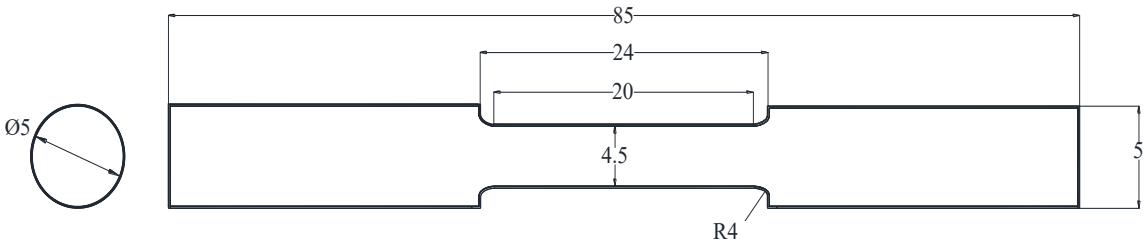

(a)

(b)

Figure 3.37. Bed Joint Reinforcement Coupon Detail

CHAPTER 4 EXPERIMENTAL RESULTS

4.1 INTRODUCTION

This chapter presents the results obtained from infilled specimen tests as well as auxiliary tests. The infilled specimen results include failure mode, load vs. displacement response, stiffness, lateral strength, and ductility of each specimen. Auxiliary test results include physical and mechanical properties of the CMUs, mortar, grout, masonry prisms, concrete, and boundary frame and bed-joint reinforcing steel.

4.2 INFILLED FRAME SPECIMEN RESULTS

This section first describes the general behaviour, through which a few terminologies that are used throughout the later discussion are defined, and then presents the failure mode, and lateral load vs. displacement response for each specimen. Finally, the effects of infill strength, infill reinforcement and vertical load on the lateral behaviour and strength is discussed.

4.2.1 General Behaviour of Specimens Subjected to In-Plane Loading

A general view of the load vs. displacement responses of the infilled specimens shows that there are four distinctive phases on the response curve. Using specimen IF-RS as an example, as shown in Figure 4.1, the first phase corresponds to the initial portion of the response curve. The slope of this portion, often linear, is defined as the initial stiffness (K_{ini}). At the end of phase one, the response curve showed the onset of non-linearity, usually indicating some form of cracking occurred in either masonry frame or infill. However, this cracking is not necessarily visible. The second phase covers the region from the initial cracks to the load that first significant crack is observed (P_{cr}). At this point, a

marked load drop is often observed on the curve along with experimental observation of visible cracking. The cracking stiffness (K_{cr}) represents the slope of the line connecting the origin to the point where the first significant crack occurs. Phase three covers the region from P_{cr} to the ultimate load (P_{ult}). The slope of the line connecting the origin to the point of P_{ult} is defined as the ultimate stiffness (K_{ult}). Within this region, several load drops followed by load increases are commonly observed, indicating that the masonry infills establish alternative paths for resisting the load as the cracks develop and progress in the infill. Phase four represents the region of unloading, from P_{ult} to the point where loading was discontinued. In most cases, the load was reduced to less than 80% of the P_{ult} when the test was stopped. The displacements corresponding to the linear portion of the curve, first significant crack load, ultimate load, and final failure are defined as Δ_{ini}, Δ_{cr}, Δ_{ult}, and Δ_{fail}, respectively.

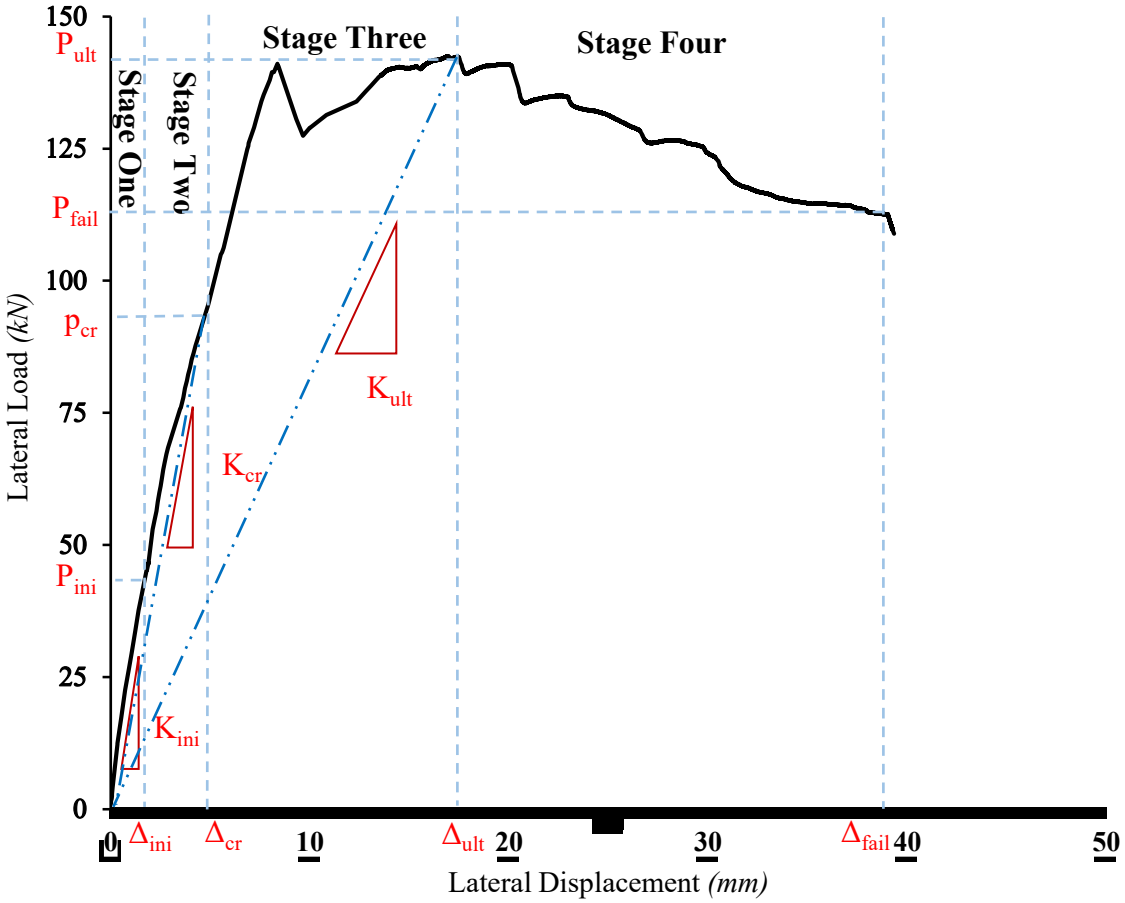

Figure 4.1. Lateral Load vs. Displacement Curve of Specimen IF-RS

4.2.2 Behaviour and Failure Mode

This section first provides a summary of failure modes for all specimens as shown in Table 4.1, which is followed by detailed descriptions of failure initiation, development and final failure mode as well as load vs. displacement response for each specimen.

Table 4.1. Summary of the Failure Mode

Specimen ID	Failure Initiation	Final Failure Mode
IF-RS	DC	DC
IF-RW	DC	DC+SS
IF-RS-A	DC	DC
IF-BB	SS	SS
IF-BJ	DC	DC
BF	Crack at the loaded beam-column intersection	Tension crack failure on the left column

Note that SS and DC stand for shear sliding and diagonal tension cracking, respectively. One important observation is that failure initiation mechanism for most specimens was by diagonal cracking (DC) which also remained as the final failure mode for all except one. Interestingly, unlike masonry infilled RC frames whose failure are likely governed by corner crushing, no evident corner crushing was observed in this case.

4.2.3 Masonry Bare Frame (BF)

Figure 4.2 shows the final crack pattern at failure. Ultimately, the frame failed (when the load dropped) as the course detachment occurred in the lower courses of the left column, as can be seen in the figure. The first significant crack occurred on the left column-beam connection at 24.5 *kN* (Figure 4.3(a)). As the load increased, more tension cracks developed on the left surface of the left column and these cracks were through mortar joints (Figure 4.3(b)). Visible cracking also developed in two areas, i.e., the left top corner and the bottom right corner as seen in Figure 4.3 (a) and (c) where the former was largely due to the stress concentration at the loading point and the latter was due to the combined shear and

compression (vertical cracks). With further increase in load, more cracks appeared on the top beam grout developing through the joints mortar between the beam lintel blocks (Figure 4.3(d)). At failure, the bed joint cracks on the left column close to the bottom courses penetrated through the entire width of the mortar joint and the bottom course faceshell spalled out (Figure 4.3(e)). The overall deformation of the frame is clearly visible showing a marked uplift of the left column.

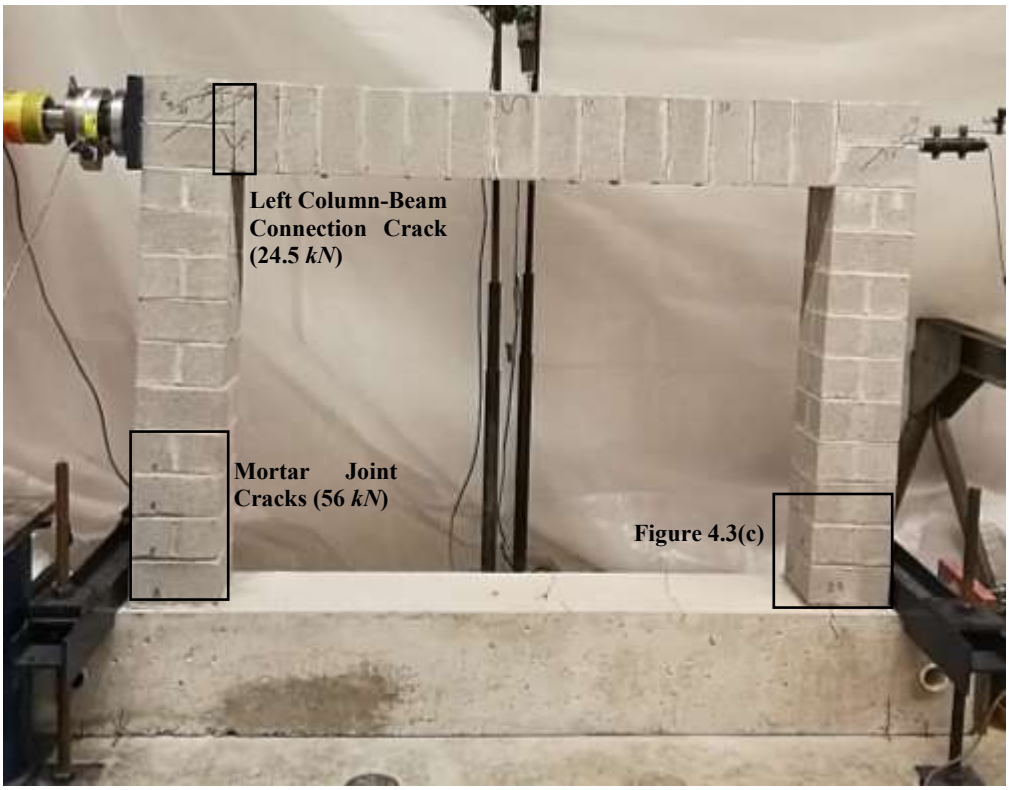

Figure 4.2. Final Crack Pattern of the Masonry Bare Frame

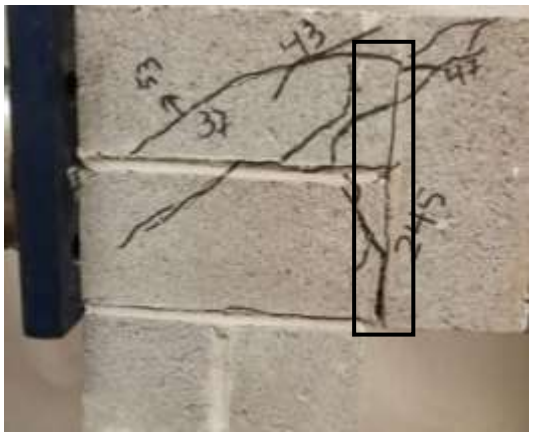

(a) Left Column-Beam Intersection Crack

(b) Left Column Mortar Joint Crack

(c) Right Column Bottom Courses Cracks

(d) Grout Cracks on the Top Beam

(e) Mortar Joint Cracks and Faceshell Spalling of the Left Column

Figure 4.3. Masonry Bare Frame Failure Pattern

Figure 4.4 illustrates the load vs. displacement curve of the bare frame. The curve showed a noticeably ductile behaviour where the nonlinearity began at quite early stage of loading and the ultimate load was maintained over a relatively large displacement (25 to 38 *mm*). It appears to have a similar behaviour trend as a RC frame of a similar geometry and reinforcing details. Detailed comparison is discussed later in Chapter 5.

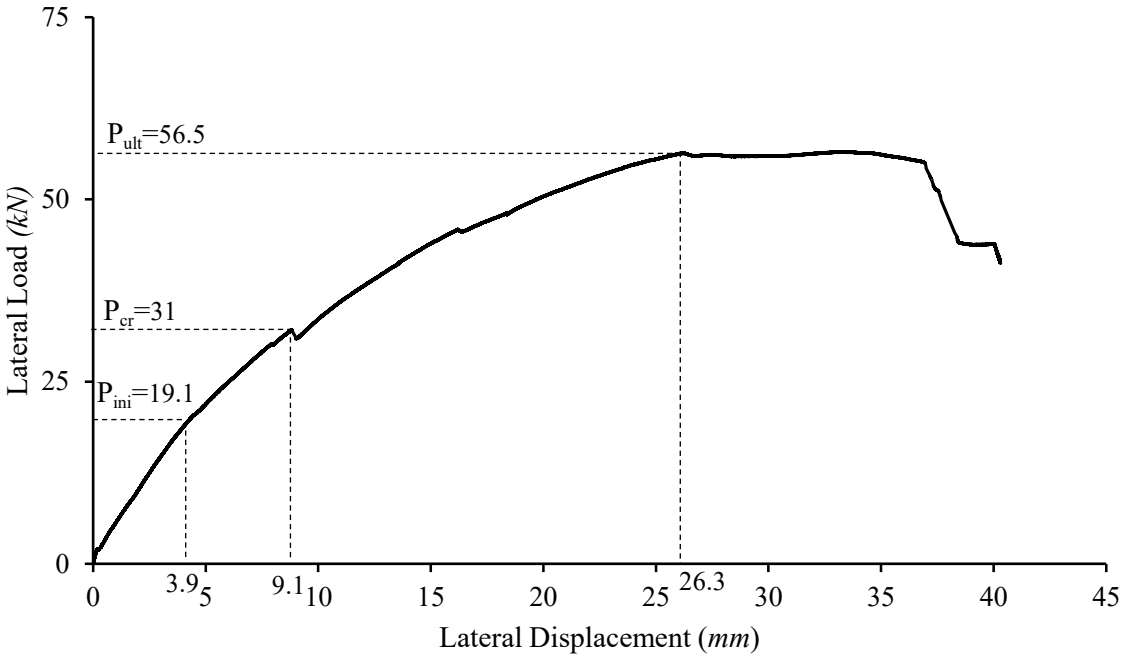

Figure 4.4. Lateral Load vs. In-Plane Displacement Curve of the Bare Frame

4.2.4 Specimen IF-RS

Specimen IF-RS was tested as the infilled control specimen. Figure 4.5 shows the failure mode and Figure 4.7 shows the load vs. displacement response. Similar to the infill in a RC frame, significant diagonal cracking was observed in the infill. Small hairline cracks began to occur at the left infill-to-column interface at the load of 42.6 *kN* (Figure 4.7) when the response curve showed onset of nonlinearity. The first significant crack occurred at 93.4 *kN* through mortar joints. The second significant crack appeared around 130 *kN* at the

right half of the infill and extended towards the upper left corner and lower right corner as load increased. At the load of 142 *kN,* a sudden wide fracture occurred on the top beam as seen in Figure 4.6, causing a 13 *kN* load drop in the load-displacement curve. The frame however continued to deform while maintaining the load at about 140 *kN*. At 20 *mm* of displacement, the load began to drop and severe cracking was also seen at the bottom of the right column. It appears that the second crack developed through the infill and extended to the top beam and right column. It is noted that the specimen still showed marked ductility post-ultimate where no abrupt or sudden drop of load was observed.

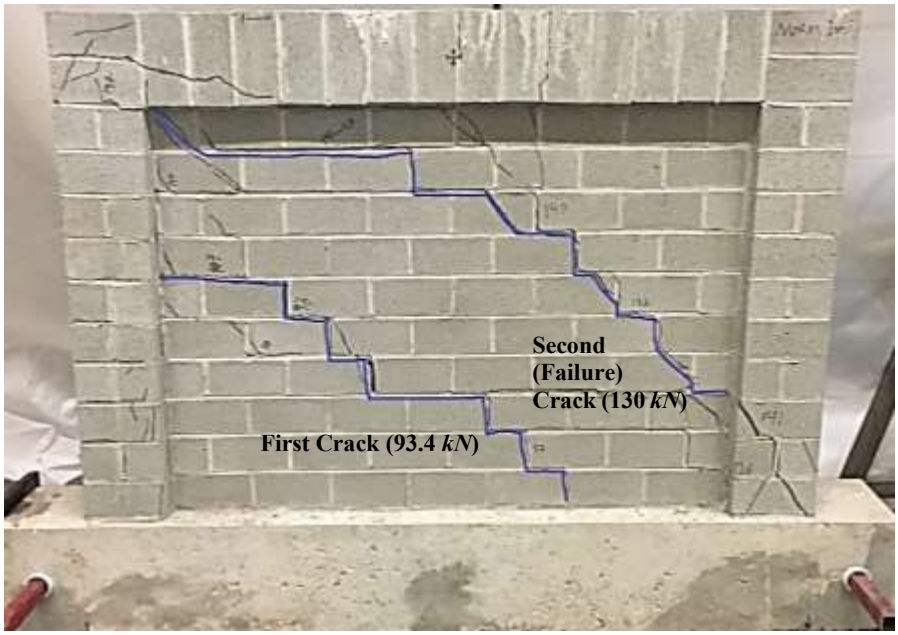

Figure 4.5. Final Failure Pattern of IF-RS

Figure 4.6. Fracture Crack on the Top Beam of IF-RS

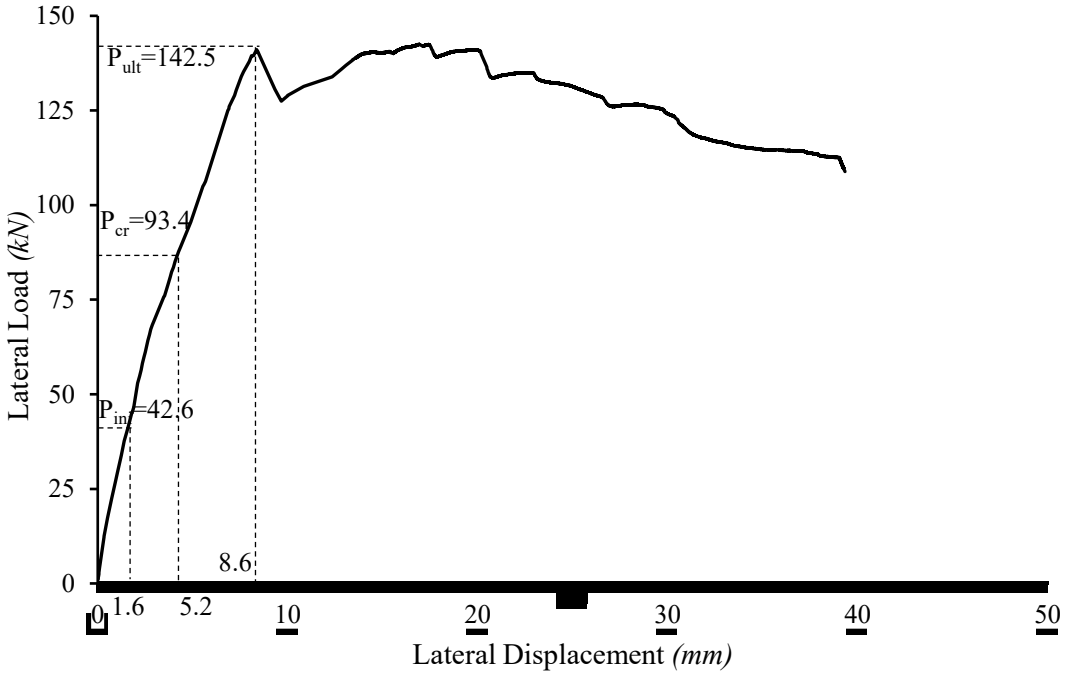

Figure 4.7. Lateral Load vs. In-Plane Displacement Curve of IF-RS

4.2.5 Specimen IF-RW

This specimen was designed with weaker CMUs and weaker mortar in comparison with the control specimen to evaluate the effect of infill masonry strength on the lateral response. Figure 4.8 shows the failure mode and Figure 4.9 shows the load vs. displacement response. In general, both the failure mode and response trend are similar to the control specimen, indicating that the infill strength may affect the ultimate load but not the behaviour. Up to a load of 28 *kN*, no cracking was observed and the response remained linear. Hairline cracks began to develop around the load of 50 *kN* in different parts of infill and the first significant diagonal crack occurred at 71.4 *kN* as shown in Figure 4.8(a). The system continued to resist load and at the load of 98 *kN*, a major crack developed and extended through a sliding crack at the second course to the loaded corner. A marked non-linearity was evident on the response curve after this point although the load continued to increase.

At failure (around 115 *kN*), the first major crack along with the sliding crack widened and faceshell spalling at the upper left corner of the infill indicated some form of corner crushing as shown in Figure 4.8(b). Similar to the control specimen, the post-ultimate behaviour is ductile and the specimen maintained about 80% of the strength over a 20 *mm* displacement.

(a)

(b)

Figure 4.8. Failure Mode for Specimen IF-RW: (a) Final Crack Pattern, (b) Faceshell Spalling at Failure

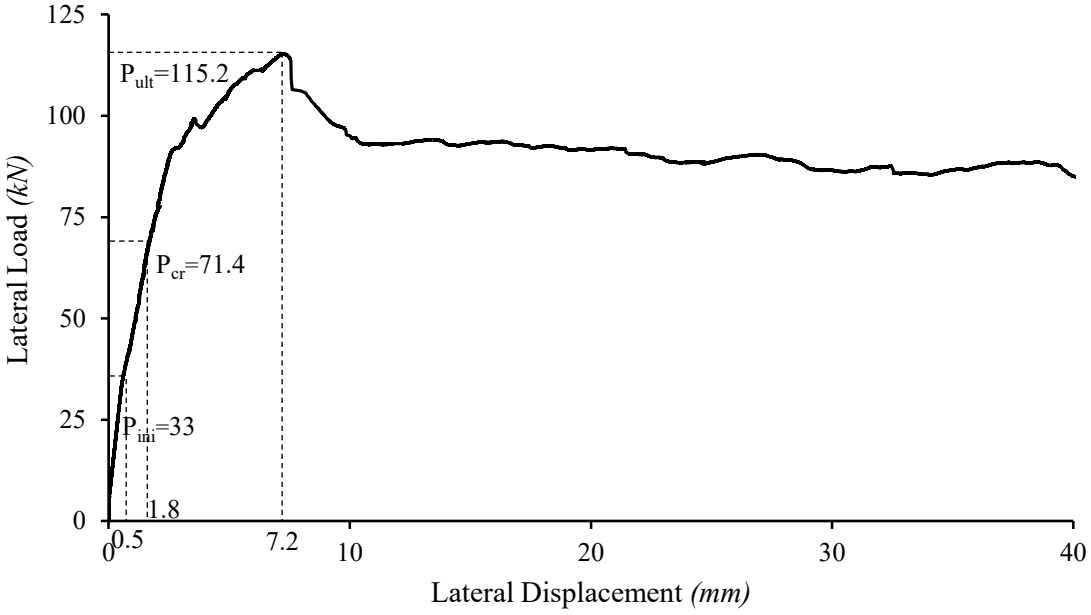

Figure 4.9. Lateral Load vs. In-Plane Displacement Curve of IF-RW

4.2.6 Specimen IF-RS-A

This specimen was used to investigate the effect of vertical load on the lateral response of all-masonry infilled frames. The vertical load of 80 *kN*, was applied first and kept constant while the lateral load was increased until the failure of the specimen. Figure 4.10 shows the failure mode and Figure 4.12 shows the load vs. displacement response. The failure development had three distinctive phases. As the lateral load increased greater than 35 *kN*, vertical hairline cracks through mortar head joints started occurring on the top beam in the vicinity of the loading points and the course underneath (Figure 4.11(a)). This is attributed to the presence of vertical load. At the lateral load of around 100 *kN*, more horizontal hairline mortar cracks formed, mostly at the left boundary column, as shown in Figure 4.11(b). At the ultimate load (199 *kN*), a sudden significant diagonal crack appeared and rapidly expanded, leading to significant cracking and face-shell spalling at the bottom of the right column (Figure 4.11(c)). The response curve showed a noticeable load drop around 124 *kN*, although no visible new cracking was observed at this load. The response curve shows stiffer behaviour in general in comparison with the control specimen, which is believed to be attributed to the vertical load presence.

Figure 4.10. Crack Pattern at Failure of IF-RS-A

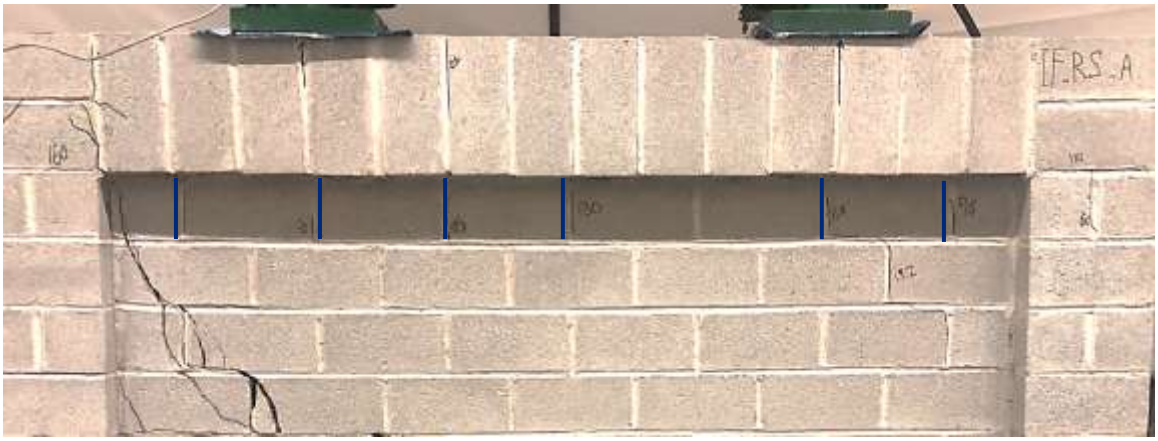

(a)

(b)

(c)

Figure 4.11. Close-Up View of Failure of IF-RS-A: (a) Vertical Hairline Cracks in the Top Course, (b) Horizontal Mortar Joint Cracks on the Left Boundary Column, (c) Compression and Shear Cracking on the Right Boundary Column

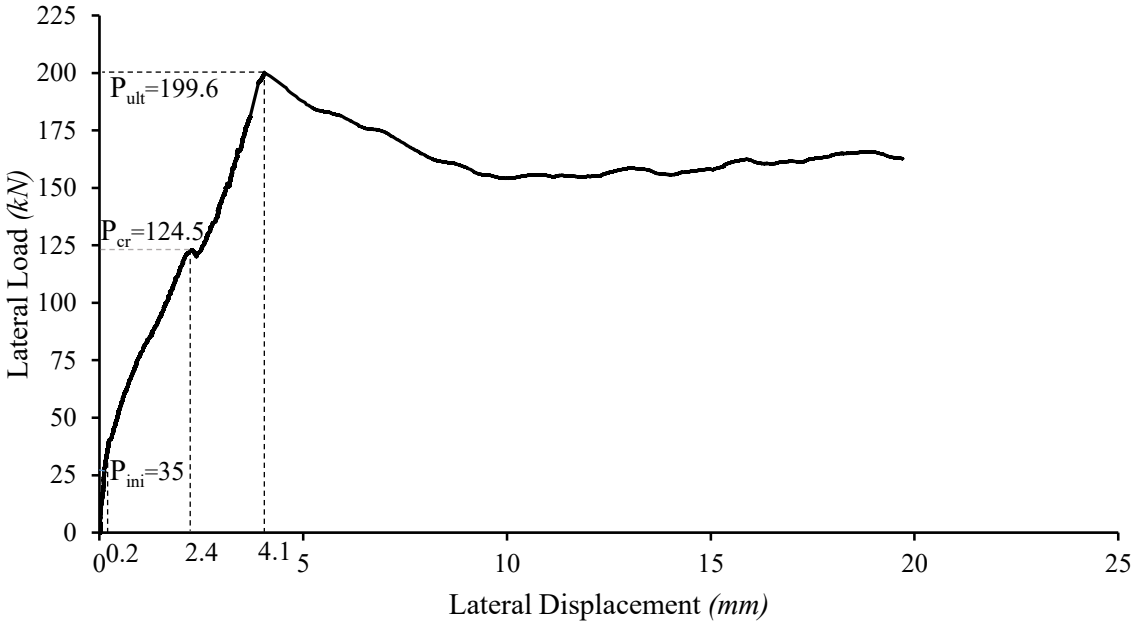

Figure 4.12. Lateral Load vs. In-Plane Displacement Curve of IF-RS-A

4.2.7 Specimen IF-BB

This specimen was constructed with two bond beams in the infill. Figure 4.13 shows the failure mode and Figure 4.14 shows the load vs. displacement response. Although there was cracking developed in a generally diagonal direction as shown, a distinctive failure characteristic that is different from the previous specimens was the long shear sliding crack through the mortar joint at the fourth course, the course above the bond beam course. This sliding shear crack suddenly appeared at the fourth course at the load of around 75 *kN*, before which point no visible cracks were observed. The marked nonlinearity between 43 to 75 *kN* on the response curve may suggest that this crack was formed earlier but just not visible. From the load of 75 *kN* to 140 *kN,* there were no new cracks observed, and the aforementioned sliding crack extended almost to the whole width of the mortar joint while the specimen deformed. Around the load of 140 *kN,* another sliding shear crack developed which caused a small load drop (Figure 4.14). Additionally, some diagonal cracks

developed from the load of 140 *kN* to 146 *kN* around the upper left and lower portion of the infill as shown as red lines in Figure 4.13. These diagonal cracks also extended into the left and right boundary columns where the vertical cracks on the right column showing the shear effect (blue lines in Figure 4.13).

Figure 4.13. Final Failure Pattern of IF-BB

The similarity between this specimen and previous ones lies in the ductility exhibited, especially the post-ultimate ductile behaviour. The noticeable difference is the much softer behaviour between the crack load and ultimate load as a result of the sliding shear.

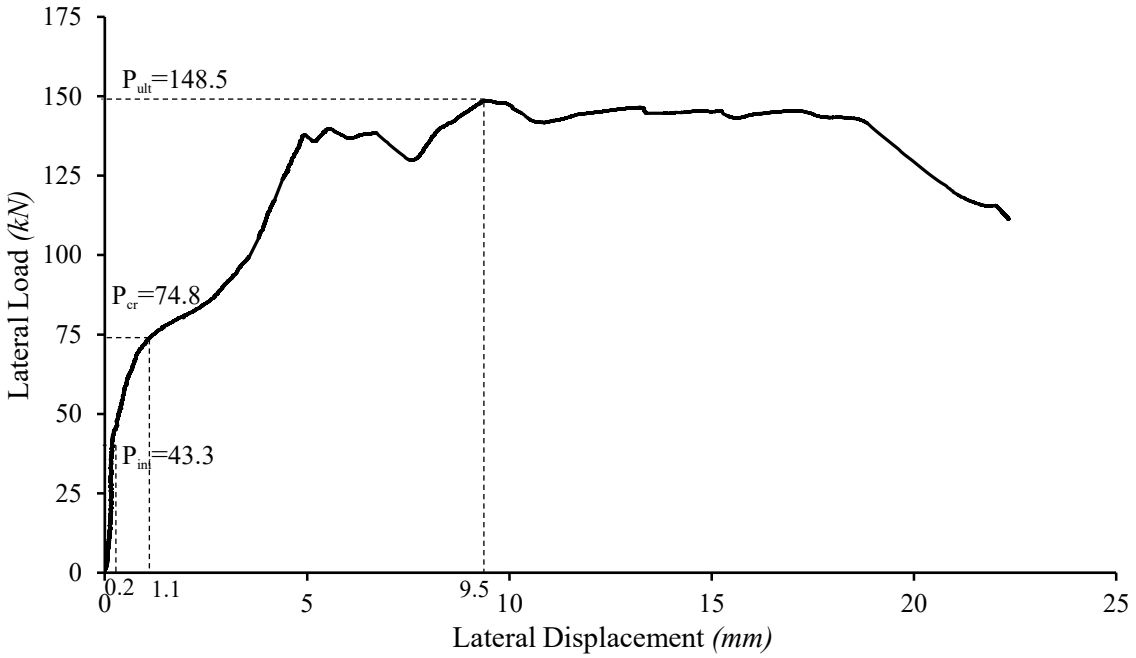

Figure 4.14. Lateral Load vs. In-Plane Displacement of IF-BB

4.2.8 Specimen IF-BJ

This specimen was designed to have the infill reinforced with ladder-type bed joint reinforcement at every other course. The blue line in Figure 4.15 shows the failure mode and Figure 4.16 shows the load vs. displacement response. The final failure pattern suggests a combination of significant shear sliding cracks and diagonal cracks. After the initial linear stage, the first visible bed joint mortar crack in the lower course of the left column occurred around the load of 60 *kN*. As load increased, more dispersed diagonal cracks developed in the mortar bed joint around 105 *kN* in the roughly same location and expended towards the corners. Around 135 *kN*, a significant shear sliding crack extending two units long occurred at the sixth course, which corresponded a 10 *kN* load drop on the response curve. The specimen continued to resist load and more hairline cracks occurred in the bed joint mortar on the left column and on the loaded corner (Figure 4.15). Before reaching the failure load of 150 *kN*, more bed joint sliding cracks developed on each course

having the bed joint reinforcement accompanied by a significant lateral displacement (green lines in Figure 4.15). At failure, the main diagonal crack widened such that almost separating the infill into two sections. Similar to previous specimens, the post-ultimate behaviour showed marked ductility and no sudden load drops were observed.

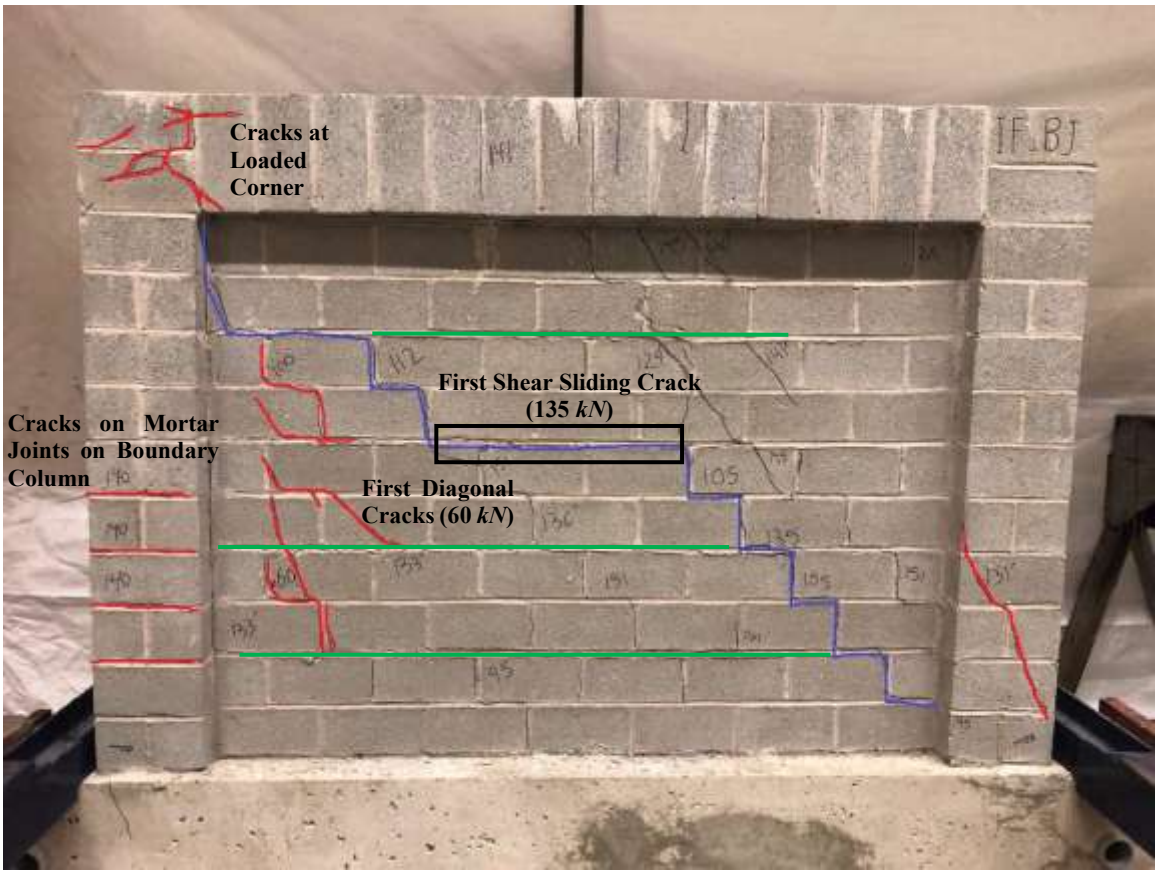

Figure 4.15. Final Failure Pattern of IF-BJ

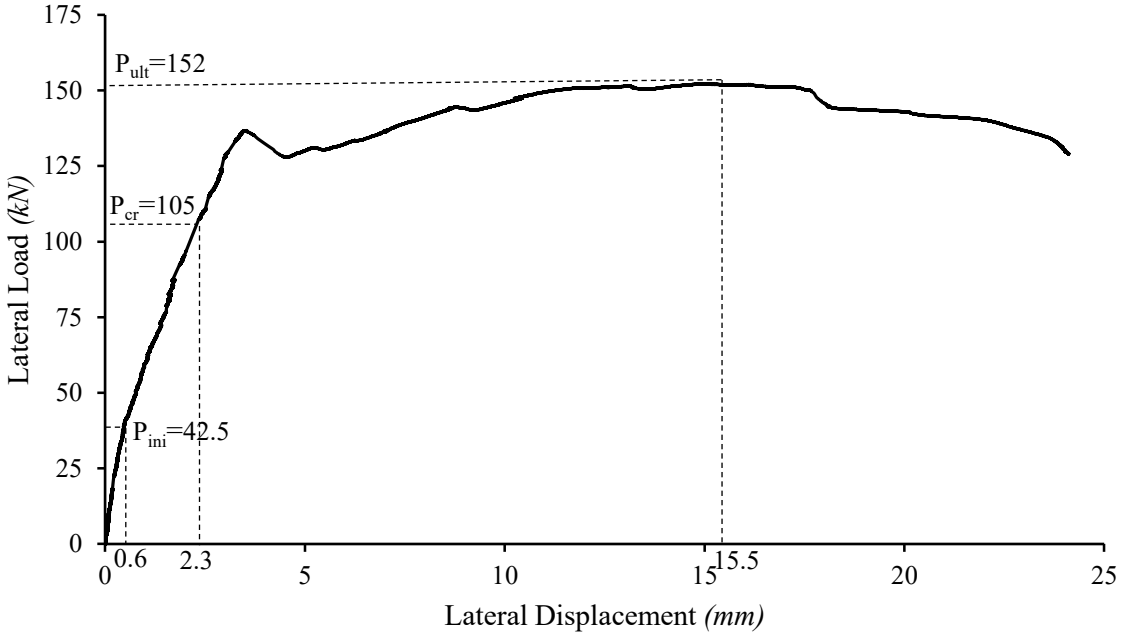

Figure 4.16. Lateral Load vs. In-Plane Displacement Curve of IF-BJ

4.3 EFFECT OF PARAMETERS ON THE IN-PLANE BEHAVIOUR

Table 4.2 provides a summary of the test results of all specimens. It shows that the presence of infills markedly increases the lateral stiffness and ultimate strength of the infilled masonry frames in comparison with the bare frame. As an example, in the case of the specimen IF-RS, the ultimate strength increased by 150% when compared to BF, whereas the initial stiffness increased more than 5 times (5.2 to 26.6 *kN/mm*). The following sections focus more on the comparison among infilled specimens.

Table 4.2. Summary of Test Results of the Specimens

Specimen ID	f'_m (MPa)	K_{ini} (kN/mm)	K_{cr} (kN/mm)	K_{ult} (kN/mm)	P_{cr} (kN)	P_{ult} (kN)	Δ_{ult} (mm)	P_{fail} (mm)	Δ_{fail} (mm)
BF	-	5.2	3.4	2.2	31.0	56.5	26.3	41.2	40.3
IF-RS	20.9	26.6	17.9	8.1	93.4	142.5	8.6	112.5	39.0
IF-RW	7.1	62.3	39.8	16.0	71.7	115.2	7.2	86.3	39.2
IF-RS-A	23.4	175.0	51.8	48.7	124.5	199.6	4.1	162.7	19.7
IF-BB	26.3	216.5	68.0	15.6	74.8	148.5	9.5	112.5	22.2
IF-BJ	20.7	71.0	45.7	9.8	105.0	152.0	15.5	130.4	24.0

4.3.1 Effect of Infill Strength

Specimens IF-RS and IF-RW were used for this study. Figure 4.17 compares load vs. displacement curves of these two specimens. The results summarized in Table 4.3 show that the specimen with the stronger infill (IF-RS) attained 24% greater ultimate load, and 30% greater cracking load when compared to the one with the weak infill (IF-RW). While both specimens showed similar ductile behaviour, IF-RS sustained larger displacement before reaching the ultimate load than IF-RW and the post-ultimate response was more gentle. On the other hand, the comparison in stiffness showed that the initial stiffness and ultimate stiffness of IF-RW were, 134% and 98% greater than IF-RS. While more specimens are needed to further the study, it can be observed that the infill strength directly affects the infilled frame strength, in both ultimate and cracking load; however, no directly proportional relationship can be determined between the infill masonry strength and the infill frame stiffness.

Table 4.3. Test Results Comparison of IF-RW and IF-RS

Specimen ID	f'_m (MPa)	K_{ini} (kN/mm)	K_{cr} (kN/mm)	K_{ult} (kN/mm)	P_{cr} (kN)	P_{ult} (kN)	Δ_{ult} (mm)
IF-RS	20.9	26.6	17.9	8.1	93.4	142.5	8.6
IF-RW	7.1	62.3	39.8	16.0	71.7	115.2	7.2

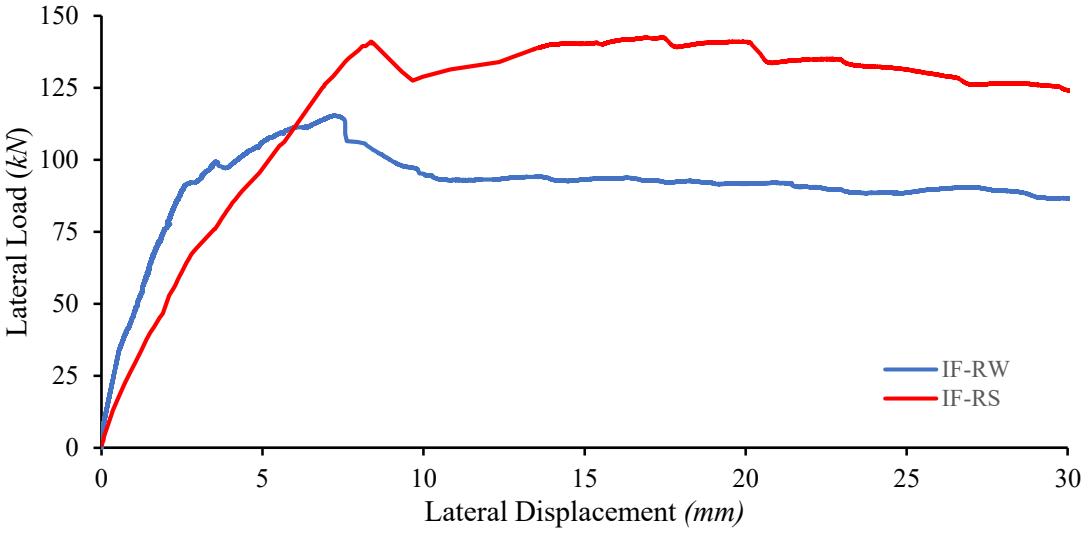

Figure 4.17. Load vs. Displacement Curves for Infill Strength Study

In the case of the cracking pattern, Figure 4.18 shows that both IF-RS and IF-RW showed two diagonal cracks in a similar manner and in the similar area of the infill before failure. At failure, in addition to the diagonal cracking, IF-RW also sustained shear sliding cracks which might be attributed to weaker mortar and thus weaker bond between the mortar and the block. The frame of IF-RS suffered more cracking than IF-RW, indicating for a weaker masonry infill strength, the cracking occurs more in the infill.

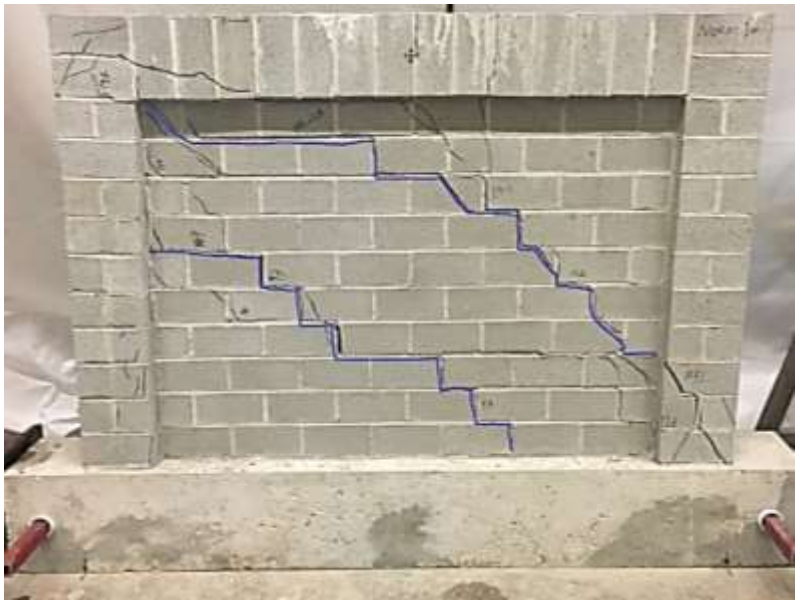

(a)

(b)

Figure 4.18. Comparison of Final Crack Pattern: (a) IF-RS, (b) IF-RW

4.3.2 Effect of Vertical Load

The effect of vertical load is illustrated in Table 4.4 and Figure 4.19 where the load vs. displacement response of specimens IF-RS and IF-RS-A are compared. The presence of vertical load (80 *kN* in this case) resulted in significant increases in both cracking and

ultimate load of IF-RS-A, by about 33% and 40%, respectively, when compared to those of IF-RS. In the case of stiffness, as expected, the presence of vertical load resulted in a much stiffer infilled frame system with lower ductility than the control specimen. IF-RS-A showed more than five times in both initial and ultimate stiffnesses than IF-RS, but reached the ultimate load at a smaller displacement (4.1 *mm* vs. 8.6 *mm*). The post-ultimate behaviour of IF-RS-A showed a more brittle failure with a significant load drop.

Table 4.4. Test Result Comparison of IF-RS-A and IF-RS

Specimen ID	f'_m (MPa)	K_{ini} (kN/mm)	K_{cr} (kN/mm)	K_{ult} (kN/mm)	P_{cr} (kN)	P_{ult} (kN)	Δ_{ult} (mm)
IF-RS	20.9	26.6	17.9	8.1	93.4	142.5	8.6
IF-RS-A	23.4	175.0	51.8	48.7	124.5	199.6	4.1

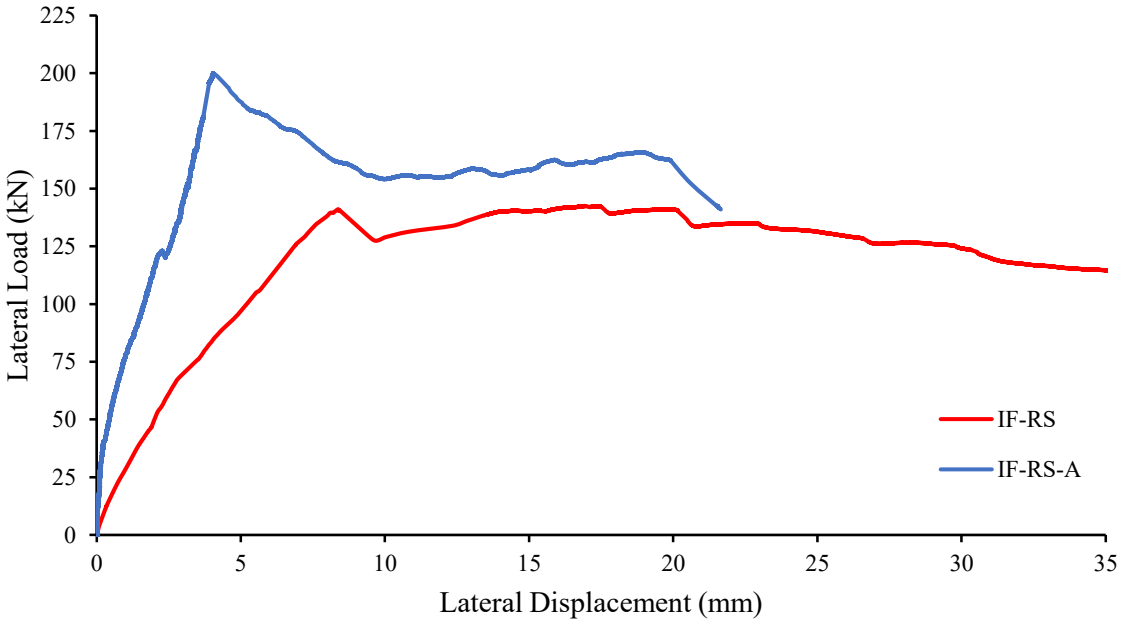

Figure 4.19. Load vs. Displacement Curves for Vertical Load Study

Figure 4.20 provides a side-by-side failure pattern comparison for IF-RS and IF-RS-A. It shows that the characteristics of failure mode between the two specimens are similar, all sustaining severe diagonal cracking and boundary column cracking, albeit that IF-RS's diagonal cracking was more extensive. This is attributed to a more ductile behaviour of IF-RS where cracking was allowed to develop over a larger displacement. The difference is that the vertical load resulted in some vertical cracks in the course underneath the frame beam, although this cracking did not seem to directly link to the diagonal cracking. Higher levels of vertical load should be included in a further study to evaluate its impact on the failure mode.

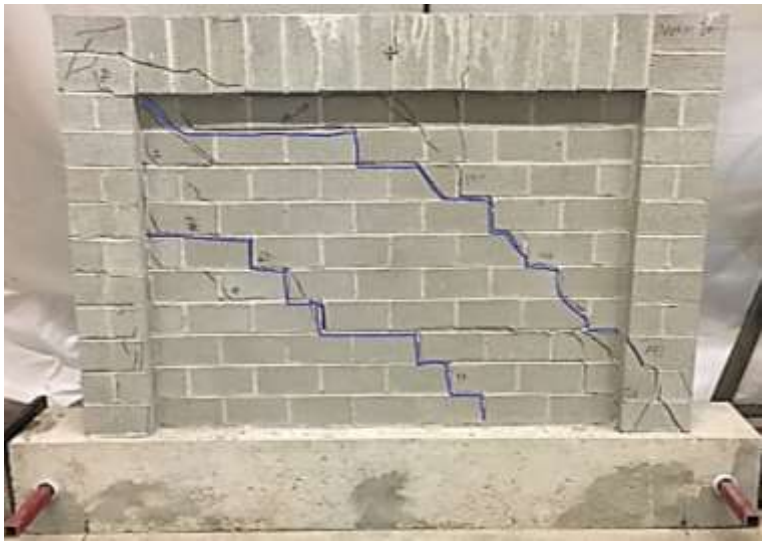

(a)

(b)

Figure 4.20. Crack Pattern Comparison: (a) IF-RS, (b) IF-RS-A

4.3.3 Effect of Infill Reinforcement

The effect of infill reinforcement is illustrated in Table 4.5 and Figure 4.21 where specimens IF-RS, IF-BB, and IF-BJ are compared. In terms of strength, while the infills with reinforcement attained higher ultimate loads, the degree of the capacity increase was small, about 5%, which may be insignificant from a practical standpoint. The more pronounced effect is observed in the stiffness. Both the initial and cracking stiffness of IF-

BJ and IF-BB were noticeably higher than IF-RS. Further, the former two specimens showed a greater capability of sustaining displacement, especially IF-BJ, before reaching the ultimate load than the latter specimen. A comparison between IF-BB and IF-BJ seems to suggest that a more distributed reinforcement scheme (IF-BJ) performed better than a concentrated one (IF-BB) where the load and overall ductility were slightly higher for the former.

Table 4.5. Test Results Comparison of IF-RS, IF-BB and IF-BJ

Specimen ID	f'_m (MPa)	K_{ini} (kN/mm)	K_{cr} (kN/mm)	K_{ult} (kN/mm)	P_{cr} (kN)	P_{ult} (kN)	Δ_{ult} (mm)
IF-RS	20.9	26.6	17.9	8.1	93.4	142.5	8.6
IF-BB	26.3	216.5	68.0	15.6	74.8	148.5	9.5
IF-BJ	20.7	71.0	45.7	9.8	105.0	152.0	15.5

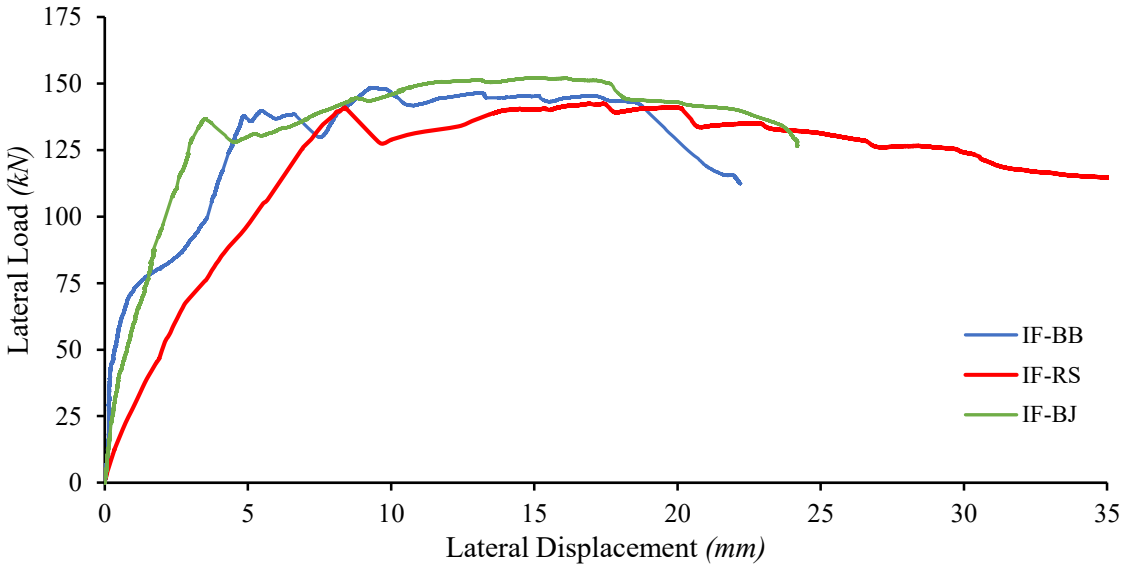

Figure 4.21. Lateral Load vs. Displacement Curves for Infill Reinforcement Study

A side-by-side failure pattern comparison for the three specimens is shown in Figure 4.22. Again, one distinctive characteristic of the specimen with infill reinforcement is the pronounced shear sliding crack which resulted in the final failure. Horizontal reinforcement is often used in masonry shear walls to increase the shear resistance of the wall. It is thus interesting to observe that the horizontal reinforcement in the infilled frame application did not markedly increase the capacity of the infill, indicating a different failure mechanism between the infill and the shear wall even though both are lateral load resisting elements.

(a)

(b)

(c)

Figure 4.22. Failure Crack Pattern Comparison: (a) IF-RS, (b) IF-BJ, (c) IF-BB

4.4 STORY DRIFT

The previous discussion compared the absolute ultimate load of each specimen. However, the comparison can only be complete if the performance of specimens is also compared at code-permitted drift levels. According to National Building Code of Canada (NBCC 2015), the allowable storey drifts are 1%, 2%, and 2.5% of the storey height for post-disaster buildings, schools, and all other buildings, respectively. For the height of the frames (1215 *mm*) tested in this study, the three allowable storey drifts were calculated to be 12.2, 24.3, and 30.4 *mm* respectively. Table 4.6 summarizes the load comparison at these three drift levels and they are labeled as P_{d1}, $P_{d2,}$ and P_{d3}, respectively. Figure 4.23 plots load vs. displacement curves of all infilled specimens with drift levels identified.

Table 4.6. Summary of the Loads Sustained at Three Allowable Storey Drifts

Specimen ID	P_{ult} (kN)	P_{d1} (kN)	P_{d2} (kN)	P_{d3} (kN)
IF-RS	142.5	132.9	132.1	123.0
IF-RW	115.2	93.1	88.6	86.3
IF-RS-A	199.6	155.2	-	-
IF-BB	148.5	145.1	-	-
IF-BJ	152.0	145.1	-	-

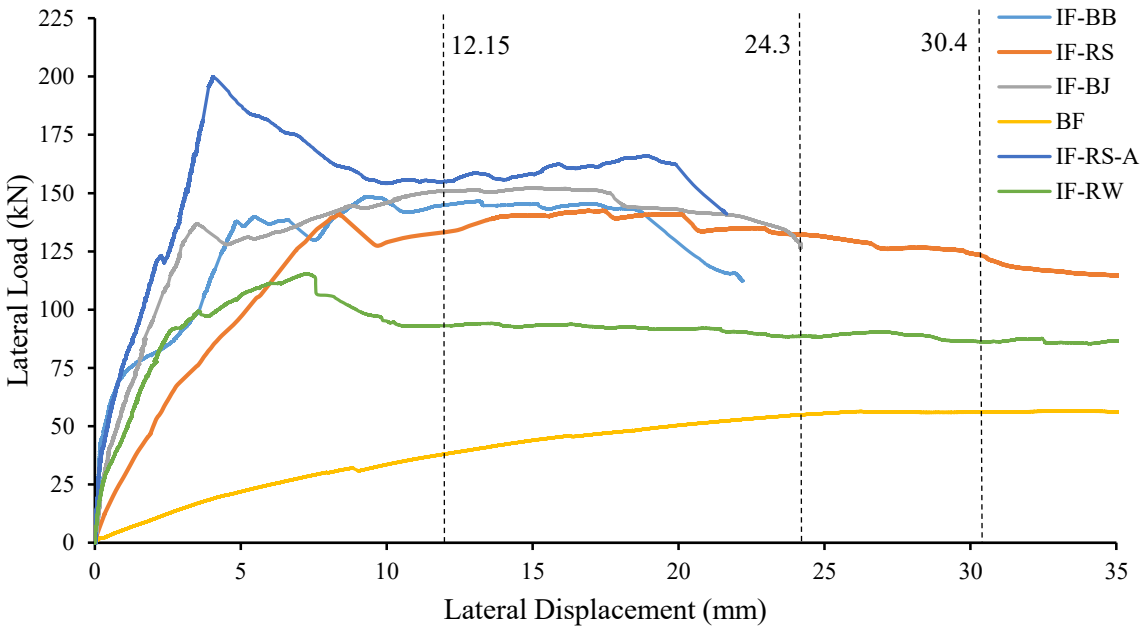

Figure 4.23. Comparison of Load vs. Displacement Curves for Drift Study

Note that no data was collected at 2% and 2.5% for IF-RS-A, IF-BB and IF-BJ, indicating the test was stopped before reaching this level of displacement. Considering that all ultimate loads for all specimens were obtained within 1% of the drift level, this indicates that this system satisfies all three categories of building drift limits and thus can be used for all from the drift standpoint. The following comparison is performed for 1% drift level. Both the table and figure show that all the previous discussed observations remain valid and true at 1% drift level. It is noted that If-BB and IF-BJ reached their ultimate loads around 1% drift levels whereas others did so significantly before this point. These further underscores the point that the infill reinforcement increased the ductility of the infilled frame system.

4.5 DUCTILITY

Ductility is used to measure how much a structure or a member can tolerate deformation after the yield point, while maintaining most of its load-carrying capacity. Ductility is often calculated as the ratio between the measured displacement at a specific load demand level and the maximum elastic displacement. Ductility of masonry structures depends on a wide range of factors, including axial load ratio, reinforcement ratio, and structural geometry. When subjected to seismic load, the ductility factor plays an important role in design structures' ability to absorb energy through plastic deformation. Thus, structures can be designed at a reduced seismic load once they satisfied the ductility demand. NBCC 2015 permits to reduce the seismic design load by a factor of 1 to 5 based on the seismic resisting system used. According to NBCC 2015, typical ductility factors for moment-resisting RC frames and unreinforced masonry are 2.5 and 1.0, respectively. However, there is no specified ductility factors listed for unreinforced masonry infilled masonry frames as a seismic resisting frame. While the ductility factor is often evaluated using the backbone curves generated through hysteretic responses of a structure under cyclic loading, it is felt still useful to evaluate it with the available results herein. A previous study (Steeves 2017) showed that the backbone curve of a hysteresis response is similar to a static curve in general with the difference of having a reduced ultimate load. Assuming that the load vs. displacement curves under static loading is similar to the curve under cyclic loading, the ductility factor may be calculated through an adopted approach by several researchers (Salonikios et al., 2000; Carrillo et al., 2014; Tawfik et al., 2014; Robazzza 2019). According to this approach, ductility is the ratio of the displacement corresponding 20% to 50% drop after the ultimate load (Δ_d) to the displacement at 80% of the ultimate load (P_y)

in the rising part of the curve (Δ_y) as illustrated in Figure 4.24 and Equation 4.1. In this study, a 20% reduction in load after reaching P_{ult}, was chosen to determine Δ_d. Table 4.7 provides a summary of the ductility factor of each specimen.

$$R_d = \frac{\Delta_d}{\Delta_y} \quad [4\text{-}1]$$

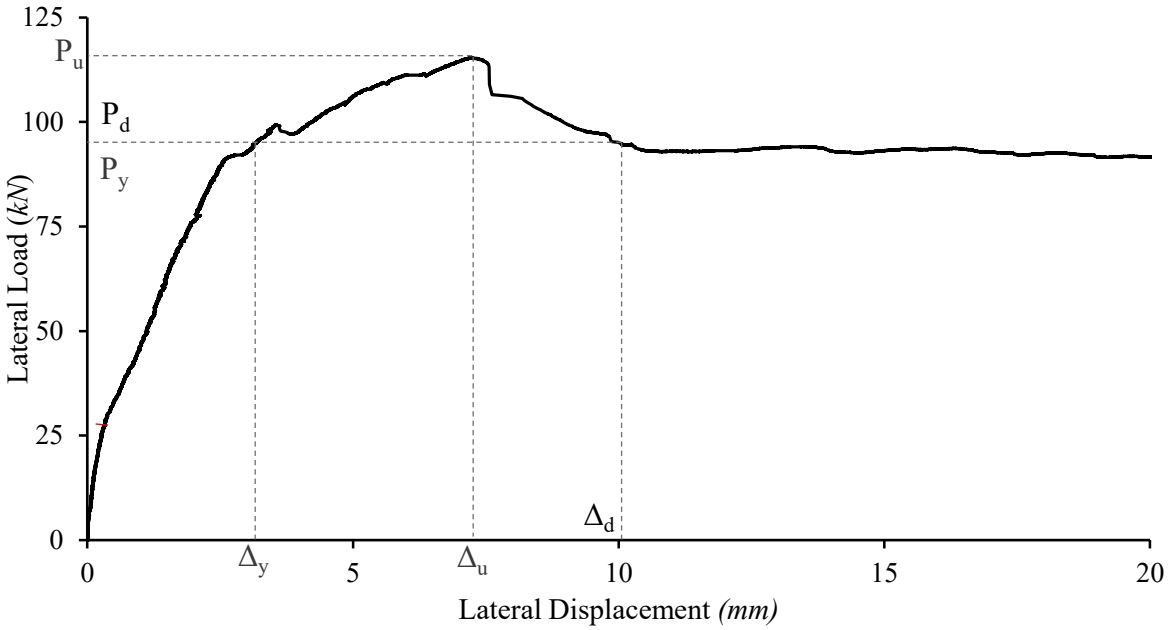

Figure 4.24. Δ_d and Δ_y Definition in Ductility Calculation

Table 4.7. Summary of Ductility Factor of Specimens

Specimen ID	$P_d = P_y$ (kN)	Δ_d (mm)	Δ_y (mm)	R_d
BF	45.2	38.3	15.8	2.4
IF-RS	114.0	37.3	6.2	6.0
IF-RW	92.2	18.7	2.9	6.2
IF-RS-A	160.0	8.5	3.3	2.6
IF-BB	118.8	21.0	4.2	5.0
IF-BJ	122.5	24.1	2.9	8.3

According to the table, the average ductility factor for masonry infilled masonry frame specimens is approximately 6.4 which is greater than unity, as specified for unreinforced masonry by NBCC 2015. This indicates that unreinforced masonry infills bounded by reinforced masonry frames have much improved ductility and have the potential to be used as a seismic resisting system. Additionally, the moderately ductile concrete moment resisting frames have a ductility factor of 2 as specified by NBCC 2015. The ductility factor of 2.4 achieved by the bare frame specimen showed that the reinforced masonry frame is comparable to RC bare frames in terms of ductility. As expected, the specimen with vertical load showed less ductility. It should be pointed out that a more accurate evaluation of ductility should be performed based on cyclic loading results. However, the above discussion serves to shed some light on the capability of all-masonry infilled frame systems as a seismic resisting system.

4.6 RESULT OF AUXILIARY TESTS

4.6.1 CMUs

Four batches of CMUs were used to construct the infilled specimens. Three CMUs were randomly selected from each batch for the determination of physical properties and compressive strength of the CMUs. The physical properties included the net and gross area, density, 24-hour absorption rate, and moisture content of CMUs and they were determined using procedures specified in ASTM C140/C140M (2018). The received weight of each CMU block was first measured. The block was then immersed in the water and the immersed weight was subsequently measured. Next, the block was kept in the water for 24 hours to measure the saturated weight after being surface dried with a towel. Then the block was kept in an oven at $100°C$ for 24 hours and the dry weight was measured

afterwards. According to the provisions required by CAN/CSA A165 (2015) Standard for Masonry Units, a standard 200 *mm* hollow block, shall have a density greater than 2000 kg/m^3, a moisture content less than 45%, and an absorption less than 175 kg/m^3. Moreover, the CV of sample results shall be less than 15%. Table 4.8, 4.9, 4.10, and 4.11 summarize the properties measured for the four batches of concrete blocks. Although all blocks are in half-scale, they satisfied the property requirements given by the code for a standard 200 *mm* block. However, the density of new batch blocks was less than 2000 kg/m^3, strength-wise, it had no effect on the results.

Table 4.8. Standard Stretcher CMUs Properties

ID	Received Weight (w_r)	Immersed Weight (w_L)	Saturated Weight (w_s)	Dry Weight (w_D)	Absorption		Moisture Content	Density
	g	g	g	g	kg/m^3	%	%	kg/m^3
S1	1687.5	779	1788.6	1674.2	113.3	6.8	11.6	1658.3
S2	1685.5	760	1771.3	1669.8	100.4	6.1	15.5	1651.1
S3	1683.8	768	1772.4	1670.3	101.6	6.1	13.5	1663.3
				Avg.	105.1	6.3	13.5	1657.6
				CV(%)	6.8	6.7	14.2	0.4

Table 4.9. Half Blocks Properties

ID	Received Weight (w_r)	Immersed Weight (w_L)	Saturated Weight (w_s)	Dry Weight (w_D)	Absorption		Moisture Content	Density
	g	g	g	G	kg/m^3	%	%	kg/m^3
H1	991	433	1029.1	980.2	82.4	5.0	22.4	1644.0
H2	1017	444	1054.1	1005.8	79.2	4.8	23.2	1648.6
H3	998	438	1045.0	986.5	96.4	5.9	19.7	1625.2
				Avg.	86.0	5.2	21.7	1639.3
				CV(%)	10.6	11.4	8.5	0.8

Table 4.10. Boundary CMUs Properties

ID	Received Weight (w_r)	Immersed Weight (w_L)	Saturated Weight (w_s)	Dry Weight (w_D)	Absorption		Moisture Content	Density
	g	g	g	G	kg/m^3	%	%	kg/m^3
L1	5176	2313.3	5406	5105	97.3	5.9	23.6	1650.7
L2	5164	2322.4	5399	5083	102.7	6.2	25.6	1652.1
L3	5170	2349.6	5440	5104	108.7	6.6	19.6	1651.6
				Avg.	102.9	6.2	23.0	1651.5
				CV(%)	5.5	5.5	13.3	0.1

Table 4.11. Weak Stretcher CMUs (for IF-RW) Properties

ID	Received Weight (w_r)	Immersed Weight (w_L)	Saturated Weight (w_s)	Dry Weight (w_D)	Absorption		Moisture Content	Density
	g	g	g	G	kg/m^3	%	%	kg/m^3
O1	1625.3	931.5	1732.2	1616.7	144.2	7.1	7.8	2019.1
O2	1630.4	941.3	1737.6	1619.1	148.8	7.3	9.5	2033.3
O3	1620.0	925.3	1725.4	1608.0	146.7	7.3	10.2	2009.7
				Avg.	146.6	7.3	9.2	2020.7
				CV(%)	1.6	1.3	13.6	0.6

The net area of 8390 *mm^2*, 6290 *mm^2*, and 27,840 *mm^2* were used to calculate the compressive strength of the standard stretcher CMUs, weak stretcher CMUs and boundary blocks, respectively. Table 4.12 presents the compressive strength of CMUs and Figure 4.25 shows typical failure modes of stretcher and boundary CMUs.

Table 4.12. Mechanical Properties of CMUs

Block Type	ID	Net Area (mm^2)	Compressive Capacity		Avg. (MPa)	CV(%)
			Load (kN)	Strength (MPa)		
New Stretcher CMUs	S1	8390	147.2	17.5	18.9	9.5
	S2	8391	175.5	20.9		
	S3	8392	152.8	18.2		
Weak Stretcher CMUs	W1	6290	64.6	10.3	10.3	14.6
	W2	6290	55.2	8.8		
	W3	6290	74.5	11.8		
Boundary CMUs	L1	27840	405.0	14.5	15.7	8.0
	L2	27840	475.0	17.1		
	L3	27840	434.0	15.6		

(a)

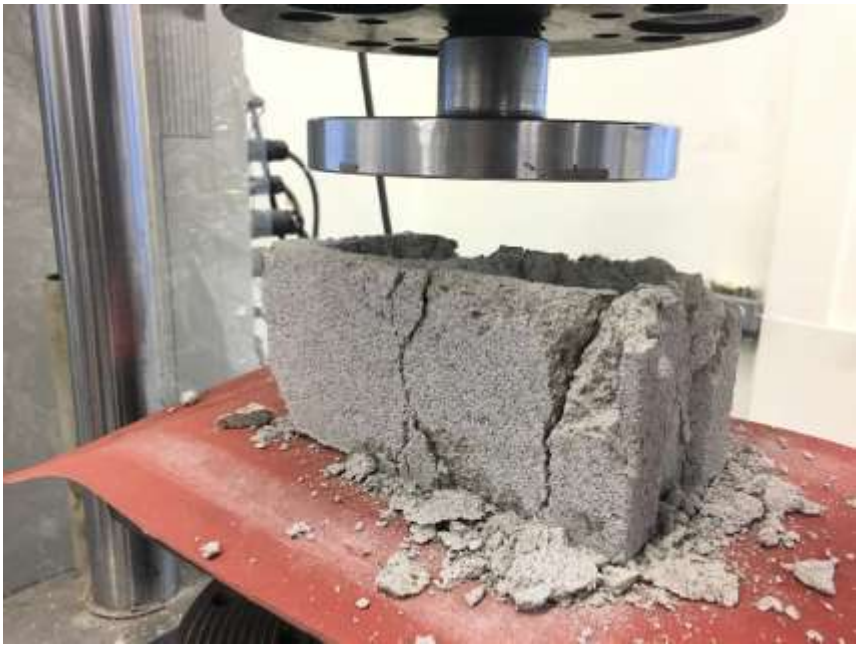

(b)

Figure 4.25. Typical Failure Mode of CMUs

4.6.2 Mortar

A total of 16 batches of standard mortar and 4 batches for weak mortar were used in constructing specimens. Table 4.6 summarizes the compressive strength for each mortar batch and its corresponding specimen. A typical failure mode of mortar cubes is shown in Figure 4.26.

Figure 4.26. Typical Failure Mode for Mortar Samples

Table 4.13. Mortar Sample Strength

Spec. ID	Mortar Batches ID	Compressive Strength (MPa)	Avg. (MPa)	CV(%)
IF-RS	B5	13.3	18.9	21.3
	B6	22.0		
	B7	21.6		
	B8	18.6		
IF-RS-A	B10	12.5	13.8	10.3
	B11	13.1		
	B12	14.0		
	B13	15.8		
IF-RW	W1	12.5	10.6	13.9
	W2	9.4		
	W3	10.8		
	W4	9.5		
IF-BJ	B1	15.4	17.5	8.3
	B2	18.8		
	B3	18.0		
	B4	17.9		
IF-BB	B14	15.6	14.7	6.3
	B15	13.8		
	B16	14.8		
BF	B9	13.1	14.5	12.9
	B13	15.8		

4.6.3 Grout

A total of 11 grout batches were used for constructing specimens. The overall mean of grout compressive strength was determined to be 20 MPa with a CV of 4.6%. Table 4.14 presents the grout strength for each specimen and overall grout strength, and Figure 4.27 shows the failure pattern of grout prisms.

Table 4.14. Average Grout Compressive Strength for Specimens

Spec. ID	Grout Batch Numbers	Grout Batch Strength (MPa)	CV(%)	Avg. (MPa)
IF-RS	B2	20.7	19.5	20.4
	B6	20.2	10.6	
IF-RS-A	B4	20.1	18.8	20.4
	B5	20.7	10.7	
IF-RW	B3	17.2	9.8	18.7
	B4	20.1	18.8	
BF	B6	20.2	10.6	19.1
	B7	19.1	8.2	
	B8	18.1	3.9	
IF-BB	B1	20.1	13.7	21.2
	B3	17.2	9.8	
	B9	23.0	13.9	
	B10	19.4	10.3	
IF-BJ	B10	19.4	10.3	19.9
	B11	20.4	5.3	
			Avg.	20.0
			CV(%)	4.6

Figure 4.27. Grout Sample Failure mode

4.6.4 Masonry Prism

A total of 15 masonry prisms were constructed. The compressive strength of masonry prisms is summarized in Table 4.15 and the mean compressive strength corresponded to each specimen is also presented. Masonry prisms were identified using the same labels as the mortar used to construct them. As shown in the table, the CV of specimens IF-RS-A was not below the required limit of CV which is 15% according to CSA S304-14. The dominant failure pattern were vertical inclined cracks through both face shells and webs of the prisms which is illustrated in Figure 4.28.

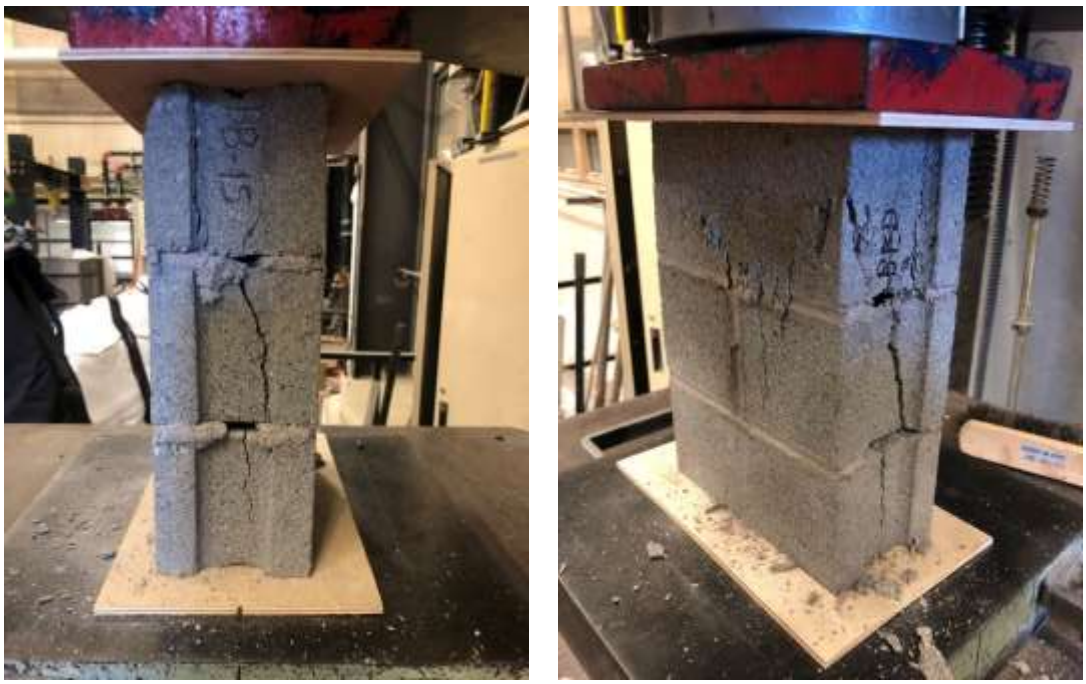

(a) (b)

Figure 4.28. Failure Mode of Masonry Prisms

Table 4.15. Compressive Strength of Masonry Prisms

Spec. ID	Mortar Batch	Ultimate Load (kN)	f'_m (MPa)	Avg. (MPa)	CV(%)
IF-RS	B13	21.9	21.9	20.9	6.2
	B11	19.5	19.5		
	B10	21.4	21.4		
Weak	W1	7.6	7.6	7.1	6.3
	W2	7.1	7.1		
	W4	6.7	6.7		
IF-RS-A	B7	24.5	24.5	23.4	7.4
	B5	21.4	21.4		
	B8	24.3	24.3		
IF-BB	B14 (BB)	25.5	25.5	26.3	4.0
	B15	26.0	26.0		
	B16	27.5	27.5		
IF-BJ	B3	20.8	20.8	20.7	4.1
	B4	19.8	19.8		
	B2	21.5	21.5		

4.6.5 Concrete Cylinder

Only one batch was used for the base beams concrete casting. Four small (S) and two large cylinders (L) were sampled from the batch. The concrete cylinders were tested to measure the concrete compressive strength at 14-day, 28-day, and the day of specimen testing, and

modulus of elasticity at the day of specimen testing. Table 4.16 lists a summary of concrete cylinder compression test results. Figure 4.29 shows the failure pattern of concrete cylinders which was conical failure with vertical inclined cracks. Figure 4.30 illustrates the linear portion of the stress-strain curve where the elastic modulus of the concrete was determined.

Table 4.16. Concrete Cylinder Compression Test Results

	Ultimate Load (kN)	Compressive Strength (MPa)	Modulus of Elasticity (MPa)	Avg. (MPa)	CV(%)
14 days					
S 1	192.8	24.6	-	24.3	1.6
S 2	188.5	24.0			
28 days					
S 3	215.5	27.4	-	27.8	1.9
S 4	221.4	28.2			
Day of specimen testing					
L 1	538.4	30.5	-	30.7	0.8
L 2	547.1	31.0			
L 3	541.1	30.6			
Modulus of Elasticity (MPa)					
L 1	-		23167		
L 2	-		25430	24537	4.9
L 3	-		25016		

Figure 4.29. Concrete Cylinders Failure Pattern

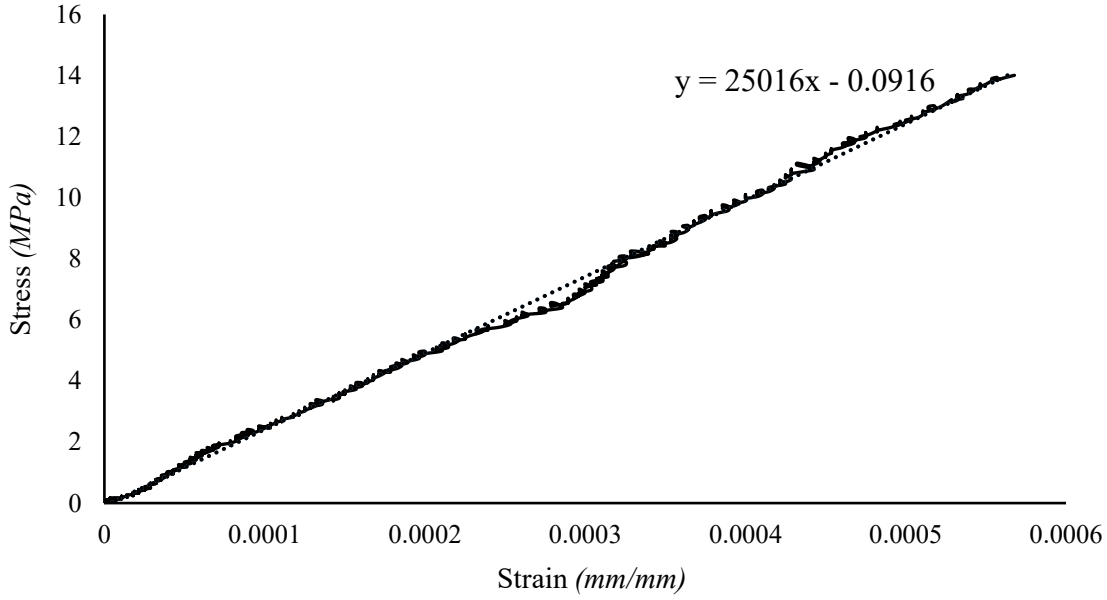

Figure 4.30 Initial Stress vs. Strain Curve of Concrete Cylinders under Compression

4.6.6 Summary of Auxiliary Test Results

As mentioned in Chapter 3, the mechanical properties of vertical steel reinforcement were collected from Hu (2015), and those for the bed joint reinforcement were consulted with ASTM A951 (2016) for specified strength. A summary of auxiliary test results for each masonry infilled frame specimen is provided in Table 4.17.

Table 4.17. Summary of Auxiliary Test Results

Component	Property	BF	IF-RS	IF-RS-A	IF-RW	IF-BB	IF-BJ
Boundary CMUs	Strength (MPa)	15.7	15.7	15.7	15.7	15.7	15.7
Infill CMUs	Strength (MPa)	-	18.9	18.9	10.3	18.9	18.9
Mortar	Strength (MPa)	14.5	18.9	13.9	10.6	14.7	17.5
Grout	Strength (MPa)	19.3	20.4	20.4	18.7	20.2	19.9
Masonry Prism	Strength (MPa)	-	20.9	23.4	7.1	26.3	20.7
Concrete	Strength (MPa)	30.7	30.7	30.7	30.7	30.7	30.7
	Elastic Modulus (MPa)	24537	24537	24537	24537	24537	24537
Reinforcement (Hu 2015)	Yield (Tensile) Strength (MPa)	446 (665)	446 (665)	446 (665)	446 (665)	446 (665)	446 (665)
Bed-Joint Reinforcement (ASTM A951 2016)	Yield (Tensile) Strength (MPa)	-	-	-	-	-	485 (550)

CHAPTER 5 COMPARATIVE STUDY OF EXPERIMENTAL RESULTS AND EVALUATION OF ANALYTICAL METHODS

5.1 INTRODUCTION

In this chapter, the experimental results of the current study are compared with the previous experimental studies conducted by the same research group (Hu 2015; Manesh 2013). Additionally, the applicability of analytical methods specified in the North American design standards for calculation of infill in-plane stiffness and strength on all-masonry infilled frames is evaluated.

5.2 COMPARISON WITH THE PREVIOUS STUDIES BY THE RESEARCH GROUP

Two previous experimental studies were used in this comparative study. One was conducted by Hu (2015) on concrete masonry infilled RC frames under monotonic lateral loading. The other one was conducted by Manesh (2013) on concrete masonry infilled steel frames with vertical load presence. As mentioned previously, the geometry of the infill and frame, reinforcement ratio and main material properties were kept consistent between this and Hu's study to enable a direct comparison. In the case of Manesh (2013)'s study, the comparison was conducted on the effect of vertical load presence. Although the infill geometry was the same, due to the difference in bounding frame (steel vs. concrete), the comparison was relative.

5.2.1 Comparison with Experimental Results of Hu (2015)

In this case, two sets of specimens were compared including: 1) masonry and RC bare frames and 2) concrete masonry infills bounded by either RC frame or masonry frame. Table 5.1 summarizes the test results. Figures 5.1 and 5.2 compare the load vs.

displacement curves of bare frames and infilled frame specimens, respectively. The comparison of bare frame specimens shows that two specimens attained almost the same ultimate load and the general behavioral trend was also similar. Marked ductility was noted in both cases. It appears that the RC frame had higher initial stiffness (20.2 vs. 5.2 kN/mm) which might be attributed to the fact that RC member is a monolithic whole while masonry members are assemblages of masonry unit, mortar and grout which results in an inherently "non-tight" system. The "slack" between components shows a softer system. However, the stiffness of two specimens at ultimate was in the same order, indicating that after extensive cracking, two frames behaved similarly.

Table 5.1. Summary of Experiment Results of Current and Hu (2015)'s Study

	Specimen ID	f'_m (MPa)	K_{ini} (kN/mm)	K_{cra} (kN/mm)	K_{ult} (kN/mm)	P_{cra} (kN)	P_{ult} (kN)	Final Failure Mode
Current Study	Bare Masonry Frame	-	5.2	-	2.2	-	56.5	-
	IF-RS	18.9	26.6	17.9	8.1	93.4	142.5	DC
Hu (2015)	Bare RC Frame	-	20.2	-	1.7	-	57.7	-
	IF-NG	16.7	39.9	18.2	12.2	101.9	133.6	CC

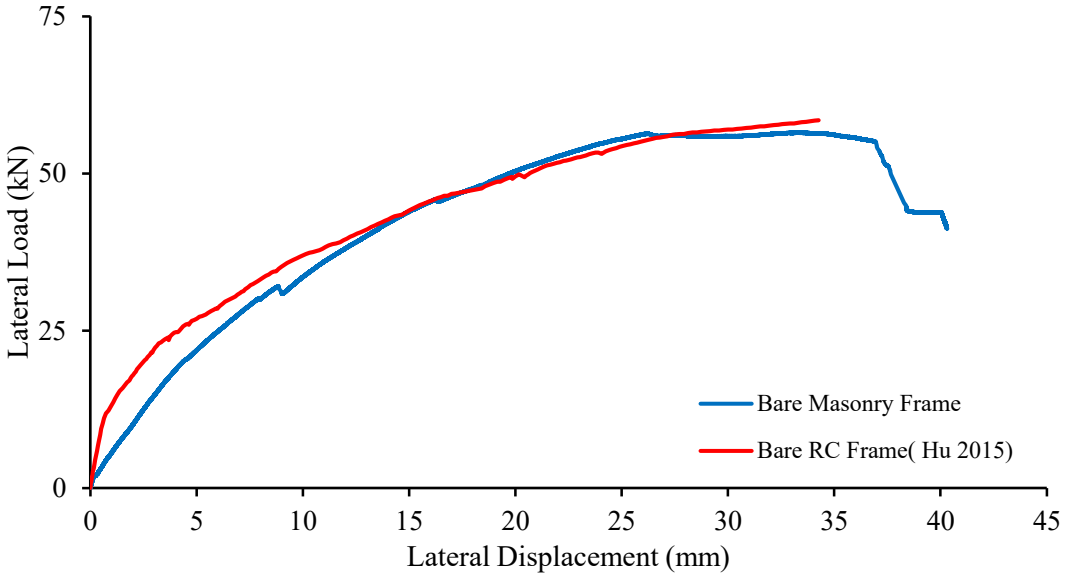

Figure 5.1. Comparison of Load-Displacement Curves for RC Bare Frame and Masonry Bare Frame Specimens

In the case of infilled frames, two specimens had similar ultimate loads with all-masonry infilled specimen (IF-RS) having slightly (6%) higher capacity than infilled RC specimen (IF-NG). The initial and crack stiffness of both specimens are more or less in the same range. The most distinctive difference appears in the post-ultimate behaviour. All-masonry infilled frame showed more ability to maintain the capacity over a large displacement while the RC framed specimen had a pronounced load drop immediately after the ultimate load. In other words, the all-masonry infilled frame seems to display greater ductility and potential more energy dissipation ability. A side-by-side failure mode comparison as seen in Figure 5.3 showed that IF-RS failed due to two-branch diagonal cracking mode, with cracking extending into columns while IF-NG experienced diagonal cracks as initiation of failure prior to corner crushing as final failure mode.

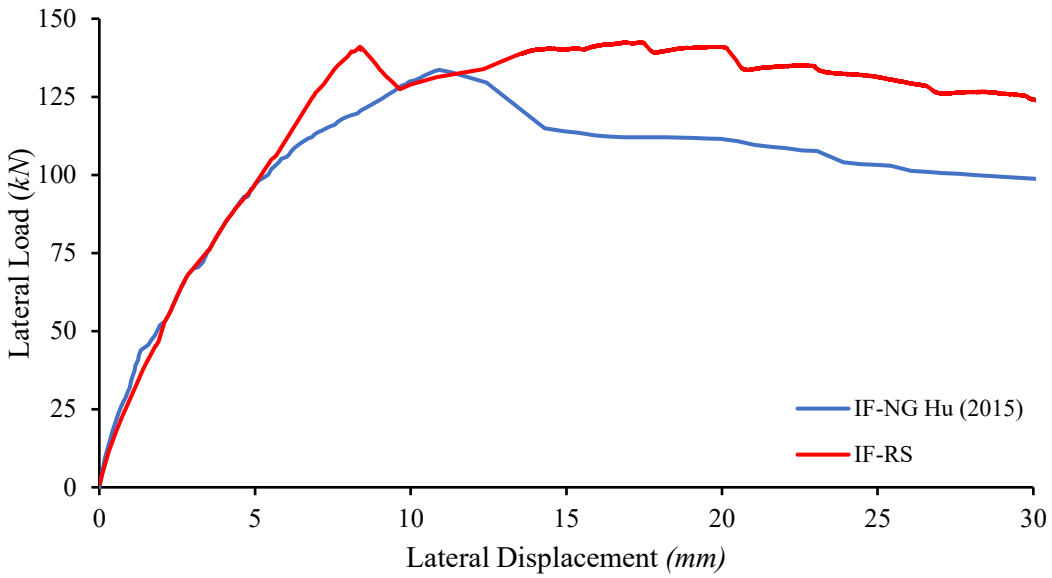

Figure 5.2. Comparison of Load-Displacement Curves for Infilled RC Frame and Masonry Frame Specimens

(a)

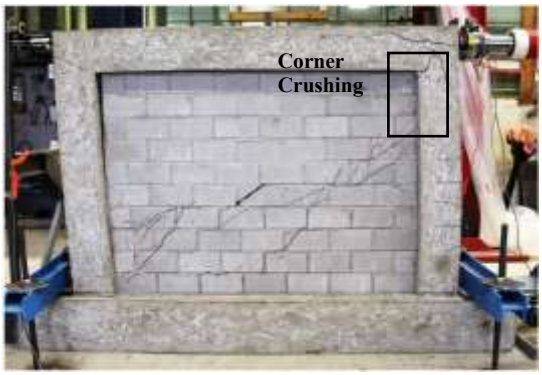

(b)

Figure 5.3. Comparison of Failure Mode between (a) IF-RS and (b) IF-NG

5.2.2 Comparison with Experimental Results of Manesh (2013)

The comparison was made with a specimen from Manesh (2013) on the effect of vertical load. Specimens IF-RS-A from the current study and CF-2 from Manesh (2013) both were subjected to 80 *kN* vertical load with the same load application set-up. Table 5.2 summarized the test results and Figure 5.4 plots two sets of load vs. displacement curves of the current and Manesh's studies so a relative comparison can be carried out. It shows that in the case of steel frame bounded infills, the presence of vertical load of 80 *kN* resulted in an increase in the lateral capacity of 24% while in the case of masonry frame bounded infills, the capacity increase was 41%. Also noted is that the presence of vertical load had a much more pronounced effect in increasing the frame stiffness for the masonry frame bounded infills. A side-by-side failure mode comparison in Figure 5.5 shows that specimen CF-2 (Manesh 2013) failed by corner crushing at the right bottom corner, whereas IF-RS-A experienced a sudden diagonal crack at ultimate with no evident corner crushing.

Table 5.2. Experiment Results of Current and Manesh (2013)'s Study

	Specimen ID	f'_m (MPa)	K_{ini} (kN/mm)	K_{cra} (kN/mm)	K_{ult} (kN/mm)	P_{cra} (kN)	P_{ult} (kN)	Final Failure Mode
Current Study	IF-RS (control)	18.9	26.6	17.9	8.1	93.4	142.5	DC
	IF-RS-A	18.9	175.0	51.8	48.7	124.5	199.6	DC
Manesh (2013)	CF-2	12.2	22.9	13.5	7.5	150.0	164.9	CC
	CF (control)	12.2	39.9	18.2	16.4	101.9	131.7	CC

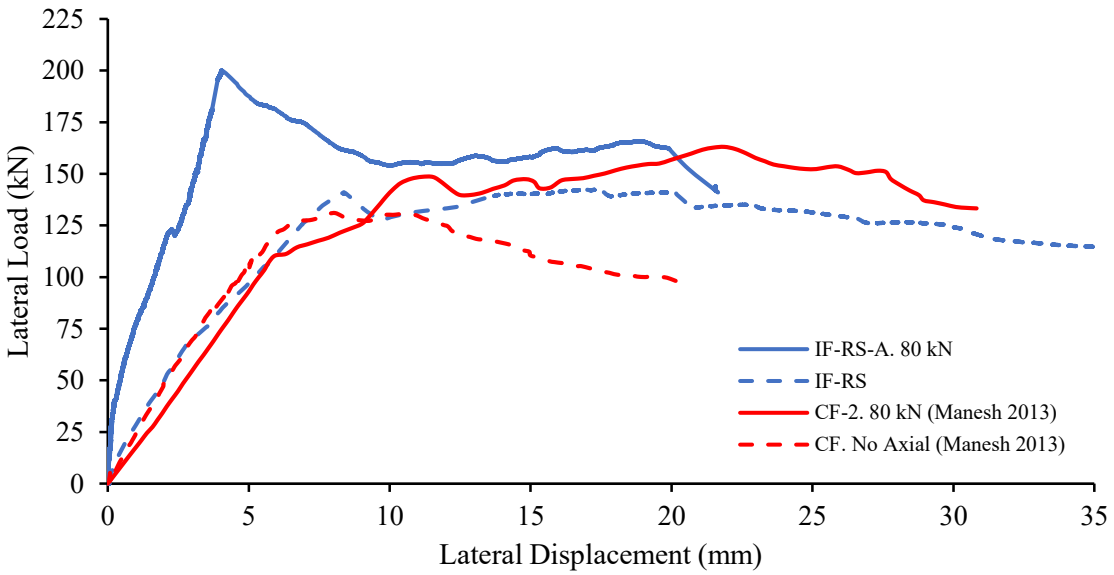

Figure 5.4. Load-Displacement Curves for Axial Load Effect Comparison Study

(a)

(b)

Figure 5.5. Comparison of Failure Mode between (a) IF-RS-A and (b) CF-2

5.3 COMPARISON WITH CSA S304.14 AND TMS 402/602-16

As mentioned previously, the all-masonry infilled frame is a new form of infilled frames and the above discussion indicates that its behaviour is comparable to the infilled RC frames. It is then a helpful exercise to evaluate the applicability of the current design provisions contained in the North American masonry design standards to this form of infilled frames. Table 5.4 summarizes all the materials and geometrical properties used for specimens in the calculation using the code equations. The compressive strength of the masonry infills (f'_m) was obtained from the results of masonry prism test. The modulus of elasticity of the infill (E_m) was taken as 850 f'_m according to CSA 304-14. The effective thickness, t_e, is defined as the face shell thickness of the masonry infill, while t is defined as the overall thickness of the infill. The modulus of elasticity of boundary frame members, including columns and beam, is calculated based on principles of mechanics as follows:

$$E_f = \frac{A_g E_g + A_b E_b}{A_T} \qquad [5\text{-}1]$$

where A_g and A_b are the cross-sectional areas of the grout column and boundary block, respectively; E_g and E_b are the elastic moduli of the grout column and boundary blocks, respectively; and A_T is the total cross-sectional area of the member. I_b and I_c are the moment of inertia of boundary frame members taking the reinforcement contribution into account.

Table 5.3. Material and Geometrical Properties of Specimens from This Study

Specimen ID	t (mm)	t_e (mm)	h (mm)	l (mm)	f'_m (MPa)	E_m (MPa)	$E_b=E_c=E_f$ (MPa)	$I_b=I_c$ ($x10^6$mm)
IF-RS	90	34	980	1350	20.9	17765	16909	124.8
IF-RW	90	34	980	1350	7.1	6035	16458	124.8
IF-RS-A	90	34	980	1350	23.4	19890	16905	124.8
IF-BB	90	34	980	1350	26.3	22355	17114	124.8
IF-BJ	90	34	980	1350	20.7	17595	16783	124.8

5.3.1 CSA S304.14 Stiffness Evaluation

For easy reference, the equations for calculation of the effective strut width specified in CSA S304-14 are summarizes as follows:

$$w_{eff} = \frac{1}{2}\sqrt{\alpha_h{}^2 + \alpha_L{}^2} \qquad [5\text{-}1]$$

Where:

$$\alpha_h = \frac{\pi}{2}\sqrt[4]{\frac{4E_f I_c h}{E_m t_e \sin 2\theta}}\ ;\ \alpha_L = \pi\sqrt[4]{\frac{4E_f I_b l}{E_m t_e \sin 2\theta}} \qquad [5\text{-}2]$$

For stiffness consideration, the CSA considers a reduction factor of 0.5 for W_{eff}, and then compared with quarter of the diagonal length, whichever is less would be considered as the effective width.

It should be noted that the above equation is intended for infills subjected to lateral loading only and therefore specimen IF-RS-A was not included in the comparison. Previous studies

by some researchers have used the experimental initial stiffness for the similar comparison and results were highly scattered. One challenge of using the initial stiffness is the non-unified definition of "initial" stiffness. While some researchers considered the initial stiffness as the slope of the tangential line to the very initial portion of the response curve, others have used the slope of initial linear portion of the curve. As the inherent "slack" exists between the infill and the frame, the engagement of the two does not necessarily occurs at the onset of loading and when the engagement occurs also depends on the system in question and workmanship. It is then not uncommon to have highly scattered results in initial stiffness. Secondly, the S304 equation is developed based on the diagonal strut concept which implies that the frame has deformed and separation between the infill and the frame at unloaded corners has occurred. It is therefore reasonable to assume that the infill may have sustained some level of cracking. It is believed that the crack stiffness is more appropriate in the comparison with the code values. This is also supported by Tucker (2007) and Manesh (2013). Table 5.4 summarizes the comparison of the experimental crack stiffness and the stiffnesses values based on CSA S304 equation. A sample calculation for the control specimen (IF-RS) is provided in Appendix A.

Table 5.4. Summary of Comparison of CSA S304.14 and Experimental Crack Stiffness

ID	Test Result	CSA S304-14	
	K_{cra}	K_{CSA}	K_{CSA}/K_{cra}
IF-RS	17.9	73.5	4.1
IF-RW	39.8	44.1	1.1
IF-BB	68.0	84.0	1.2
IF-BJ	45.7	73.0	1.6
		Avg.	2.0
		CV(%)	70.2

As shown in the table, the average of code-to-experimental stiffness ratio is 2.0 with a CV of 70.2%. Clearly, this high coefficient of variation is the result of specimen IF-RS. If this specimen was excluded from the comparison, the average ratio would be 1.3 with a CV of 20%. However, the general trend can still be observed where the S304 values overestimate the stiffness by 30% if IF-RS is excluded. This observation is also in line with findings from previous studies when the RC framed or steel framed infills were used in the evaluation of S304. For instance, Hu (2013) showed a mean code-to-experiment stiffness ratio of 1.5 when comparing experimental stiffness of five infilled RC frame specimens with the S304 predicted values. Soon (2011) and Xi (2016) reported a higher code-to-experiment stiffness ratio, in the order of 2 to 2.5, for infilled steel frames. This suggests that in terms of the code practice, the current design equation can be similarly applied to the all-masonry infilled frames as for the infilled RC frames. It also indicates that one set

of equations for all frame types especially considering concrete and steel in the same manner is questionable.

5.3.2 TMS 402/602 Stiffness Evaluation

The equations for strut width for stiffness calculation specified in TMS402/602 are summarized as follows.

$$W_{inf} = \frac{0.3}{\lambda_{strut} \cos\theta_{strut}} \qquad [5\text{-}3]$$

where λ_{strut} is the stiffness parameter, defined as below (Smith and Carter 1969):

$$\lambda_{strut} = \sqrt[4]{\frac{E_m t_{inf} \sin 2\theta}{4 E_{bc} I_{bc} h_{inf}}} \qquad [5\text{-}4]$$

Table 5.5 summarizes the comparison results. The average of code-to-experimental stiffness ratio is 1.1 with a CV of 67.9%. Again, if specimen IF-RS was excluded, the average ratio would be 0.77 with a CV of 15%. In comparison with S304, the results herein suggest that TMS values underestimate the stiffness by about 23% if IF-RS was excluded. Hu's study (2015) on RC framed infills, however, showed a mean code-to-experiment ratio of 1.17 when evaluating TMS 402/602 predicted values. Soon (2011) reported stiffness overestimation in the order of 55% by TMS 402/602 for infilled steel frames. Although the trend by the aforementioned results is not conclusive, it suggests the lack of consistency in the TMS402/602 stiffness equation, more so than CSA S304.

Table 5.5. Summary of Comparison of TMS 402/602 and Experimental Crack Stiffness

ID	Test Result	TMS	
	K_{cra}	K_{TMS}	K_{TMS}/K_{cra}
IF-RS	17.9	40.5	2.3
IF-RW	39.8	27.7	0.7
IF-BB	68.0	45.0	0.7
IF-BJ	45.7	40.2	0.9
		Avg.	1.1
		CV(%)	67.9

5.3.3 CSA S304.14 Strength Evaluation

CSA S304.14 states three failure modes for infilled frames. The following equations are provided for strength calculation of each mode according to the code.

(a) Diagonal Cracking Failure Modeϕ

$$V_r = \emptyset_m(v_m b_w d_v + 0.25P_d)\gamma_g \leq 0.4\emptyset_m\sqrt{f'_m}b_w d_v \gamma_g \quad [5\text{-}5]$$

Where,

$$V_m = 0.16(2 - \frac{M_f}{v_f d_v})\sqrt{f'_m} \quad [5\text{-}6]$$

In Equation (5-4), the maximum value for squat walls (h/l<1) is increased as below;

$$V_r \leq 0.4\emptyset_m\sqrt{f'_m}b_w d_v \gamma_g(2 - \frac{h}{l}) \quad [5\text{-}7]$$

where V_r is the ultimate load; ϕ_m and V_m are the resistance factor and shear strength of masonry. b_w is the actual thickness of the web of the infill wall; d_v is the effective depth of

the infill wall; P_d is the axial compressive load on the section under consideration; γ_g is the factor to account for partially grouted or un-grouted walls constructed of hollow or semi-solid units; M_f is the factored moment at the section considered; ν_f is the factored shear at the section considered.

(b) Sliding Shear Failure Mode

Sliding capacity along bed joint is:

$$V_r = 0.16\emptyset_m\sqrt{f'_m}A_{uc} + \emptyset_m\mu P_1 \quad [5\text{-}8]$$

where A_{uc} is the un-cracked portion of the effective cross-sectional area providing shear bond capacity; μ is the coefficient of friction on the interface between the frame and infill (here taken 1 as is for masonry-to-masonry interaction); P_1 is the minimum compressive force acting normal to the sliding plane taken as P_d plus 90% of the factored vertical component of compressive force of the diagonal strut.

(c) Corner Crushing Failure Mode

$$V_r = \frac{l}{\sqrt{h^2/l^2}}P_r \quad [5\text{-}9]$$

Where,

$$P_r = \emptyset_m\chi(0.85f'_m)w(2t_f - r) \quad [5\text{-}10]$$

$$r = (\frac{t}{2} + e) - \frac{1}{2}\sqrt{r^2 + 4te + 4e^2 - 16et_f} \quad [5\text{-}11]$$

where P_r is the factored axial load resistance; χ is the factor to account for direction of compressive stress in a masonry member relative to the direction used for the determination

of f'_m; t_f is the thickness of the flange of the concrete masonry unit; r is the radius of gyration; and e is the eccentricity of the load.

Table 5.6 lists experimental and code predicted ultimate loads of infill specimens. Note that the code equations are intended for infill strength, not the infilled frame strength. Thus, the experimental results of the infill strength were calculated as the infilled specimen ultimate load subtracted by the bare frame load at the corresponding failure point. Predicted strengths corresponding to all three failure modes as specified in CSA S304 were calculated and listed. A sample calculation for specimen IF-RS is included in Appendix A. The table shows that the sliding shear equation provides the best overall strength estimation with a code-to-experiment strength ratio of 0.9 and a CV of 18%. The corner crushing equation performed the second best with an average ratio of 1.1 and a CV of 29%. The diagonal cracking equation provides the least accurate prediction with an average ratio of 0.4 and a CV of 18%. Interestingly though, the experimental failure mode for three specimens was identified by diagonal cracking, but their ultimate loads were closer to the sliding shear predicted strength than those predicted by diagonal cracking. The latter would grossly underestimate the capacity of the specimens. This leads one to argue whether the diagonal cracking should be treated as an ultimate limit state as in most cases, the specimens continues to resist additional load even after extensive cracking. To further evaluate the code equations, the experimental cracking load where the first major cracking occurred was also listed in the table as $P_{cr\text{-}infill}$. The mean code-to-experiment ratio calculated at cracking, $P_{CSA\text{-}DC}$ /$P_{cr\text{-}infill}$ of 0.6, still suggests a significant underestimation by the code with a value of 0.6. The underestimation of the cracking load was also reported by Hu (2015) for infilled RC frames. For ultimate strength evaluation though, Hu's study showed

that S304 strength equation provides overestimates in corner crushing with a code-to-experiment ratio of 1.2. This is in line with the findings of this study on corner crushing where a code-to-experiment ratio of 1.1 was obtained as seen in the table.

Table 5.6. Comparison of Experimental Results and CSA S304.14 Predicted Ultimate Strengths

Spec. ID	Experimental Results				CSA S304.14						
	P_{ult} (kN)	P_{frame} (kN)	P_{infill} (kN)	$P_{cr\text{-}infill}$ (kN)	$P_{CSA\text{-}DC}$ (kN)	$P_{CSA\text{-}DC}/P_{cr\text{-}infill}$	$P_{CSA\text{-}DC}/P_{infill}$	$P_{CSA\text{-}SS}$ (kN)	$P_{CSA\text{-}SS}/P_{infill}$	$P_{CSA\text{-}CC}$ (kN)	$P_{CSA\text{-}CC}/P_{infill}$
IF-RS	142.5	47.0	95.5	70.9	47.3	0.7	0.5	98.0	1.0	130.6	1.4
IF-RW	115.2	28.0	87.2	62.2	27.6	0.4	0.3	57.1	0.7	57.7	0.7
IF-BB	148.5	32.5	116.0	66.3	53.0	0.8	0.5	110.0	0.9	155.7	1.3
IF-BJ	152.0	45.0	107.0	93.5	47.1	0.5	0.4	97.6	0.9	129.4	1.2
					Avg.	0.6	0.4		0.9		1.1
					CV%	26.8	18.2		18.2		28.8

5.3.4 TMS 402/602 Strength Evaluation

TMS 406/602 also considers three failure modes for infill strength, V_r, but with different definition and equations. As listed in the following, the three failure modes are corner crushing (a), shear sliding (c), and the infill strength corresponding to 25 *mm* horizontal displacement of the frame (b).

$$V_r = min \begin{cases} (a)\ (6.0\text{in.})t_e f'_m \\ (b)\ \text{Horizontal component of the force in the equivalent strut at 25 mm (1.0in.) displacement} \\ (c)\ V_n/1.5 \end{cases} \quad [5\text{-}13]$$

Where,

$$V_n = \min \begin{cases} 3.8A_{nv}\sqrt{f'_m} \\ 300A_{nv} \\ \text{or} \\ 56A_{nv} + 0.45N_u \text{ if not fully grouted} \\ 90A_{nv} + 0.45N_u \text{ if fully grouted} \end{cases} \quad [5\text{-}14]$$

Where,

$$A_{nv} = 0.8lt_e \quad [5\text{-}15]$$

V_n is the nominal shear strength, and N_u is the compressive force acting normal to shear surface.

Table 5.7 summarizes the code-to-experiment strength ratio for the specimens. The similar treatment as described previously was adopted herein to calculate the infill strength. A sample calculation is provided in Appendix A. According to TMS, the governing failure mode is sliding shear which yields the lowest strength of the three modes. However, the table shows that the code-to-experiment strength ratio for sliding shear is only 0.1 with a

CV of 12.6%, which indicates a gross underestimation of the specimen capacity. Recall that in the case of S304, sliding shear equation in the Canadian code actually provides much better prediction of strength. This seems to suggest that the equation in TMS for sliding shear needs to be reevaluated. On the other hand, the corner crushing equation of TMS showed a better performance with an average strength ratio of 0.9 and a CV of 38%. One anomaly was IF-RW with a strength ratio of 0.4. As the rest of terms are the same in the equation, the low ratio for this specimen was attributed to a much lower f'_m. Although it is simple to use, the constant term of 6 used in the equation will not accurately capture the variation of strut width as affected by material and geometric properties of the unfilled system. To find the infill strength corresponding to a 25 *mm* displacement, a simple frame with diagonal strut with corresponded properties was analyzed in SAP2000 and the load applied to the top beam was increased to reach 25 *mm* displacement. The horizontal component of the axial load in the diagonal strut was taken as the infill strength, and as shown in the table, this failure mode overestimated the design strength by approximately 5 times the experimental results. Further, the experimental infill load at 25 *mm* frame displacement ($P_{infill-25}$) was calculated, and as shown in the table, the TMS value showed a greater discrepancy in the order of 8 times the test results. It is noted that all specimens achieved their ultimate loads well before displacing 25 mm, hence it is not surprising to have the greater discrepancy when comparing experimental load at 25 mm lateral displacement with the design strength. This suggests it is questionable to use this specific lateral drift level as an ultimate limit state. Similarly, Hu (2015) concluded that TMS corner crushing equation provides the closest estimate to the test result for infilled RC

frames while the sliding shear and 25 mm lateral displacement equations either grossly underestimate or grossly overestimate the strength.

Table 5.7. Comparison of Experiment Results and TMS 402/602 Predicted Ultimate Strengths

Spec. ID	Experimental Results					TMS 402/602						
	P_{ult} (kN)	P_{frame} (kN)	P_{infill} (kN)	$P_{infill-25}$ (kN)	Failure Mode	P_{TMS-CC} (kN)	P_{TMS-CC} /P_{infill}	P_{TMS-SS} (kN)	P_{TMS-SS} /P_{infill}	P_{TMS-25} (kN)	P_{TMS-25} /P_{infill}	P_{TMS-25} /$P_{infill-25}$
IF-RS	142.5	47.0	95.5	75.8	DC	108.3	1.1	14.9	0.2	607.3	6.4	8.0
IF-RW	115.2	28.0	87.2	33.1	DC/SS	36.8	0.4	14.9	0.2	284.0	3.3	8.6
IF-BB	148.5	32.5	116.0	81.5	SS	136.3	1.2	14.9	0.1	721.0	6.2	8.8
IF-BJ	152.0	45.0	107.0	64.5	DC	107.3	1.0	14.9	0.1	606.9	5.7	9.4
						Avg.	0.9		0.1		5.4	8.7
						CV%	37.4		12.6		26.8	6.7

5.3.5 Summary

The above evaluation of both CSA S304 and TMS402/602 can be summarized as follows:

The applicability of the current code equations for both stiffness and strength is comparable between all-masonry infilled frames and infilled RC frames. In the case of stiffness calculation, CSA S304 overestimates whereas TMS 402/602 underestimates the stiffness, and the degree of the disparity seems to be in a similar range between the two codes. In terms of the strength calculation, CSA S304 performs better with both sliding shear and corner crushing failure modes providing reasonable estimates whereas only corner crushing equation in TMS 402/602 yielded reasonable estimate. Two additional observations were also made in the definition of failure modes. The diagonal cracking mode in S304 and 25 mm lateral displacement mode in TMS were not supported by experimental evidence and their validity to be defined as the ultimate limit states needs to be further investigated.

CHAPTER 6 SUMMARY AND CONCLUSIONS

6.1 SUMMARY

This experimental study was conducted to investigate the in-plane behaviour of all-masonry infilled frames, i.e., concrete masonry infills bounded by reinforced masonry frames. All infilled frame specimens were constructed with the same dimensions, measuring 980 mm high by 1350 mm long, and custom-made half-scale 200 mm concrete blocks were used for infills. The reinforced masonry frames consisted of 190x190 mm sections for the top beam and columns and a 280x250 mm section for the RC base beam. Six specimens included one bare frame, one control specimen, and four specimens with varying parameters were subjected to monotonic lateral loading until failure. The parameters included infill strength, infill horizontal reinforcement, and presence of vertical load. One specimen was constructed with weaker CMUs and mortar relative to the control specimen to study the effect of infill strength; two specimens were designed with infill horizontal reinforcement including 1) bed joint reinforcement implemented every other course in the infill and 2) two bond beams implemented in the infill at third and eighth course; and one specimen was tested under combined vertical and lateral loading to study the effect of vertical load. For all specimens, load vs. lateral displacement response, cracking pattern, failure mode, and crack and ultimate loads were obtained and discussed. These performance indicators of all-masonry infilled frames were also compared with those obtained in previous studies on RC framed and steel framed infills as appropriate. The validity of analytical methods provided by CSA S304.14 and TMS 402/602-16 on all-masonry infilled frames were also investigated by comparing with the experimental results with code suggested values.

6.2 CONCLUSIONS

The following conclusions were drawn from this study:

General Behaviour of All-Masonry Infilled Frames

The general behaviour of all-masonry infilled frames is similar to infilled RC frames. The similarities include the increase in stiffness and strength of the frame system as a result of the presence of infills. In particular, the ductile behaviour exhibited by all-masonry infilled frames is comparable to RC frames. The difference between these two types of systems seems to be in the experimentally observed failure mode. While both types of infilled frames sustained pronounced diagonal cracking within the infill prior to failure, the final failure of infilled RC frames was predominantly by corner crushing whereas the all-masonry infilled frames did not show evident crushing; instead, the final failure occurred when the diagonal cracking extended to the boundary columns.

Effect of Infill Strength

A stronger infill in terms of masonry compressive strength resulted in an increase in the ultimate strength of the infilled frame system. However, this increase is not in proportion to the increase in the compressive strength. In terms of stiffness, there was not a direct relationship between the infill strength and the infilled frame stiffness. In other words, a stronger infill does not necessarily lead to a stiffer infilled frame. In terms of failure mode, masonry strength did not seem to affect the failure mode. All failure modes were governed by severe diagonal cracking through infill and the boundary columns.

Effect of Infill Reinforcement

Infill reinforcement, whether in the form of joint reinforcement or bond beam, did not have a significant effect on the ultimate strength, when comparing to the control specimen (averagely 6% increase). With respect to stiffness, both specimens with infill reinforcement showed a remarkably higher initial and cracking stiffnesses than the control specimen and this increase was more pronounced for the specimen with bond beam than the specimen with bed joint reinforcement. In terms of failure mode, infill reinforcement was shown to change the diagonal cracking to shear sliding at courses where the reinforcement was present. It seems to suggest that the reinforcement "arrested" the cracking in the diagonal direction and changed it into sliding. As a result, the reinforced infilled frame showed greater displacement before reaching the ultimate and more ductile behaviour post-ultimate. The comparison between the joint reinforcement and bond beam showed that a distributed reinforcement scheme (bed joint reinforcement) performed better than a concentrated reinforcement scheme (bond beam).

Effect of Presence of Vertical Load

Presence of vertical load resulted in a marked increase in both ultimate and cracking loads as well as the stiffness including initial and cracking stiffness of the infilled specimen. However, less displacement sustained at the ultimate indicated lower ductility as a result of vertical load. Furthermore, the post-ultimate behaviour of the specimen with the vertical load was notedly more brittle than the control specimen. In terms of failure mode, the specimen with vertical load exhibited vertical cracks in the infill underneath the vertical loading points although the final failure was governed by a sudden diagonal cracking.

Ductility and Storey Drift

When considering the lateral drift levels defined by NBCC 2015, all specimens reached their ultimate load within the 1% drift level, the most stringent drift limit, indicating that the all-masonry infilled frame satisfies all three categories of building drift limits and thus can be used for all from the drift standpoint. In terms of ductility, all specimens showed a ductility ratio several times greater than unity, ductility assigned to unreinforced masonry systems in NBCC 2015. This indicates that unreinforced masonry infills bounded by reinforced masonry frames have much-improved ductility and have the potential to be used as a seismic resisting system. More tests need to be carried out in the cyclic test scheme to further evaluate the efficacy of the seismic resisting properties of the system.

CSA S304.14 and TMS 402/602 Evaluation

In general, the applicability of the code equations to the all-masonry infilled frames is similar to the infilled RC frames. For the stiffness prediction, it was concluded that CSA S304-14 seems to overestimate and TMS 402/602-16 seems to underestimate the stiffness with a similar degree of under- or over- estimation. For the strength prediction, the CSA S304.14 provided reasonable values for both sliding shear and corner crushing equations. Given that the diagonal cracking equation greatly underestimated the values, its validity to be considered as an ultimate limit state should be evaluated. The TMS 402/602 corner crushing equation seems to provide the most realistic strength values whereas the sliding shear and 25 *mm* displacement provisions either grossly under- or over- estimate the strength.

6.3 RECOMMENDATIONS FOR FUTURE RESEARCH

Since the all-masonry infilled frame is a new form of the infilled frame, more tests need to be conducted to include material, geometric, loading, and construction parameters that are unique to this system to have a thorough evaluation of the performance of the system. The following recommendations are provided for future work.

Material and geometric parameters

More tests should be carried out to investigate more variations of the masonry material property including properties of the infill and frame, and the relative of the two. Infill aspect ratios including more squat or slender infills should be a parameter for future testing.

Loading parameters

In the case of presence of vertical loading, more vertical load levels should be investigated to establish a correlation between the level of the load and the frame strength and failure mode. Further, the manner of vertical load application, i.e., whether it is applied through the boundary beam or through the boundary columns, should be included in the investigation.

Once the static loading characteristics of the new system are established, the study should include the quasi-static and cyclic loading conditions to establish the dynamic characteristics of the system.

Construction parameters

Under construction parameter consideration, the infill-to-frame interfacial gap, infill openings, infill-to-frame mechanical anchorage can be incorporated in testing. Moreover, the simultaneous construction of the infill and frame lend to possibility of grouting and reinforcing (vertical) the infill. This aspect of infill construction can be included in the further study.

REFERENCES

Abo El Ezz, A., Seif Eldin, H. M. and Galal, K. (2015). Influence of confinement reinforcement on the compression stress-strain of grouted reinforced concrete block masonry boundary elements, *Structures*. Elsevier B.V., 2, pp. 32–43.

Al-Chaar, G. (2002). Evaluating strength and stiffness of unreinforced masonry infill structures. *Journal of Structural Engineering*, ASCE, 128(8):1055-1063.

Al-Chaar, G., Issa, M., and Sweeney, S. (2002). Behavior of masonry-infilled nonductile reinforced concrete frames. *Journal of Structural Engineering*, 128(8):1055-1063.

M. Memari, A. and Aliaari, M. (2018). Finite Element Modeling of Masonry Infill Walls Equipped with Structural Fuse, in *New Trends in Structural Engineering*.

Amato, G. *et al.* (2008). Infilled frames: influence of vertical loads on the equivalent diagonal strut model', *Proc. of 14th WCEE.*

ASTM International. *A951/A951M-16e1 Standard Specification for Steel Wire for Masonry Joint Reinforcement*. West Conshohocken, PA, 2016.

ASTM International. *C143/C143M-15a Standard Test Method for Slump of Hydraulic-Cement Concrete*. West Conshohocken, PA, 2015.

ASTM International. *C39/C39M-16a Standard Test Method for Compressive Strength of Cylindrical Concrete Specimens*. West Conshohocken, PA, 2016.

ASTM International. *C140/C140M-18a Standard Test Methods for Sampling and Testing Concrete Masonry Units and Related Units*. West Conshohocken, PA, 2018.

ASTM International. *C270-14 Standard Specification for Mortar for Unit Masonry*. West Conshohocken, PA, 2014.

ASTM International. *C476-18 Standard Specification for Grout for Masonry*. West Conshohocken, PA, 2018.

ASTM International. *C1019-18e1 Standard Test Method for Sampling and Testing Grout*. West Conshohocken, PA, 2018.

ASTM International. *C1314-16 Standard Test Method for Compressive Strength of Masonry Prisms*. West Conshohocken, PA, 2016.

ASTM International. *C39/C39M-18 Standard Test Method for Compressive Strength of Cylindrical Concrete Specimens*. West Conshohocken, PA, 2018.

ASTM International. *E8/E8M-16a Standard Test Methods for Tension Testing of Metallic Materials*. West Conshohocken, PA, 2016.

Banting, B. R. and El-Dakhakhni, W. W. (2012). Force- and displacement-based seismic performance parameters for reinforced masonry structural walls with boundary elements, *Journal of Structural Engineering (United States)*, 138(12), pp. 1477–1491.

Banting, B., (2013). Seismic performance quantification of concrete block masonry structural

walls with confined boundary elements and development of the normal strain-adjusted shear strength expression (NSSSE) (Doctoral dissertation).

Banting, B.R. and El-Dakhakhni, W.W., (2013). Seismic performance quantification of reinforced masonry structural walls with boundary elements. *Journal of Structural Engineering*, *140*(5), p.04014001.

Banting, B.R. and El-Dakhakhni, W.W., (2014). Seismic design parameters for special masonry structural walls detailed with confined boundary elements. *Journal of Structural Engineering*, *140*(10), p.04014067.

CAN/CSA A165 (2014). CSA standards on concrete masonry units. Mississauga, ON, Canada: Canadian Standard Association.

CAN/CSA S304-14 (2014). Design of masonry structures. Mississauga, ON, Canada: Canadian Standard Association.

Chen, X. (2016). Numerical study of the in-plane behaviour of concrete masonry infills bounded by steel frames. Ph.D. Thesis, Civil & Resource Engineering Department Dalhousie University, Halifax, Canada.

Chen, X. and Liu, Y. (2015). Numerical study of in-plane behaviour and strength of concrete masonry infills with openings, *Engineering Structures*. Elsevier Ltd, 82, pp. 226–235.Cyrier, W.B., (2012). Performance of concrete masonry shear walls with integral confined concrete boundary elements. Ph.D. Dissertation, Washington State University.

Dawe, J.L., and Seah, C.K. (1989). Behaviour of masonry infilled steel frames. *Canadian Journal of Civil Engineering*, 16(6): 865–876.

Decanini L.D., Fantin G.E., (1986). Modelos simplificados de la mamposteria incluida en porticos. Caracteristicas de rigidez y resistencia lateral en estado limite, Jornadas Argentinas de Ingenieria Estructural, Buenos Aires, Argentina, 1986, Vol.2, pp.817-836 (in Spanish).

Di Trapani, F. *et al.* (2015). Masonry infills and RC frames interaction: Literature overview and state of the art of macromodeling approach, *European Journal of Environmental and Civil Engineering*. Taylor & Francis, 19(9), pp. 1059–1095.

Drysdale, R.G., and Hamid, A.A. (2005). Masonry structures: behavior and design. Mississauga, Ontario: Canadian Masonry Design Centre.

El-Dakhakhni, W. W. (2002). Experimental and analytical seismic evaluation of concrete masonry-infilled steel frames retrofitted using GFRP laminates. Ph.D. Dissertation, Drexel University.

El-Dakhakhni, W., Elgaaly, M. and Hamid, A. (2003). Three-strut model for concrete masonry-infilled steel frames. *Journal of Structural Engineering*, 129(2), 177-185.

Ezzeldin, M., El-Dakhakhni, W. and Weibe, L. (2017). Experimental assessment of the system-level seismic performance of an asymmetrical reinforced concrete block – wall building with boundary elements, *Journal of Structural Engineering*, 143(8), pp. 1–13.

Flanagan, R. D., & Bennett, R. M. (1999). In-plane behavior of structural clay tile infilled frames. *Journal of Structural Engineering*, ASCE. *125*(6), pp.590-599

Hendry A.W. (1998). Structural Masonry, 2nd ed. Macmillan Press, London.
Holmes M. (1961). Steel frames with brickwork and concrete infilling. *Proceedings of the Institution of Civil Engineers*, 19: 473-478.

Hu C. (2015). Experimental study of the effect of interfacial gaps on the in-plane behaviour of masonry infilled RC frames. MASc Thesis, Civil & Resource Engineering Department, Dalhousie University, Halifax, Canada.

Kingsley, G.R., Gangel, T. and Shing, P.B., (2014). Design of special reinforced masonry shear walls in the US.

Liauw, T.C. and Kwan, K.H. (1984). Plastic theory of infilled frames with finite interface shear strength. *Proceedings of the Institute of Civil Engineers*, 75(4):707-723.

Liu, Y. and Soon, S. (2012). Experimental study of concrete masonry infills bounded by steel frames. *Canadian Journal of Civil Engineering*, 39: 180–190.

Mainstone, R. J. (1971). On the stiffness and strengths of infilled frames. *Proceedings of the Institute of Civil Engineers*, Suppl. (4):57–90.

Manesh, P.B. (2013). Experimental study of masonry-infilled steel frames subjected to combined axial and in-plane lateral loading. MASc thesis, Civil & Resource Engineering Department, Dalhousie University, Halifax, Canada.

Mehrabi, A. B., Shing, P. B., Schuller, M. P., and Noland, J. L. (1996). Experimental evaluation of masonry-infilled RC frames. *Journal of Structural Engineering*, ASCE, 122(3):228-237.

Paulay, T., & Priestley, M. J. N. (1992). Seismic design of reinforced concrete and masonry buildings, Wiley New York.

Papia, M., Cavaleri, L., Fossetti, M., (2003). Infilled frames: developments in the evaluation of the stiffening effect of infills. *Structural Engineering and Mechanics* 16:6, 675-693.

Polyakov, S. V. (1956). Masonry in framed buildings (An investigation into the strength and stiffness of masonry infilling). Gosudarstvennoe izdatel'stvo Literatury po stroitel'stvu iarkhitekture, Moscow. (English translation by G. L. Cairns, National Lending Library for Science and Technology, Boston, Yorkshire, England, 1963).

Priestley MJN, Calvi M. (1991). Towards a capacity-design assessment procedure for reinforced concrete frames. Earthq spectra.

Robazza, b. R. (2019). Reinforced masonry shear walls subjected to in-plane seismic. Ph.D Thesis, The faculty of graduate and postdoctoral studies, The university of British Columbia, Vancouver, Canada.

Rosenblueth. E. (1980). Design of earthquake resistant structures. Pentech Press Limited: 195-222.

Saneinejad, A. and Hobbs, B., (1995). Inelastic design of infilled frames. *Journal of Structural Engineering*, *121*(4), pp.634-650.

Shedid, M. T., El-Dakhakhni, W. W. and Drysdale, R. G. (2010). Alternative strategies to enhance the seismic performance of reinforced concrete-block shear wall systems, *Journal of Structural Engineering*, 136(6), pp. 676–689.

Shing, P. B. and Mehrabi, A. B. (2002). Behaviour and analysis of masonry-infilled frames, *Progress in Structural Engineering and Materials*, 4(3), pp. 320–331.

Stafford-Smith, B., and Carter, C. (1969). A method of analysis for infilled frames. *Proceedings of the Institution of Civil Engineers*, 44(1):31-48.

Stafford-Smith, B., and Coull, A. (1991). Tall building structures: analysis and design, Wiley-Interscience.

Steeves, R. (2017). In-plane behaviour of masonry infilled rc frames with interfacial gaps subjected to quasi-static loading. MASc Thesis, Civil & Resource Engineering Department, Dalhousie University, Halifax, Canada.

Soon, S. (2011). In-plane behavior and capacity of concrete masonry infills bounded by steel frames. MASc Thesis, Civil & Resource Engineering Department, Dalhousie University, Halifax, Canada.

Tassios, T. P. (1993). Seismic design of reinforced concrete and masonry buildings, Structural Safety.

TMS 402/602 Building Code Requirements and Specifications for Masonry Structures, 2016. *Concrete International*.

Tucker, C. J. (2007). Predicting the in-plane capacity of masonry infilled frames. Ph.D. Thesis, Tennessee Technological University, USA.

World house encyclopedia, Steel moment resisting frame with brick masonry partitions, digital image. < http://db.world-housing.net/building/95 >.

APPENDIX A SAMPLE FOR DESIGN STRENGTH AND STIFFNESS CALCULATION

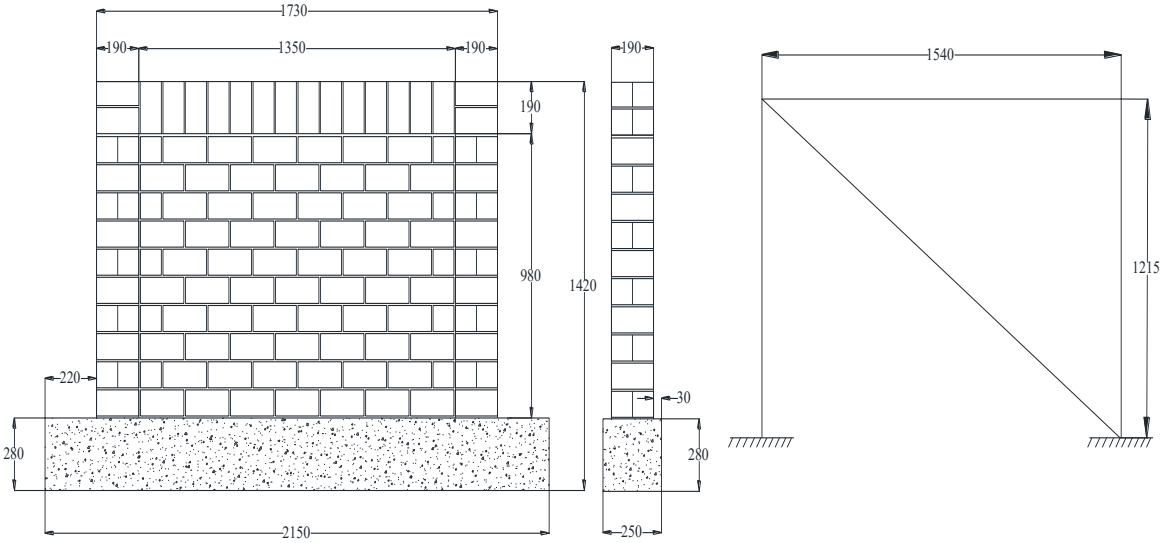

For calculation sample, the control specimen, **IF-RS**, is under study.

Frame Properties:

h' = 1170 *mm* l' = 1730 *mm* I_b and I_c = 124.8 x 10^6 *mm*

$E_b = E_c = E_f$ = 16909 *MPa*

Infill Properties:

f'_m = 20.9 *MPa* E_m = 17765 *MPa* t = 90 *mm* t_f = 34 *mm*

t_e = 17 *mm* h= 980 *mm* l= 1350 *mm*

CSA S304.14

Stiffness Calculation

the diagonal strut width is calculated as follow:

$$w_{eff} = \frac{1}{2}\sqrt{{\alpha_h}^2 + {\alpha_L}^2} = \sqrt{544^2 + 1178^2} = 649\ mm$$

Where:

$$\alpha_h = \frac{\pi}{2}\sqrt[4]{\frac{4E_f I_c h}{E_m t_e sin2\theta}} \qquad ; \alpha_L = \pi\sqrt[4]{\frac{4E_f I_b l}{E_m t_e sin2\theta}}$$

$$\alpha_h = \frac{\pi}{2}\sqrt[4]{\frac{4(16909)(124.8 \text{ x } 10^6)(980)}{(17765)(34)sin(2(0.628))}} = 544\ mm$$

$$\alpha_h = \pi\sqrt[4]{\frac{4(16909)(124.8 \text{ x } 10^6)(1350)}{(17765)(34)sin(2(0.628))}} = 1178\ mm$$

Where,

$$\theta = tan^{-1}\frac{h}{l} = tan^{-1}\frac{980}{1350} = 0.628\ rad$$

$$l_d = \sqrt{h^2 + l^2} = 1668\ mm \Longrightarrow \frac{l_d}{4} = 417\ mm$$

For stiffness consideration, CSA S304.14 states that the effective strut width should be reduced by half and not more than quarter of the infill diagonal length.

So, we have: 1/2 * 649 = 324.5 mm < 417 mm, therefor, 324.5 mm is used as the diagonal strut width for stiffness calculation.

A SAP2000 was adopted with IF-RS properties and the calculated effective strut width. 1 kN load was applied to the top beam and the corresponded displacement was observed (Δ = 0.0136 mm) . Thus, the specimen stiffness is: $K = \frac{1}{0.0136} = 73.5\ kN/mm$

Strength Calculation

1. Diagonal cracking strength

$V_r = \emptyset_m(v_m b_w d_v + 0.25P_d)\gamma_g = 1.0(1.3(90)(1080) + 0.25(0)) = 47.3\ kN$

Where,

ϕ_m = 1.0 (resistance factor set to unity to compare with the raw experimental data)

$V_m = 0.16(2 - \frac{M_f}{v_f d_v})\sqrt{f'_m} = 0.16(2 - 0.25)\sqrt{20.9} = 1.3\ kN$

$M_f/v_f d_v$ = 0.25 (taken as the minimum value of 0.25)

b_w = t = 90 *mm*

d_v = 0.8l = 0.8(1350) = 1080 *mm*

P_d = 0 (self-weight and dead load is neglected)

$\gamma_g = t_e/t = 0.38$

the calculated v_r is less than the upper value for squat walls (h-l<1):

$$V_r = 47.3\ kN \leq 0.4\emptyset_m\sqrt{f'_m}b_w d_v \gamma_g(2 - \frac{h}{l})$$

$$= 0.4(1.0)\sqrt{20.9}(90)(1080)(0.38)(2 - \frac{980}{1350}) = 86\ kN$$

2. Shear sliding strength

$$V_r = 0.16\emptyset_m\sqrt{f'_m}A_{uc} + \emptyset_m\mu P_1$$

$$= 0.16(1.0)\sqrt{20.9}(36720) + 1.0(1.0)(0.9)(sin(54))V_r = 98\ kN$$

Where,

$A_{uc} = 0.8lt_e = 0.8(1350)(34) = 36720\ mm^2$

$\mu = 1.0$ (for masonry to masonry sliding friction)

$P_1 = 0.9(\sin 54)V_r = 0.726V_r$ (the vertical component of the diagonal compression force)

3. Corner crushing strength

according to CSA S304.14 (7.13.3.4), the effective length for slenderness effect is as below:

$h = l_d - w = 1668 - 649 = 1019\ mm$

$k(l_d - w)/t = 0.9(1019)/90 = 10.2 < 30$ OK

$$P_r = \emptyset_m\chi(0.85f'_m)w(2t_f - r) = 1.0(0.5)(0.85(20.9))(649)(2 * 17 - 6)$$

$$= 161.4\ kN$$

Where,

$\chi = 0.5$ (CSA S304.1 cl 10.2.6)

$k = 0.9$ ((effective length factor, CSA S304.1 Annex B)

$b = w = 649\ mm$

r = 6 mm and is calculated as bellow:

$$r = (\frac{t}{2} + e) - \frac{1}{2}\sqrt{r^2 + 4te + 4e^2 - 16et_f}$$

Where, e = 0.1t = 0.1*90 = 9 (as the initial eccentricity)

$$P_{cr} = \frac{\pi^2 \emptyset_e (EI)_{eff}}{(kh)^2(1 + 0.5\beta_d)} = \frac{3.14^2(1.0)(2.1 \times 10^{12})}{(0.9 \times 1019)^2(1 + 0.5 * 0)} = 1620\ kN$$

Where,

ϕ_e = 1.0 (resistance factor)

β_d = 0 (temporary loading)

$(EI)_{eff} = 0.4E_mI_0 = 0.4*17765*3*10^7 = 2.1*10^{11}$ mm^4

I_o = moment of inertia of the uncracked cross-sectional area of the effective strut)

$$I_0 = \frac{(90^3 - (90 - 2 * 17)^3)649}{12} = 3 * 10^7\ mm^4$$

$$e' = \frac{1}{1 - \frac{P_r}{P_{cr}}} e$$

So,

$$e' = \frac{1}{1 - \frac{161.4}{1620}} (9) = 9.99\ mm$$

Once the first e' is calculated, it replaces the previous e to reiterate the results. The iteration process is to be carried out between e and e' until they converge. P_r is the compressive strength

of the diagonal strut, therefor, the infill strength is the horizontal component of P_r. So, the corner crushing capacity of infill is:

$$P_{cc} = \frac{l}{l_d} P_r = \frac{1350}{1668} * 161.4 = 130.6\ kN$$

TMS 402/602-16

Stiffness Calculation

First, the width of strut calculated as following:

$$w = \frac{0.3}{\lambda cos\theta} = \frac{0.3}{0.00289 \cos{(0.628)}} = 128.4\ mm$$

Where,

$$\lambda = \sqrt[4]{\frac{E_m t sin2\theta}{4E_f Ih}} = \sqrt[4]{\frac{17765 * 34 * sin\ (1.256)}{4 * 16909 * 980 * 124.8 * 10^6}} = 0.00289$$

A SAP2000 linear analysis of a braced frame with properties corresponding to TMS 402 strut width showed 0.0247 mm displacement under 1 *kN* force on the top beam. Consequently, the stiffness was 40.5 kN/mm.

Strength Calculation

Specimen IF-RS failure mode was diagonal cracking, but to have a general comparison all three failure modes proposed by TMS 402/602 are considered to calculate.

1. Corner crushing failure

$V_r = (6.0\ inches) t_e f'_m$ = (6*25.4)(34)(20.9) = 108.3 *kN*

2. Sliding shear failure

$$V_r = \frac{V_n}{1.5}$$

Where,

$$V_n = min \begin{cases} 3.8A_{nv}\sqrt{f'_m} \\ 300A_{nv} \\ or \\ 56A_{nv} + 0.45N_u \text{ if not fully grouted} \\ 90A_{nv} + 0.45N_u \text{ if fully grouted} \end{cases}$$

Where,

$N_u = 0.81V_n$ (Compressive force acting normal to shear surface)

$A_{nv} = 0.8lt_e = 0.8(1350)(34) = 37620\ mm^2 = 56.9\ in^2$

Therefor the minimum V_n is:

$V_n = 56(56.9) + (0.45)(0.81V_n)$

$V_n = 5010$ lb $= 22.3\ kN$

$V_r = V_n/1.5 = 14.9\ kN$

3. 25 mm lateral displacement

with iteration of load changing on a braced frame in SAP2000, the load of 1015 kN made 25 mm displacement. The axial load in the strut calculated by the software was 750.5 kN. Thus, the horizontal component of compression strut is the design strength which is as follow: $V_r = 750.5(\cos(0.628)) = 607.3\ kN$